University of Alberta

A unified FEM-based framework for medical image registration and segmentation

by

Karteek Popuri

A thesis submitted to the Faculty of Graduate Studies and Research
in partial fulfillment of the requirements for the degree of

Doctor of Philosophy

Department of Computing Science

Fall 2013
Edmonton, Alberta

Abstract

Image registration and segmentation are two most fundamental tasks in medical image analysis. In practice, these tasks are usually performed manually, but this is tedious, time consuming and prone to human errors. Therefore, efficient and reliable automatic medical image registration and segmentation methods need to be developed. This is difficult because medical images are generally corrupted by noise, image artifacts and the various anatomical regions of interest in medical images often do not have distinct sharp boundaries. However, these anatomical regions frequently exhibit consistent shape and topological characteristics which is an advantage when compared to natural images.

In our proposed work, we take into account the above mentioned aspects and devise automatic registration and segmentation methods using the popular energy minimization framework, with an application to medical images. In contrast to the widely used level set based segmentation approach, we follow the template-based segmentation approach, which is more suitable for medical images as it can easily handle multi-region segmentation and also has the desirable property of preserving the known topology of the anatomical structures. However, unlike the traditional template-based segmentation and registration methods that use uniform meshes along with the finite difference method (FDM) to solve the partial differential equations (PDEs) that arise in these methods, we use the finite element method (FEM) and solve the PDEs on a non-uniform mesh to obtain solutions whose accuracy is well adapted to the salient features in the image domain. In this work, we present a unified FEM-based registration and segmentation framework where the goal is to estimate a deformation field following the minimization of an energy that consists of a common diffusion-based regularization term and data term that depends on the appropriate segmentation or registration objective. Further, we extend this framework through the incorporation of an additional shape prior based regularization term that is learned from training data. Lastly, we propose a novel variational formulation for discrete deformable registration and show that interestingly it can be cast into the proposed unified FEM-based registration and segmentation framework.

We validated our proposed unified FEM-based segmentation and registration framework on real medical images including some of the popular benchmark datasets. We present a thorough evaluation of the various registration and segmentation algorithms developed in our work by comparing their performance with the other established methods in image registration and segmentation.

Acknowledgements

I want to acknowledge my supervisor Dr. Martin Jägersand for the constant support and patience throughout the course this work. I am extremely grateful to my co-supervisor Dr. Dana Cobzas for the guidance and encouragement with the project. I am also thankful to the members of the vision lab David Lovi, Neil Birkbeck for useful inputs on my research. I also want to thank Dr. Vickie Baracos and Nina Esfandiari with whom I collaborated on various projects.

Table of Contents

List of Tables

List of Figures

List of Symbols

Chapter 1

Introduction

Nowadays, non-invasive medical imaging techniques are a de facto standard in clinical settings for diagnosis and treatment planning of various types of cancers and other pathologies in the human body. Further, medical images are also extensively used in medical science research studies that strive to understand the physiological and pathological processes underlying the normal and diseased human anatomy. Before clinically or scientifically relevant inferences can be made from medical images, two fundamental image processing tasks of registration and segmentation need to be undertaken. Performing these tasks manually is in general too cumbersome, time consuming and often produces results that suffer from inter (intra)-expert variability. Hence, there is a great motivation to develop accurate and efficient automatic methods for reliable medical image registration and segmentation.

The tasks of automatic medical image registration and segmentation are quite challenging because of following main issues:

(1) **Weak boundaries (poor contrast)**: The inability of a particular medical image modality to acquire sufficient contrast results in weak image edges or boundaries between the various anatomical regions of interest. This makes the automatic segmentation task difficult because it heavily relies on the intensity information to disambiguate between the various anatomical regions of interest. Additional information can be incorporated through the use of an atlas image to aid in segmentation, but this requires the need for automatic image registration, which in itself is a non-trivial task.

(2) **Sensor noise**: In medical images, sensor noise and other image artifacts are ubiquitous, resulting in spurious image features. This can seriously mislead automatic segmentation methods that are based on image edge information in the image, as these methods can confuse the spurious image features with the true boundaries of the anatomical regions of interest. Also, automatic registration methods can obtain incorrect correspondences between the spurious image features and the actual anatomical regions of interest.

The popular trend in medical image segmentation is to use region-based energies (which effectively

address the issues of weak boundaries and sensor noise) within a level set based optimization framework [23], [79]. But, the most desired feature of level sets, which is their ability to freely allow to for topological changes is actually a disadvantage in the case of medical images where the topology of the anatomical regions of interest is already known and needs to be maintained throughout the segmentation process. Besides, it is not trivial to extend the level set framework for multi-region segmentation (which is often required in medical images), as the evolving level sets corresponding to different regions might overlap with each other. Although, there exist level set based multi-region segmentation methods [17], [123] that solve this overlap problem, they still cannot prevent the undesired topology changes. Therefore, an alternate template-based approach for multi-region segmentation can be considered, where a template containing the topology and layout of the regions of interest is smoothly deformed according to the minimization of a region-based energy. The template-based segmentation task is similar to the deformable registration task in the sense that, in both template-based segmentation and deformable registration an unknown smooth deformation field is estimated via the minimization of an energy functional. Further, the regularization strategies used in both these tasks for achieving a smooth deformation field are often identical. However, in template-based segmentation a region-based energy is minimized as opposed to the image similarity measure in deformable registration. A common drawback among the existing template-based segmentation methods [102], [55] and most of the popular deformable registration methods [25], [112], [72], [99] is that the partial differential equations (PDEs) that arise in these various deformable registration and template-based segmentation methods are solved using uniform meshes and using the finite difference method (FDM). This approach achieves solutions with an uniform accuracy across the problem domain. This is not desirable in medical image problems where usually more accurate solutions are required near the boundaries of the anatomical regions and an inferior quality solution can be tolerated elsewhere.

Despite the similarity between the template-based segmentation and deformable registration tasks, currently there does not exist a framework that considers these tasks in a unified manner. In this work, we provide such a unified framework for template-based segmentation and deformable registration. Here, we address the main shortcoming of the traditional template-based segmentation and registration methods, which is the use of uniform discretizations, by solving the PDEs in a more computationally efficient and accurate manner using the finite element method (FEM). This facilitates the use of non-uniform meshes with a variable mesh resolution that can be well adapted to the salient features in the image domain. Specifically, in this work we present a unified FEM-based registration and segmentation framework where the goal is to estimate a deformation field following the minimization of an energy that consists of a common diffusion-based regularization term and data term that depends on the appropriate segmentation or registration objective. We propose two approaches, namely, variational-like and demons-like approaches for the numerical solution of this energy minimization using the FEM method. Although, there are some segmentation methods

that have been proposed using the non-uniform FEM mesh [106], [39], these methods do not take the template-based approach but rather use the FEM parametrization of the popular snakes model [60]. Likewise, a few FEM-based registration methods have also been proposed [40], [89], [56], but these methods use complex bio-mechanical models to model the elastic behavior of the underlying anatomy in medical images and hence they are not applicable for general image registration tasks. The diffusion-based regularization that we propose can impose a gamut of smoothness constraints, from isotropic homogeneous to anisotropic inhomogeneous depending on the specific registration task.

An advantage in medical images compared to natural images is the availability of a priori knowledge about the shape characteristics of the various anatomical regions of interest. Therefore, in order exploit this advantage, we investigate an extension to our unified FEM-based registration and segmentation framework through the incorporation of an additional shape prior based regularization term. Lastly, we propose a novel variational formulation for discrete deformable registration which results in a convex energy and show that it can be cast into our unified FEM-based registration and segmentation framework.

1.1 Contributions of this thesis

To summarize, the list of our theoretical contributions are below:

- Propose a unified FEM-based registration and segmentation framework.
- A new convex variational formulation of the discrete deformable registration task using the FEM method.
- Formulate a shape prior on the FEM-based nodal deformation fields and incorporate them into the unified FEM-based registration and segmentation framework.
- Perform an extensive validation of the proposed FEM-based registration and segmentation methods on synthetic and real medical images.
- Provide an application of the proposed FEM-based registration method to the task of muscle and fat tissue segmentation in thoracic computed tomography (CT) images for body composition estimation.

1.2 Thesis outline

The rest of this thesis is organized as follows:

- Chapter 2 presents a detailed review of the existing methods on deformable image registration and image segmentation using deformable models.

- Chapter 3 discusses the basic concepts in the finite element method (FEM).
- Chapter 4 presents the proposed unified FEM-based framework for image registration and segmentation. In this chapter, the FEM-based continuous deformable registration and template-based segmentation methods are developed and evaluated on synthetic and real medical image data.
- Chapter 5 presents the novel FEM-based variational discrete registration method.
- Chapter 6 presents a comparative evaluation between the proposed FEM-based continuous and discrete registration methods and the other popular deformable registration methods on two 3D benchmark data sets.
- Chapter 7 discusses the application of the proposed unified FEM-based registration and segmentation framework for the segmentation of computed tomography (CT) images.
- Chapter 8 presents the conclusion and discusses the future work.

1.3 Publications related to this thesis

1.3.1 Peer-reviewed journals

- **Karteek Popuri**, Dana Cobzas and Martin Jägersand, "Random walker based discrete deformable registration", Medical Image Analysis (*in preparation*).

1.3.2 Peer-reviewed conferences

- **Karteek Popuri**, Dana Cobzas, and Martin Jägersand, "A variational formulation for discrete registration", Medical Image Computing and Computer Assisted Intervention (MICCAI), 2013 (*accepted*).
- **Karteek Popuri**, Dana Cobzas, Martin Jägersand, Nina Esfandiari, and Vickie Baracos, "FEM-based automatic segmentation of muscle and fat tissues from thoracic CT images", International Symposium on Biomedical Imaging (ISBI), 2013 (*to appear*).
- **Karteek Popuri**, Dana Cobzas, and Martin Jägersand, "A FEM deformable mesh for active region segmentation", International Symposium on Biomedical Imaging (ISBI), 2013 (*to appear*).
- **Karteek Popuri**, Dana Cobzas, and Martin Jägersand, "Fast FEM-based non-rigid registration", Computer and Robot Vision (CRV), 2010.

Chapter 2

Literature review

In this chapter, a comprehensive yet concise survey of the vast amount of existing literature on deformable registration methods and image segmentation methods using deformable models is presented. Broadly, the structure of our discussion adheres to the dichotomy of non-parametric or parametric approaches, that naturally emerges in both deformable registration and segmentation using deformable models. The deformable registration methods are categorized as non-parametric or parametric depending on the regularization strategy used. On the other hand, the segmentation methods using deformable models are classified as non-parametric or parametric based on the chosen representation of the deformable model. We also shortly discuss the coupled registration and segmentation methods that aim to solve the registration and segmentation tasks simultaneously.

2.1 Deformable image registration

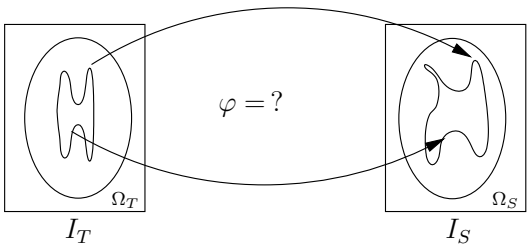

Figure 2.1: Illustration of deformable image registration

Given a *source* image $I_S : \Omega_S \to \mathbb{R}$, $\Omega_S \subset \mathbb{R}^\nu$ and a *template* image $I_T : \Omega_T \to \mathbb{R}$, $\Omega_T \subset \mathbb{R}^\nu$, $\nu = 2$ or 3, the goal of deformable or non-rigid registration is to find a dense transformation $\varphi : \Omega_T \to \Omega_S$ such that the *warped* source image $I_S \circ \varphi : \Omega_T \to \mathbb{R}$ is similar to the template image I_T. The non-rigid transformation φ can be conveniently split into the identity part and a non-linear transformation represented by the *deformation* or *displacement* field $\mathbf{U} : \Omega_T \to \mathbb{R}^\nu$, such that $\varphi(\mathbf{x}) = \mathbf{x} + \mathbf{U}(\mathbf{x})$ and $(I_S \circ \varphi)(\mathbf{x}) = I_S(\varphi(\mathbf{x})) = I_S(\mathbf{x} + \mathbf{U}(\mathbf{x}))$, $\forall \mathbf{x} \in \Omega_T$. Now, the task of deformable registration can be formulated as finding an optimal deformation field $\mathbf{U}^*$ through the minimization of the *data term* E_D, which measures the similarity between the warped source image

and the template image:

$$\mathbf{U}^* = \underset{\mathbf{U}}{\operatorname{argmin}}\ E_D[\mathbf{U}; I_T, I_S], \tag{2.1}$$

$$\text{where} \quad E_D[\mathbf{U}; I_T, I_S] = E_D^{\text{SSD}}[\mathbf{U}; I_T, I_S] = \frac{1}{2}\int_{\Omega_T} \left(I_S(\mathbf{x} + \mathbf{U}(\mathbf{x})) - I_T(\mathbf{x})\right)^2 d\mathbf{x}.$$

Remarks.

1. **Data term**: The particular data term E_D^{SSD} shown above is the most commonly used Sum of Squared Differences (SSD) similarity measure. Other popular choices for the data term include the Correlation Coefficient (CC), Correlation Ratio (CR), Joint Entropy (JE), Mutual Information (MI) and the Normalized Mutual Information (NMI) (see [113] for detailed expressions of these data terms). In the following discussion unless otherwise specified the SSD data term is being used.

2. **Ill-conditioned problem**: The above mentioned data term minimization is inherently ill-posed, as small changes in the input data might lead to large changes in the output. Also, the data term is typically non-convex and thus there exist multiple local minima. Hence, a direct minimization of the data term is not possible. Therefore, the *regularization* or *smoothing* constraints are required to make the minimization problem tractable.

Over the years, various regularization approaches have been proposed for the task of deformable registration. These approaches can be broadly categorized into two groups:

- **Non-parametric approaches**: An *explicit* regularization term (regularizer) is added to smooth the deformation field.

- **Parametric approaches**: The regularization is enforced in an *implicit* manner through the parametrization of the deformation field using a finite set of basis functions.

Another way to regularize the minimization problem in Eq. 2.1 is by restricting the deformation field to Sobolev spaces H^s, which by construction contain only functions with certain regularity properties, that are in turn desirable for deformable registration [24], [12], [140].

Diffeomorphisms: A good space of non-rigid transformations In general, it might be desirable to estimate a non-rigid transformation φ (or equivalently the deformation field $\mathbf{U}$) that is not only smooth but is also invertible, i.e. there exists a smooth $\varphi^{-1} : \Omega_S \rightarrow \Omega_T$ such that $\varphi^{-1}(\mathbf{x}) = \mathbf{x} + \mathbf{U}^{-1}(\mathbf{x})\ \forall\, \mathbf{x} \in \Omega_S$, where $\mathbf{U}^{-1} : \Omega_S \rightarrow \mathbb{R}^\nu$ is the corresponding inverse deformation field. Such smooth transformations which are invertible and have smooth inverses are known as *diffeomorphisms*. Particularly, in medical image registration the estimation of diffeomorphic transformations is a natural choice because the space of diffeomorphisms is ideally suited to capture the actual real world deformations that the underlying anatomical regions can undergo. In other words,

the estimation of a diffeomorphic transformation preserves the smoothness and also ensures that no "foldings " (or "tears") occur while mapping the anatomical regions in the template image to the source image and vice-versa. As a consequence, connected (disjoint) anatomical regions in the template image also remain connected (disjoint) in the source image. Although, the above mentioned regularization approaches (parametric, non-parametric and the restriction to Sobolev spaces) can ensure smoothness of the non-rigid transformation they cannot guarantee that the transformation is diffeomorphic. Therefore, apart from the regularization constraints, additional constraints have to be imposed such that the minimization of the data term (see Eq. 2.1) is performed in the space of diffeomorphisms. Most of the existing works on deformable registration methods do not attempt to estimate diffeomorphic deformation fields. However, there do exist a few diffeomorphic deformable registration methods employing the following two basic frameworks to compute diffeomorphic non-rigid transformations:

- **Large deformations diffeomorphic metric mapping** (**LDDMM**): In this approach [36], [12], the diffeomorphic transformation φ is generated as the endpoint $\varphi = \phi(1)$ of a path $\phi(t)$ in the space of diffeomorphisms which is obtained as solution of the ordinary differential equation (ODE) $\dot{\phi} = \mathbf{v}_t(t, \phi(t))$ with an initial condition $\phi(0) = \mathrm{Id}$, where $\mathbf{v}_t : [0\ 1] \rightarrow T$ is a *time-dependent velocity field* and Id is the identity transformation. T is the tangent space of the Riemannian manifold corresponding to the space of diffeomorphisms.

- **Stationary velocity fields** (**SVF**): Here [51], [8], [121], [122], *stationary velocity fields*, i.e. time-independent velocity fields, $\mathbf{v} \in T$ are employed instead of the time-dependent velocity fields $\mathbf{v}_t : [0\ 1] \rightarrow T$ and the diffeomorphic transformation φ is computed by the exponential map $\varphi = \exp(\mathbf{v})$ of the stationary velocity field $\mathbf{v}$.

Apart from the above mentioned two basic frameworks, there also have been efforts to construct diffeomorphic transformations by combining a set of locally affine transformations [7], [6].

In the following sections, we present a discussion on the existing deformable registration methods (including some of the diffeomorphic registration methods) structured according to the regularization strategy employed. The major works discussed in this review are summarized in Table 2.1.

2.1.1 Non-parametric approaches

Among the non-parametric approaches, the *variational* approaches incorporate the regularizer directly as an additional term into Eq. 2.1, whereas in contrast the *demons* approaches smooth the deformation field using the regularizer in a separate step.

Deformable registration methods		Deformable models in segmentation	
Non-parametric	Parametric	Non-parametric	Parametric
Variational [15],[25], [72],[41] Demons [117],[81],[19], [112],[121],[122]	Radial basis [90], [94] B-spline [101],[99], [91],[50],[110] FEM [40],[89],[56],[84] DFT [4],[26] DCT [9]	Level set (Implicit): Edge-based [20],[21] Region-based: [23],[79],[80],[16] Template-based: TGCV [102], TCV [65]	Explicit: Snakes [60] Balloon [29] GVF [133] AVM [107] FEM snakes [30],[39] B-spline snakes [68] AVM-FEM [106] Fourier [114], SH [61], [11], SW [77] snakes Template-based: Metamorphs [55] Active-image [67]

Table 2.1: Summary of the various deformable registration methods and the segmentation methods using deformable models

Variational approaches

In the variational approach to deformable registration an energy functional consisting of the data term E_D and the regularizer E_R is minimized:

$$E[\mathbf{U}] = E_D[\mathbf{U}; I_T, I_S] + \gamma E_R[\mathbf{U}], \tag{2.2}$$
$$\mathbf{U}^* = \underset{\mathbf{U}}{\operatorname{argmin}}\ E[\mathbf{U}],$$

where the regularization parameter γ controls the relative weighting of the data and regularization terms. The minimization of the above energy functional is typically performed by solving the corresponding Euler-Lagrange equation of the functional E which is a non-linear partial differential equation (PDE) of the form [72]:

$$\mathcal{A}[\mathbf{U}] - f(\mathbf{U}) = 0, \tag{2.3}$$

where $f(\mathbf{U})$ is known as the *force* and corresponds to the functional or variational derivative (gradient) of the data term, i.e., $f(\mathbf{U}) = \nabla_{\mathbf{U}} E_D = (I_S(\mathbf{x}+\mathbf{U}) - I_T(\mathbf{x}))\nabla I_S|_{(\mathbf{x}+\mathbf{U})}$ and $\mathcal{A}$ is a partial differential operator corresponding to the variational derivative of the regularizer such that $\mathcal{A}[\mathbf{U}] = \gamma \nabla_{\mathbf{U}} E_R$. Here, $\nabla_{\mathbf{U}}$ denotes the variational derivative operator with respect to $\mathbf{U}$. The above non-linear PDE is typically solved by setting up a semi-implicit fixed-point iteration scheme $\mathcal{A}[\mathbf{U}^{k+1}] = f(\mathbf{U}^k)$. Alternatively, an explicit gradient descent scheme $\mathbf{U}^{k+1} = \mathbf{U}^k - \tau(\mathcal{A}[\mathbf{U}^k] - f(\mathbf{U}^k))$ can also be employed [72].

In the earliest work on variational deformable registration, Broit [15] introduced the concept of *elastic* regularization, where he considered the template and source images as two different instances of an elastic body before and after deformation respectively. The deformations were modeled using a linear elastic model and the deformation model was introduced into the variational framework by

choosing the linear elastic potential as the regularizer:

$$E_R = E_R^{\text{elas}}[\mathbf{U}] = \int_{\Omega_T} \varrho_1 \,\text{trace}(\text{St}^{\text{lin}}[\mathbf{U}]^{\text{T}}\text{St}^{\text{lin}}[\mathbf{U}]) + \frac{\varrho_2}{2}\,\text{trace}(\text{St}^{\text{lin}}[\mathbf{U}])^2 \, d\mathbf{x}, \qquad (2.4)$$
$$\text{with} \quad \text{St}^{\text{lin}}[\mathbf{U}] = \frac{1}{2}(\nabla\mathbf{U} + \nabla\mathbf{U}^{\text{T}}),$$

where St^{lin} is the linear strain tensor and ϱ_1, ϱ_2 are the Lamé constants. For the choice of the elastic regularizer the PDE is given by:

$$\mathcal{A}^{\text{elas}}[\mathbf{U}] - f(\mathbf{U}) = 0, \quad \text{where} \quad \mathcal{A}^{\text{elas}} = \varrho_1\triangle + (\varrho_1 + \varrho_2)\nabla\,\text{div}. \qquad (2.5)$$

The main drawback of elastic registration is that it does not allow large deformations. This is because the linear elasticity model is based on the assumption of infinitesimal deformations. Further, in the linear elasticity model the internal stress opposing the external force $f(\mathbf{U})$ increases monotonically with the strain and thus preventing larger deformations. To address this issue, Yanovsky et *al.* [135] proposed the use of a *nonlinear* elastic deformation model which would allow large deformations:

$$E_R^{\text{nlin}-\text{elas}}[\mathbf{U}] = \int_{\Omega_T} \varrho_1 \,\text{trace}(\text{St}^{\text{nlin}}[\mathbf{U}]^{\text{T}}\text{St}^{\text{nlin}}[\mathbf{U}]) + \frac{\varrho_2}{2}\,\text{trace}(\text{St}^{\text{nlin}}[\mathbf{U}])^2 \, d\mathbf{x}, \qquad (2.6)$$
$$\text{with} \quad \text{St}^{\text{nlin}}[\mathbf{U}] = \frac{1}{2}(\nabla\mathbf{U} + \nabla\mathbf{U}^{\text{T}} + \nabla\mathbf{U}^{\text{T}}\nabla\mathbf{U}),$$

where St^{nlin} is the *non-linear* strain tensor and ϱ_2, ϱ_2 are the Lamé constants. The direct computation of the Euler-Lagrange equation of $E_R^{\text{nlin}-\text{elas}}$ is cumbersome, therefore the variable splitting method [70] is used to aid in the minimization of Eq. 2.2. Alternatively, large deformations can also be obtained using the *viscous fluid* deformation model proposed by Christensen et *al.* [25], where the elastic regularization is enforced on the velocity field instead of the deformation field. This enables the fluid model to achieve the desired large deformations given enough time as the internal stress in the fluid model disappears over time. The PDE for the fluid registration is as follows:

$$\varrho_1\triangle\mathbf{v} + (\varrho_1 + \varrho_2)\nabla\,\text{div}\,\mathbf{v} - f(\mathbf{U}) = 0, \qquad (2.7)$$

where $\mathbf{v}$ denotes the velocity field, which is related to the deformation field $\mathbf{U}$ as $\partial_t\mathbf{U} = \mathbf{v} - \nabla\mathbf{U}\,\mathbf{v}$. Comparing Eq. 2.7 with Eq. 2.5 we can see that the fluid registration PDE is in fact obtained by applying the linear elastic operator $\mathcal{A}^{\text{elas}}$ to the velocity field $\mathbf{v}$.

In the spirit of the Horn-Schunck variational optic flow method [53], Fischer et *al.* [72] proposed the *diffusion*-based registration method, using a gradient-based regularizer:

$$E_R^{\text{diff}}[\mathbf{U}] = \frac{1}{2}\sum_{i=1}^{\nu}\int_{\Omega_T} \parallel \nabla U_i \parallel^2 \, d\mathbf{x}, \qquad (2.8)$$

where $\mathbf{U} = [U_i]_{i=1}^{\nu}$. In contrast to elastic and fluid regularizations, the diffusion based regularization is not physically motivated but motivated by the smoothing properties of the Laplacian (or diffusion) operator $\triangle$, which results from the Euler-Lagrange equation of the diffusion regularizer:

$$\mathcal{A}^{\text{diff}}[\mathbf{U}] - f(\mathbf{U}) = 0, \quad \text{where} \quad \mathcal{A}^{\text{diff}} = \gamma\triangle. \qquad (2.9)$$

The diffusion regularizer essentially minimizes the oscillations in first-order derivative (the gradient) in order to smooth the deformation field. In [41], Fischer et *al.* explored the use of second-order derivative to characterize the smoothness of the deformation field and proposed the *curvature* regularizer:

$$E_R^{\text{curv}}[\mathbf{U}] = \frac{1}{2}\sum_{i=1}^{\nu}\int_{\Omega_T}(\triangle U_i)^2\, d\mathbf{x}, \tag{2.10}$$

where $\mathbf{U} = [U_i]_{i=1}^{\nu}$. Here, the term $(\triangle U_i)^2$ can be seen as an approximation to the curvature of the components of the deformation field. The main advantage of curvature based registration is that, in contrast to the other deformable registration methods it is less sensitive to the initial affine pre-registration step. This is because the curvature regularizer E_R^{curv} does not penalize affine transformations, i.e., $E_R^{\text{curv}}[C\mathbf{x} + \mathbf{b}] = 0$ for all $C \in \mathbb{R}^{\nu\times\nu}$, $\mathbf{b} \in \mathbb{R}^{\nu}$. The PDE for the curvature based registration is given by:

$$\mathcal{A}^{\text{curv}}[\mathbf{U}] - f(\mathbf{U}) = 0, \quad \text{where} \quad \mathcal{A}^{\text{curv}} = \gamma\triangle^2. \tag{2.11}$$

Demons approaches

The basic idea in a demons approach to deformable registration is to decouple the minimization of the data term E_D (see Eq. 2.1) from the smoothing of the deformation field using the regularizer E_R. This is in contrast to the variational approach, where the minimization of the combined data and regularization terms is performed.

In the seminal paper [117], Thirion presented the original formulation of the demons algorithm motivated by an analogy to Maxwell's demons. However, this formulation was based on heuristics, where image forces derived from optic flow equations were iteratively added to the current estimate of the deformation field and in each iteration Gaussian smoothing of the deformation field was performed. Subsequently, Pennec et *al.* [81] proposed a more rigorous formulation of the demons algorithm, where they showed that the image forces in the Thirion's demons algorithm were equivalent to minimizing the data term E_D using an approximate second-order gradient descent method. Further, they proposed two variants of the demons algorithm, the *elastic demons* in which the deformation field is smoothed (same as the original demons by Thirion) and the *fluid demons* in which the update to the deformation field is smoothed. The smoothing was performed by convolution with a Gaussian kernel G_σ. In [72], Modersitzki showed that smoothing by Gaussian convolution is equivalent to diffusion regularization E_R^{diff}. In [19], Cahill et *al.* extended this idea of equivalence to the curvature E_R^{curv} and elastic E_R^{elas} regularizers and devised the corresponding smoothing kernels for the curvature and elastic regularizers respectively. To summarize, the contributions of the above discussed works in the general demons registration algorithm are shown in Algorithm 1.

Over the past few years, a few extensions to the general demons algorithm (see Algorithm 1) have been proposed. In [112], Stefanescu et *al.* replaced the additive update in step 5 with the *compositional* update ($\mathbf{U}^{k+1} \leftarrow \mathbf{U}^k \circ \mathbf{u}^k$) and accordingly the warped gradient of the source image

Algorithm 1 General Demons registration

Require: I_S, I_T, E_R
Ensure: $\mathbf{U}^*$

1: At iteration $k = 0$, initialize $\mathbf{U}^0$
2: **while** convergence not reached **do**
3: $\mathbf{u}^k = -\mathcal{F}(\nabla_{\mathbf{U}} E_D[\mathbf{U}^k])$ $= -\mathcal{F}((I_S(\mathbf{x} + \mathbf{U}^k) - I_T(\mathbf{x}))\nabla I_S|_{(\mathbf{x}+\mathbf{U}^k)})$ //compute the update to the deformation field using some function $\mathcal{F}(.)$ of the gradient of the data term E_D
4: $\mathbf{u}^k \leftarrow K_R * \mathbf{u}^k$ //fluid smoothing, convolution kernel K_R corresponds to the regularizer E_R
5: $\mathbf{U}^{k+1} \leftarrow \mathbf{U}^k + \mathbf{u}^k$ //update the current estimate of the deformation field
6: $\mathbf{U}^{k+1} \leftarrow K_R * \mathbf{U}^{k+1}$ //elastic smoothing, convolution kernel K_R corresponds to the regularizer E_R
7: **end while**

$\nabla I_S|_{(\mathbf{x}+\mathbf{U}^k)}$ in step 3 was replaced with the gradient of the warped source image $\nabla I_S(\mathbf{x} + \mathbf{U}^k)$. They, empirically justified the better performance of the compositional update. Further, in their work smoothing of the deformation and update fields (steps 4, 6) was performed by solving a diffusion equation instead of convolution with a Gaussian kernel (which is equivalent to the simple linear diffusion regularizer E_R^{diff}). We can see that the general demons algorithm performs optimization (of the data term) on the entire space of deformation fields. Hence, the deformation fields estimated using the general demons algorithm are not guaranteed to be diffeomorphic. In order to compute diffeomorphic deformation fields, Veracauteren et *al.* [121] proposed the *diffeomorphic demons* algorithm which adapts the general demons algorithm to the space of diffeomorphic transformations, using the concept of stationary velocity fields. In the diffeomorphic demons algorithm, at each iteration the update $\mathbf{u}^k$ in step 3 is computed in the space of the stationary velocity fields and then mapped into the space of diffeomorphisms using the exponential map of the velocity field update, i.e., $\mathbf{u}^k \rightarrow \exp(\mathbf{u}^k)$. Then, accordingly, the additive update in step 5 is replaced with $\mathbf{U}^{k+1} \leftarrow \mathbf{U}^k \circ \exp(\mathbf{u}^k)$, which ensured a final diffeomorphic deformation field. In a subsequent work, Veracauteren et *al.* [122] proposed an extension to the diffeomorphic demons algorithm where the current deformation field $\mathbf{U}^k$ itself is represented as an exponential of a smooth velocity field $\mathbf{v}^k$, i.e., $\mathbf{U}^k = \exp(\mathbf{v}^k)$. The advantage of this representation is that the "true" inverse of the deformation field can simply be written as $\mathbf{U}^{-\mathbf{1}^k} = \exp(-\mathbf{v}^k)$. The deformation field and its true inverse were then computed using the diffeomorphic demons approach employing a symmetric data term $\hat{E}_D = E_D[\mathbf{U}; I_T, I_S] + E_D[\mathbf{U}^{-1}; I_T, I_S]$.

2.1.2 Parametric approaches

In the parametric approach to deformable registration, the deformation field $\mathbf{U}$ (or the non-rigid transformation φ itself) is parametrized using a finite set of basis functions $B_n : \Omega_T \rightarrow \mathbb{R}$, $n \in$

$\{1, 2, \ldots, N\}$ as:

$$\mathbf{U}(\mathbf{x})\,(\text{or}\,\varphi(\mathbf{x})) = \sum_{n=1}^{N} \boldsymbol{\alpha}_n B_n(\mathbf{x}), \quad \forall\, \mathbf{x} \in \Omega_T, \tag{2.12}$$

where $\{\boldsymbol{\alpha}_n\}_{n=1}^{N}$, $\boldsymbol{\alpha}_n \in \mathbb{R}^{\nu}$ are the basis coefficients which are considered as the *parameters*. The minimization problem corresponding to the deformable registration task in Eq. 2.1 can now be re-formulated as:

$$\{\boldsymbol{\alpha}_n^*\}_{n=1}^{N} = \underset{\{\boldsymbol{\alpha}_n\}_{n=1}^{N}}{\text{argmin}}\ E_D[\mathbf{U}\,(\text{or}\,\varphi); I_T, I_S], \tag{2.13}$$

i.e., find the optimal set of parameters $\{\boldsymbol{\alpha}_n^*\}_{n=1}^{N}$, $\boldsymbol{\alpha}_n^* \in \mathbb{R}^{\nu}$ such that the data term E_D is minimized. Thus, parametric deformable registration is posed as a finite-dimensional optimization problem. In general, the numerical solution to the above problem can be obtained using any of the standard optimization methods, e.g. gradient descent, Gauss-Newton, LevenbergMarquardt etc. Furthermore, additional regularization is often enforced on $\mathbf{U}(\,\text{or}\,\varphi)$ through the use of regularizers $E_R[\mathbf{U}\,(\text{or}, \varphi)]$ either by adding them directly to the data term and performing the minimization similar to the variational approach or by employing them in a separate step similar to the demons approach.

In the following sections, we present a discussion on some of the existing approaches for parametric deformable registration. These approaches can be broadly divided into two groups based on the type of the basis functions used in the parametrization of the deformation field [141]. The first group consists of approaches that employ *local* basis functions, where each of the basis functions $B_n(\mathbf{x})$ has a compact support centered around a point $\mathbf{x}_n \in \Omega_T$. The second group contains approaches that use *global* basis functions which do not have a particular center of influence. Below, we discuss a few representative methods from each of the two groups. For, local basis approaches: parametrization by the radial basis functions (RBF), the B-spline based free form deformations (FFD) and the finite element method (FEM) basis functions. For global basis approaches: parametrization based on trigonometric functions, e.g. Fourier series basis and discrete cosine transform basis functions.

Local basis

Radial basis functions The radial basis functions (RBFs) depend on the distance between a given point $\mathbf{x}$ and basis function center $\mathbf{x}_n$, such that $B_n^{\text{RBF}}(\mathbf{x}) := B_n^{\text{RBF}}(\parallel \mathbf{x} - \mathbf{x}_n \parallel)$, where $\parallel . \parallel$ is the Euclidean norm. Traditionally, RBFs have been used for landmark-based parametric registration, where a set of user-defined correspondences between the landmark points (chosen as some salient image features) in the template and source images $\{\mathbf{x}_n\}_{n=1}^{N} \rightarrow \{\mathbf{y}_n\}_{n=1}^{N}$, $\mathbf{x}_n \in \Omega_T, \mathbf{y}_n \in \Omega_S$ are used to estimate the non-rigid transformation φ such that the constraints $\varphi(\mathbf{x}_n) = \mathbf{y}_n$, $\forall\, n \in \{1, 2, \ldots, N\}$ are satisfied. In [92], [93], Rohr et *al.* employed the thin-plate spline (TPS) based RBFs ($B_n^{\text{RBF-TPS}}(r) = r^2 \log r$) and Fornefett et *al.* [42] employed Wendland function based RBFs [130] to parametrize φ for landmark-based registration of medical images. A disadvantage of the

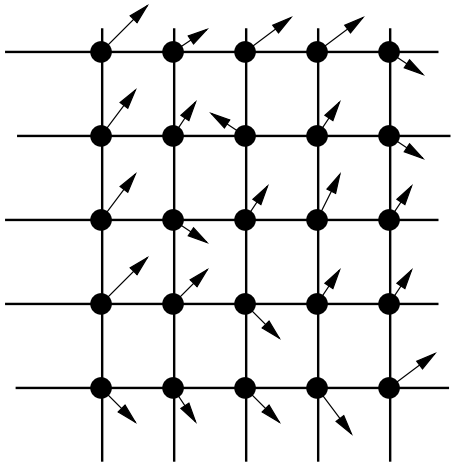

Figure 2.2: An uniform B-spline FFD lattice undergoing deformation.

RBF based parameterization is that the local spatial influence of the non-rigid transformation φ cannot be controlled, except through the introduction of additional landmark points, which is impractical. In order to overcome this limitation, recently Rohr et *al.* [94] proposed a new type of RBFs called the Gaussian thin-plate splines (GTPS):

$$B_n^{\mathrm{RBF-GTPS}}(r) = -\frac{1}{8\pi}\left(4\pi\sigma^4 G_\sigma(r) + \left(r + \frac{\sigma^2}{r}\right)\mathrm{erf}\left(\frac{r}{\sqrt{2}\sigma}\right)\right), \tag{2.14}$$

where $\mathrm{erf}(r) = (\frac{2}{\sqrt{\pi}})\int_0^r \exp(-\xi^2)\, d\xi$ is the error function and $G_\sigma(r) = \frac{1}{(\sqrt{2\pi}\sigma)^\nu}\exp(-\frac{r^2}{2\sigma^2})$ is the Gaussian kernel. It is possible to control the local influence of the GTPS based RBFs by varying the standard deviation σ of the Gaussian kernel. Note that landmark-based registration differs from the intensity-based registration approaches discussed until now, that use a data term E_D measuring the similarity between the template and source images in the intensity space. However, Rohde et *al.* [90] have used RBFs for intensity-based parametric registration of medical images. In their work, RBFs proposed by Wu [131] ($B_n^{\text{RBF-WU}}(r) = \max(1-r, 0)\,(3r^3 + 12r^2 + 16r + 4),\ \forall\, r \geq 0$) were used to parametrize the deformation field $\mathbf{U}$ (instead of φ) and the Normalized Mutual Information (NMI) similarity metric was used as the data term.

B-spline free form deformations In the B-spline based free from deformation (FFD) registration approach the deformation field is essentially parametrized using the deformation field values at a set of regularly spaced control points. Consider a *uniform* lattice of N control points $\boldsymbol{\Upsilon} = \{\mathbf{x}_{i,j,k} = (x_{i,j,k}, y_{i,j,k}, z_{i,j,k})\}_{i=1,j=1,k=1}^{N_x,N_y,N_z}$, $N = N_x \times N_y \times N_z$ overlaid on the the 3D image domain $\Omega_T = \{\mathbf{x} = (x, y, z) | 0 \leq x \leq X, 0 \leq x \leq 0 \leq x \leq Y, 0 \leq x \leq Z\}$ as shown in see Figure 2.2. The B-spline based free form deformations (FFD) basis functions $B_{i,j,k}^{\mathrm{FFD}}$ corresponding to each lattice point can then be written as a 3D tensor product of one-dimensional cubic B-spline basis functions

$B^{\mathrm{B-spline}} := \{b_0, b_1, b_2, b_3\}$:

$$B^{\mathrm{FFD}}_{i,j,k}(\mathbf{x}) = \begin{cases} b_{i-l}(u)b_{j-m}(v)b_{k-n}(w) & \text{if } 0 \leq i-l, j-m, k-n \leq 3, \\ 0 & \text{otherwise,} \end{cases} \tag{2.15}$$

where $l = \lfloor \frac{x}{X}(N_x - 1) \rfloor + 1$, $m = \lfloor \frac{y}{Y}(N_y - 1) \rfloor + 1$, $n = \lfloor \frac{z}{Z}(N_z - 1) \rfloor + 1$ and $u = \frac{x}{X}(N_x - 1) - \lfloor \frac{x}{X}(N_x - 1) \rfloor$, $v = \frac{y}{Y}(N_y - 1) - \lfloor \frac{y}{Y}(N_y - 1) \rfloor$, $w = \frac{z}{Z}(N_z - 1) - \lfloor \frac{z}{Z}(N_z - 1) \rfloor$ and the cubic B-spline basis functions are given by $b_0(u) = \frac{(1-u)^3}{6}, b_1(u) = \frac{3u^3 - 6u^2 + 4}{6}, b_2(u) = \frac{-3u^3 + 3u^2 + 3u + 1}{6}, b_3(u) = \frac{u^3}{6}$. From the above we can see that the span of the support of each basis function is four lattice points in each direction.

In a popular work, Rueckert et *al.* [101] employed the FFD basis functions for the registration of breast MRI images where they parametrized the non-rigid transformation φ as:

$$\varphi(\mathbf{x}) = \sum_{i=1}^{N_x} \sum_{j=1}^{N_y} \sum_{k=1}^{N_z} \mathbf{x}_{i,j,k} B^{\mathrm{FFD}}_{i,j,k}(\mathbf{x}). \tag{2.16}$$

Here, the coordinates of the lattice points ($\boldsymbol{\Upsilon} = \{\mathbf{x}_{i,j,k}\}_{i=1,j=1,k=1}^{N_x,N_y,N_z}$) are the unknown parameters that were estimated through the minimization of an energy based on the Normalized Mutual Information (NMI) for data term and an additional smoothing term given by the bending energy:

$$E_R^{\mathrm{bending}}[\varphi] = \int_{\Omega_T} [(\partial^2_{xx}\varphi)^2 + (\partial^2_{yy}\varphi)^2 + (\partial^2_{zz}\varphi)^2 + 2(\partial^2_{xy}\varphi)^2 \ldots \\ \ldots + 2(\partial^2_{yz}\varphi)^2 + 2(\partial^2_{zx}\varphi)^2]\, d\mathbf{x}. \tag{2.17}$$

The minimization was performed using a multiresolution framework in which the resolution of the lattice $\boldsymbol{\Upsilon}$ was increased in a coarse-to-fine manner. In a later work, Rueckert et *al.* [99], proposed a diffeomorphic registration method based on their FFD registration methodology. In this work, a diffeomorphic transformation was constructed by composing a sequence of FFD transformations, while ensuring that each of the individual FFD transformations was diffeomorphic by imposing constraints on the maximum displacement of the lattice points. Rohlfing et *al.* [91] showed an improved performance of the FFD registration method using the following Jacobian-based incompressibility regularization constraint instead of the above mentioned E_R^{bending} regularizer:

$$E_R^{\mathrm{incompress}}[\varphi] = \int_{\Omega_T} \log(J_\varphi(\mathbf{x})). \tag{2.18}$$

Recently, Shi et *al.* [110] found that instead of estimating the FFD deformations separately at each multi-resolution level, a more accurate solution is obtained by solving for the FFD deformations at all the levels simultaneously with a single energy minimization step while using an addtional sparsity constratint. Hansen et *al.* [50] extended FFD deformable registration to non-uniform lattices, where instead of the regularly placed points in uniform lattices, the density of these points is varied such that the resolution of the lattice is finer in image regions with salient features and it is coarser in the homogenous regions. They parametrized the deformation field using multivariate B-splines which can be defined on non-uniform lattices as opposed to the above discussed tensor product B-splines that correspond to uniform lattices.

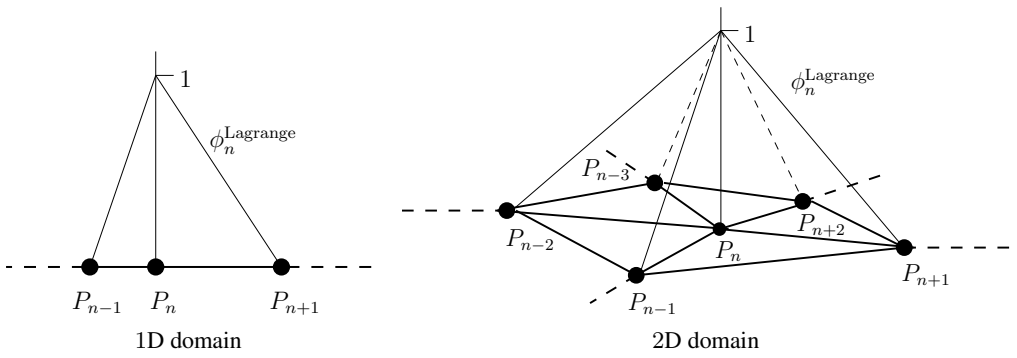

Figure 2.3: Illustration of the Lagrange nodal basis function.

Finite element method Consider a discrete tesselation $\mathcal{M} = (\{P_n\}_{n=1}^N, \Delta_h)$ of the template domain Ω_T, where $\{P_n\}_{n=1}^N$ denote the nodes of the mesh and Δ_h is the set of elements (triangles in 2D and tetrahedra in 3D). The deformation field $\mathbf{U}$ can be approximated by a set of finite element method (FEM) basis functions $\{B_n^{\text{FEM}} := \phi_n^{\text{Lagrange}}\}_{n=1}^N$, which are commonly chosen as piece-wise linear polynomials (but sometimes also chosen as quadratic piece-wise polynomials):

$$\mathbf{U}(\mathbf{x}) = \sum_{n=1}^{N} \mathbf{U}_n \phi_n^{\text{Lagrange}}(\mathbf{x}), \qquad \forall\, \mathbf{x} \in \Omega_T, \tag{2.19}$$

where $\mathbf{U}_n$ is the value of deformation field at the node P_n. We assign a piece-wise linear basis function ϕ_n^{Lagrange} to each node P_n which is uniquely defined as (see Figure 2.3):

$$\phi_n^{\text{Lagrange}}(\mathbf{x}) = \begin{cases} & \text{is linear within each adjacent element,} \\ 1 & \text{at each node } P_n, \\ 0 & \text{at every other node } P_m \neq P_n. \end{cases} \tag{2.20}$$

Here, we note that the nodal deformations $\{\mathbf{U}_n\}_{n=1}^N$ are the unknown parameters that need to be estimated.

The FEM-based approach is in general suitable for deformable registration (and especially for medical image registration) because it naturally allows for the use of non-uniform meshes adapted to the salient features (anatomical structures) in the image. Such adaptive non-uniform meshes can improve both the computational efficiency and accuracy of the solution to the deformable registration task. Despite the attractiveness of the FEM-based approach, there exist relatively few works in the area of FEM-based deformable registration. In [40], Ferrant et *al.* proposed a FEM-based elastic registration method, where they employed the linearized SSD data term $E_D^{\text{LIN-SSD}} \approx \int_{\Omega_T} (I_S(\mathbf{x}) + \nabla I_S(\mathbf{x})\mathbf{U}(\mathbf{x}) - I_T(\mathbf{x}))^2\, d\mathbf{x}$ along with the linear elastic regularizer E_R^{elas} (see Eq. 2.4). Due to the linearization of the data term, setting the partial derivative of the energy with respect each of the N parameters $\{\mathbf{U}_n\}_{n=1}^N$ to zero, i.e, $\partial_{\mathbf{U}_n}(E_D^{\text{LIN-SSD}} + \gamma E_R^{\text{elas}}) = 0$ yields a system of N linear equations which were solved to obtain the nodal deformations $\{\mathbf{U}_n\}_{n=1}^N$ and hence the deformation field $\mathbf{U}$. Typically, determining the elasticity parameters (Lamé constants) ϱ_2

and ϱ_1 involved in the elastic regularizer E_R^{elas} is a difficult task (especially for the various tissues in medical image registration). Recently, Risholm et *al.* [89] proposed a Markov Chain Monte Carlo (MCMC) optimization approach for FEM-based elastic registration to simultaneously estimate the elasticity parameters along with the deformation field parameters. Apart from the linear elastic regularizer, more complex regularizers based on constitutive models have been proposed [56]. Popuri et *al.* [84] employed a simple diffusion-based regularization in a demons-like framework for FEM-based deformable registration.

Global basis

As an alternative to the local basis parametrization of the deformation fields, there have been works that parametrize the deformation fields using trigonometric functions which have a global support [141]. The basic idea in these works is to parametrize the deformation field using either a discrete Fourier transformation (DFT) [4], [26] or a discrete cosine transform (DCT) [9]. The basis functions $\{B_n^{\text{DFT}}\}_{n=1}^N$ and $\{B_n^{\text{DCT}}\}_{n=1}^N$ corresponding to the DFT and DCT parametrization respectively essentially represent signals of frequency $n = \{1, 2, \ldots, N\}$ (see [4] and [9] for definitions of the B_n^{DFT} and B_n^{DCT} respectively). Typically, these N frequencies are chosen from the low-frequency end of the spectrum. This provides an inherent regularization of the deformation field as only smooth functions are generated by the linear combination of such low-frequency basis functions. Another motivation for the use of trigonometric basis functions is that the trigonometric basis form the eigenfunctions of the operator $\mathcal{A}$ correspond to the variational derivative of the regularizer E_R, which facilitates in the solution of the Euler-Lagrange equation in Eq. 2.3.

2.2 Deformable models in image segmentation

Image segmentation in general refers to the task of partitioning an image $I : \Omega \rightarrow \mathbb{R}$ into "meaningful" regions. More specifically in the context of medical imaging, segmentation involves the delineation of the various anatomical structures (or tissues) present in the medical image. Deformable models have been widely used for medical image segmentation with considerable success. A deformable model is basically a closed *curve* $\mathcal{C}$ defined on the image domain Ω. The goal of image segmentation using a deformable model can be formulated as finding an optimal curve $\mathcal{C}^*$ that aligns with the boundary of the object of interest in the image such that an energy E is minimized :

$$\begin{aligned} E[\mathcal{C}] &= E_{\text{image}}[\mathcal{C}; I] + \gamma E_{\text{smooth}}[\mathcal{C}], \\ \mathcal{C}^* &= \underset{\mathcal{C}}{\operatorname{argmin}}\ E[\mathcal{C}], \end{aligned} \tag{2.21}$$

where E_{image} is the *image-based* energy term that incorporates edge/gradient information (edge-based) or region intensity statistics (region-based) derived from the image data, E_{smooth} is the *smoothness-based* energy term that purely contains regularization constraints defined on the curve and γ is the regularization parameter that controls the relative weighting between the two terms.

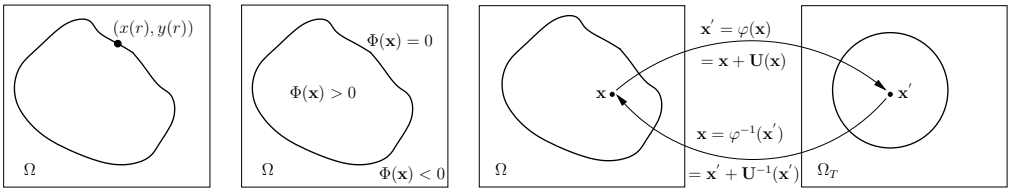

(a) Explicit representation (b) Implicit representation (c) Template-based representation

Figure 2.4: Different representations of the curve $\mathcal{C}$ employed by the deformable models in segmentation.

The minimization of the energy E in Eq. 2.21 is typically performed using a gradient descent strategy. Thus, starting with an initialization $\mathcal{C} \equiv \mathcal{C}^0$, the deformable model given by the curve $\mathcal{C}$ is deformed according to the following evolution equation:

$$\partial_t \mathcal{C} = \mathbf{f}_{\text{image}}(\mathcal{C}) + \mathbf{f}_{\text{smooth}}(\mathcal{C}), \tag{2.22}$$

until a local minimum of E at $\mathcal{C} \equiv \mathcal{C}^*$ is reached, corresponding to the segmentation of the image. In the above, $\mathbf{f}_{\text{image}} = -\nabla_{\mathcal{C}} E_{\text{image}}$ is the *image-based* force that drives the deformable model towards the boundary of the object of interest in the image and $\mathbf{f}_{\text{smooth}} = -\gamma \nabla_{\mathcal{C}} E_{\text{smooth}}$ is the *smoothness-based* force that keeps the deformable model smooth during evolution. Here, $\nabla_{\mathcal{C}}$ denotes the gradient with respect to the curve $\mathcal{C}$.

In the practical application of the image segmentation framework using deformable models, the most important choice to be made is the representation of deformable model itself, meaning the representation of the curve $\mathcal{C}$. This choice determines the space in which the minimization of the energy E (see Eq. 2.21) is performed. That is, if the deformable model is represented using a specific parametrization, then the optimal curve is searched in the space of parameters corresponding to that parametrization. Such deformable models are called as *parametric deformable models* in this review. On the contrary if the deformable model is represented in a "parameter-free" manner using a function belonging to a particular class of functions defined on the image domain, then the optimization is restricted to the space of that function class. Such deformable models are referred to as *non-parametric deformable models* in this review.

In the last few decades, numerous deformable models have been proposed for the purpose of image segmentation under various names like snakes, active contours, balloons, active regions, metamorphs etc. Among these deformable models, we encounter three particular representations of the curve $\mathcal{C}$ (see Figure 2.4). In the following, we discuss each of these representations in the context of the above introduced dichotomy of parametric and non-parametric models:

- **Explicit representation**: The curve $\mathcal{C}$ is represented using a vector function $\mathbf{\Gamma} : [0\ 1] \rightarrow \Omega$, such that for $r \in [0\ 1]$, $\mathbf{\Gamma}(r) = (x(r), y(r))$ are points on $\mathcal{C}$ (see Figure 2.4a). In this representation, the point coordinates $(x(r), y(r)),\ r \in [0\ 1]$ are considered as the parameters. Further, the function $\mathbf{\Gamma}$ can itself be expressed in terms of a finite set of basis functions, i.e.,

$\mathbf{\Gamma}(r) = \sum_{n=1}^{N} \boldsymbol{\alpha}_n B_n(r)$, $r \in [0\ 1]$. In this case, the curve is parametrized using the finite set of basis function coefficients $\{\boldsymbol{\alpha}_n\}_{n=1}^{N}$. Hence, in deformable models that use an explicit representation of the curve $\mathcal{C}$, the energy minimization is performed either in the space of the point coordinate parameters $(x(r), y(r))$, $r \in [0\ 1]$ or in the space of the basis function coefficient parameters $\{\boldsymbol{\alpha}_n\}_{n=1}^{N}$, which places the explicit representation based deformable models in the group of parametric deformable models.

- **Implicit representation**: The curve $\mathcal{C}$ is encoded as a zero isocontour of the *level set* function $\Phi : \Omega \rightarrow \mathbb{R}$, i.e., $\mathcal{C} = \{\mathbf{x} | \Phi(\mathbf{x}) = 0, \mathbf{x} \in \Omega\}$ (see Figure 2.4b), where the function Φ is commonly chosen as the *signed distance* function [78]. Therefore, in deformable models that employ an implicit representation of the curve $\mathcal{C}$, the energy optimization is carried out in the space of level set functions and thus the implicit representation based deformable models can be categorized as non-parametric deformable models. In practice the computation is limited to only a narrow band around the zero level set.

- **Template-based representation**: The curve $\mathcal{C}$ is represented using a *template image* (or simply *template*) $I_T : \Omega_T \rightarrow \mathbb{R}$ which is deformed through a deformation field $\mathbf{U} : \Omega \rightarrow \Omega_T$ (see Figure 2.4c). The template I_T essentially embeds the *topological shape* of the curve $\mathcal{C}$ using either a level set function (signed distance function) or a binary image. The curve $\mathcal{C}$ is then embedded into the warped template $I_T \circ \varphi : \Omega \rightarrow \Omega_T$, where $\varphi : \Omega \rightarrow \Omega_T$ is the transformation corresponding to the deformation field $\mathbf{U}$, such that $\varphi(\mathbf{x}) = \mathbf{x} + \mathbf{U}(\mathbf{x})$ and $(I_T \circ \varphi)(\mathbf{x}) = I_T(\varphi(\mathbf{x})) = I_T(\mathbf{x} + \mathbf{U}(\mathbf{x}))$, $\forall\, \mathbf{x} \in \Omega$. Thus, in deformable models that employ a template-based representation of the curve $\mathcal{C}$, the segmentation energy E in Eq. 2.21 is optimized over the space of the deformation fields (or directly over the space of transformations). This optimization task can be performed using any of the deformable registration approaches discussed previously in Section 2.1. We can then classify the deformable models using the template-based representation of the curve as non-parametric or parametric deformable models depending on whether non-parametric or parametric deformable registration models are used for energy optimization. We note that alternatively the curve $\mathcal{C}$ can also be represented through the inverse transformation $\varphi^{-1} : \Omega_T \rightarrow \Omega$ and the corresponding inverse deformation field $\mathbf{U}^{-1} : \Omega \rightarrow \Omega_T$, where $\varphi^{-1}(\mathbf{x}') = \mathbf{x}' + \mathbf{U}^{-1}(\mathbf{x}')$. Although, the representation of the curve $\mathcal{C}$ using the inverse transformation might seem un-intuitive, it is popularly used by the parametric deformable models which employ local basis functions. This is because it facilitates the use of a discrete mesh (or lattice) overlaid on the template domain on which the local basis functions can be conveniently defined.

In the next sections, we present a review on some of the existing non-parametric and parametric deformable models in image segmentation.

We note that the discussion until now pertained to 2D deformable models (i.e. deformable

curves). However, the general energy minimization based segmentation framework using 2D deformable models presented above is also applicable to 3D deformable models (i.e. deformable surfaces). Likewise, even though most of the segmentation techniques presented in the following sections are discussed in the context of 2D deformable models, they can be readily extended to 3D deformable models as well.

2.2.1 Non-parametric deformable models

The non-parametric deformable models can be further divided into two groups based on whether the segmentation is being driven by the edge or region information in the image. Below, we discuss both the edge- and region-based non-parametric deformable models. In all the non-parametric deformable models discussed below, the implicit representation of the curve is employed with the exception of works by Saddi et *al.* [102] and Le Guyader et *al.* [65], where a template-based representation of the curve is used.

Edge-based

The edge-based non-parametric deformable models essentially perform segmentation by evolving a curve in the direction of its *normal* with a speed dependent on the *curvature* until it encounters an edge in the image. According to the energy minimization based segmentation framework described in the previous section, segmentation using the edge-based non-parametric deformable model can be described as minimizing the *curve length* (length of the curve) subject to the edge-based constraints derived from the image. Using the implicit level set representation (see Figure 2.4b), consider a segmentation energy containing just the smoothness-based term, which is chosen as the length of the curve $\mathcal{C}$:

$$E^{\text{Length}}[\Phi] = E^{\text{Length}}_{\text{smooth}}[\Phi] = \text{Length}(\mathcal{C}) = \int_{\Omega} |\nabla H(\Phi(\mathbf{x}))|\, d\mathbf{x}, \tag{2.23}$$

where $H(.)$ is the *Heaviside* function defined as: $H(\Phi) = 1$ if $\Phi \geq 0$ and $H(\Phi) = 0$ if $\Phi < 0$. The evolution of a non-parametric deformable model according to the above energy is given as:

$$\partial_t \Phi = \mathbf{f}^{\text{Length}}_{\text{smooth}}[\Phi] = \text{div}\left(\frac{\nabla\Phi}{|\nabla\Phi|}\right)|\nabla\Phi| = \kappa|\nabla\Phi|, \tag{2.24}$$

where $\kappa = \text{div}\big(\frac{\nabla\Phi}{|\nabla\Phi|}\big)$ is the curvature of the curve $\mathcal{C}$. The above evolution is known as the *mean curvature* motion, where the smoothness-based force $\mathbf{f}^{\text{Length}}_{\text{smooth}}$ moves the non-parametric deformable model with a speed proportional to the curvature κ in the direction of the normal to the curve. In order to perform segmentation, the edge-based non-parametric deformable models either incorporate an edge detector into the energy $E^{\text{Length}}_{\text{smooth}}$ or directly modify the force $\mathbf{f}^{\text{Length}}_{\text{smooth}}$ using an edge detector.

The earliest edge-based non-parametric deformable model for segmentation called *geometric active contour* was proposed by Caselles et *al.* [20], using a edge-detector of the form:

$$g(|\nabla I|) = \frac{1}{1 + |(\nabla G_\sigma * I)|}, \tag{2.25}$$

where G_σ is a Gaussian kernel. Note that $g(|\nabla I|) \to 0$ as $|\nabla I| \to \infty$, i.e., the edge detector takes very small values in the presence of edges, which are defined by high gradients in the image. In the geometric active contours model, a new force using the edge-detector was defined as:

$$\partial_t \Phi = F^{\text{geometric}}_{\text{smooth}}[\Phi] = g(|\nabla I|)\,\text{div}\left(\frac{\nabla \Phi}{|\nabla \Phi|}\right)|\nabla \Phi|. \tag{2.26}$$

In the above, the edge-detector is used as a multiplicative stopping-term which is supposed to stop the evolution of the curve near the edges. However, in practice this multiplicative stopping-term only slows down the evolution and in the absence of strong edges this stopping-term is unable to prevent the curve from "leaking" into the object boundary. To address this problem, in a subsequent work Caselles et *al.* [21] proposed the popular *geodesic active contour* (GAC) model, where the edge-detector is used to formulate an energy that corresponds to the curve length in a Riemannian space (according to a metric induced by the image) as:

$$E^{\text{GAC}}[\Phi] = E^{\text{GAC}}_{\text{smooth}}[\Phi] = \int_\Omega g(|\nabla I|)|\nabla \Phi|\, d\mathbf{x}. \tag{2.27}$$

The minimization of the above energy leads to the following evolution:

$$\partial_t \Phi = \mathbf{f}^{\text{GAC}}_{\text{smooth}}[\Phi] = g(|\nabla I|)\,\text{div}\left(\frac{\nabla \Phi}{|\nabla \Phi|}\right)|\nabla \Phi| + \nabla g \cdot \nabla \Phi. \tag{2.28}$$

Comparing the above GAC evolution equation with Eq. 2.26 we can see that there is an additional stopping-term $\nabla g \cdot \nabla \Phi$, that "pulls back" the curve in case it crosses the object boundary.

The main limitation of the above discussed edge-based non-parametric deformable models is that they are solely dependent on the edge information in the image and hence often fail (even the GAC model) when images do not have sufficient contrast between the object of interest and background (this is especially true for medical images). One way to address this issue is by introducing region-based information into the non-parametric deformable model.

Region-based

In the seminal work by Mumford et *al.* [75], the segmentation problem was modeled as partitioning the image into two *piecewise smooth* regions separated by the curve $\mathcal{C}$, where one of the regions corresponds the object of interest in the image and the other to the background. The Mumford-Shah (MS) functional for segmentation is given by:

$$E[\mathcal{C}, \tilde{I}] = E^{\text{MS}}_{\text{image}}[\mathcal{C}, \tilde{I}] + \gamma E^{\text{MS}}_{\text{smooth}}[\mathcal{C}], \tag{2.29}$$

$$\text{where} \quad E^{\text{MS}}_{\text{image}}[\mathcal{C}, \tilde{I}] = \int_\Omega (\tilde{I} - I)^2\, d\mathbf{x} + \beta \int_{\Omega \setminus \mathcal{C}} |\nabla \tilde{I}|^2\, d\mathbf{x} \quad \text{and} \quad E^{\text{MS}}_{\text{smooth}}[\mathcal{C}] = \text{Length}(\mathcal{C}),$$

where $\tilde{I}$ is the "solution" image containing the two piecewise smooth regions. A simplified version of the MS functional known as the *cartoon limit*, is obtained by setting $\beta = 0$ and replacing the piecewise smooth approximation with a *piecewise-constant* approximation. Based on the cartoon limit version of the MS functional and using the level set representation, Chan et *al.* [23] proposed

the extremely popular *Chan-Vese* (CV) region-based non-parametric deformable model for segmentation:

$$E^{\text{CV}}[\Phi] = E^{\text{CV}}_{\text{image}}[\Phi] + \gamma E^{\text{Length}}_{\text{smooth}}[\Phi], \tag{2.30}$$
$$\text{with} \quad E^{\text{CV}}_{\text{image}}[\Phi] = \int_{\Omega} H(\Phi)(I-\mu_1)^2 + (1-H(\Phi))(I-\mu_2)^2 \, d\mathbf{x},$$

where μ_1, μ_2 denote the mean intensities of the two piecewise constant regions $\Omega_1 = \{\mathbf{x}|\Phi(\mathbf{x}) >= 0, \mathbf{x} \in \Omega\}$ and $\Omega_2 = \{\mathbf{x}|\Phi(\mathbf{x}) < 0, \mathbf{x} \in \Omega\}$ respectively, which are separated by the curve $\mathcal{C} = \{\mathbf{x}|\Phi(\mathbf{x}) = 0, \mathbf{x} \in \Omega\}$. We also note that the Heaviside function $H(\Phi) = 1$ in region Ω_1 and $H(\Phi) = 0$ in region Ω_2. The evolution equation for the CV model is given by:

$$\partial_t \Phi = \mathbf{f}^{\text{CV}}_{\text{image}}[\Phi] + \gamma \mathbf{f}^{\text{Length}}_{\text{smooth}}[\Phi], \tag{2.31}$$
$$\text{with} \quad \mathbf{f}^{\text{CV}}_{\text{image}}[\Phi] = ((I-\mu_2)^2 - (I-\mu_1)^2)|\nabla\Phi|,$$

and the means of the regions Ω_1, Ω_2 are updated at every evolution step as:

$$\mu_1 = \frac{\int_{\Omega} I H(\Phi)\, d\mathbf{x}}{\int_{\Omega} H(\Phi)\, d\mathbf{x}}, \quad \mu_2 = \frac{\int_{\Omega} I(1-H(\Phi))\, d\mathbf{x}}{\int_{\Omega}(1-H(\Phi))\, d\mathbf{x}}. \tag{2.32}$$

Thus, the minimization of the CV energy attempts to find a smooth curve $\mathcal{C}$ that separates the image into two distinct regions Ω_1 (say object) and Ω_2 (say background) such that the corresponding means μ_1 and μ_2 are distinct while each of the regions Ω_1 and Ω_2 are as homogeneous as possible.

The CV model employs the simplest of statistics namely, the mean, to characterize the regional intensity information in the image. Consequently, the CV model is not appropriate to distinguish regions that are highly inhomogeneous, i.e., violate the piecewise constancy assumption and hence cannot be represented by a single mean value. One way to overcome this shortcoming is through the incorporation of more complex region statistics into the CV model. For this purpose, Paragios et *al.* [79] re-formulated the original CV model using a probabilistic framework, where image segmentation is posed as a Bayesian inference task and proposed the following *generalized Chan-Vese* (GCV) energy functional:

$$E^{\text{GCV}}[\Phi] = E^{\text{GCV}}_{\text{image}}[\Phi] + \gamma E^{\text{Length}}_{\text{smooth}}[\Phi], \tag{2.33}$$
$$\text{with} \quad E^{\text{GCV}}_{\text{image}}[\Phi] = \int_{\Omega} -H(\Phi)\log\, p_1 - (1-H(\Phi))\log\, p_2 \, d\mathbf{x},$$

where $p_1(\mathbf{x}) := p(I(\mathbf{x})|\mathbf{x} \in \Omega_1)$, $p_2(\mathbf{x}) := p(I(\mathbf{x})|\mathbf{x} \in \Omega_2)$ are the probability densities that model the intensity distributions in the two regions Ω_1, Ω_2 of the image. Minimization of the above GCV energy attempts to find a smooth curve $\mathcal{C}$ that separates the image domain into two regions Ω_1 (object) and Ω_2 (background) such that the likelihood of the observed image intensity values is maximized given the two region probability densities p_1, p_2 corresponding to regions Ω_1, Ω_2. The CV energy E^{CV} in Eq. 2.30 is a special case of the above energy and is obtained by choosing a Gaussian probability density $p_1(\mathbf{x}) = \frac{1}{\sqrt{2\pi}\sigma_1}\exp^{-\frac{(I(\mathbf{x})-\mu_1)^2}{2\sigma_1^2}}$, $p_2(\mathbf{x}) = \frac{1}{\sqrt{2\pi}\sigma_2}\exp^{-\frac{(I(\mathbf{x})-\mu_2)^2}{2\sigma_2^2}}$, with $\sigma_1 = \sigma_2 = \sqrt{0.5}$ to model the region intensity distributions. The Parzen density has also been

employed for image segmentation based on the GCV model [16]. The evolution corresponding to the above energy in Eq. 2.33 is given by:

$$\partial_t \Phi = \mathbf{f}^{\text{GCV}}_{\text{image}}[\Phi] + \gamma \mathbf{f}^{\text{Length}}_{\text{smooth}}[\Phi], \tag{2.34}$$
$$\text{with} \quad \mathbf{f}^{\text{GCV}}_{\text{image}}[\Phi] = (\log\, p_1 - \log\, p_2)|\nabla\Phi|,$$

where p_1,p_2 are re-estimated at every evolution step.

The non-parametric deformable models discussed until now formulate energies either purely based on edge cues (see Section 2.2.1) or purely based on the region information in the image. Contrary to these formulations, Paragios et *al.* [80] integrated the edge-based GAC model into the region-based GCV model and proposed the *geodesic active region* (GAR) model:

$$E^{\text{GAR}}[\Phi] = E^{\text{GCV}}_{\text{image}}[\Phi] + \gamma E^{\text{GAC}}_{\text{smooth}}[\Phi]. \tag{2.35}$$

The evolution corresponding to the GAR model is given by:

$$\partial_t \Phi = \mathbf{f}^{\text{GCV}}_{\text{image}}[\Phi] + \gamma \mathbf{f}^{\text{GAC}}_{\text{smooth}}[\Phi]. \tag{2.36}$$

Template-based curve representation: Saddi et *al.* [102] re-formulated the GCV energy in Eq. 2.33 by replacing the level set representation with the template-based representation of curve $\mathcal{C}$ (see Figure 2.4c) and proposed the following template-based generalized Chan-Vese (TGCV) energy:

$$E^{\text{TGCV}}[\mathbf{U}] = E^{\text{TGCV}}_{\text{image}}[\mathbf{U}] = \int_\Omega -I_T(\mathbf{x}+\mathbf{U}(\mathbf{x}))\log\, p_1 \ldots$$
$$\ldots - (1 - I_T(\mathbf{x}+\mathbf{U}(\mathbf{x})))\log\, p_2\, d\mathbf{x}, \tag{2.37}$$

where I_T was chosen as a binary template image. Comparing the above with Eq. 2.33, we see that the warped template $I_T(\mathbf{x}+\mathbf{U}(\mathbf{x}))$ can be seen as the Heaviside function $H(\Phi)$. The minimization of the above energy was performed using the fluid demons approach (see Section 2.1.1 and algorithm 1). In this approach, an update field $\mathbf{u}^k$ was computed at each evolution step k as:

$$\mathbf{u}^k = \mathbf{f}^{\text{TCGV}}_{\text{image}}[\mathbf{U}^k] = (\log\, p_1 - \log\, p_2)(\nabla I_T(\mathbf{x}+\mathbf{U}^k(\mathbf{x}))). \tag{2.38}$$

Then, this update field was smoothed at each step using a Gaussian kernel G_σ, i.e., $\mathbf{u}^k \leftarrow G_\sigma * \mathbf{u}^k$. As mentioned before (see Section 2.1.1), this can be regarded as using the diffusion regularizer E^{diff}_R (see Eq. 2.8) as the smoothness-based energy, i.e., $E^{\text{TCGV}}_{\text{smooth}} = E^{\text{diff}}_R$ and it follows that $F^{\text{TCGV}}_{\text{smooth}}[\mathbf{u}] = \mathcal{A}^{\text{diff}}[\mathbf{u}] = \triangle\mathbf{u}$. This smoothed update field was then used to update the current estimate of the deformation field $\mathbf{U}^k$ using a compositional update rule, i.e, $\mathbf{U}^{k+1} \leftarrow \mathbf{U}^k \circ \mathbf{u}^k$. A similar template-based segmentation method was recently proposed by Le Guyader et *al.* [65], where the level set based CV energy in Eq. 2.30 was re-formulated using the template-based curve representation and the nonlinear elastic regularizer in Eq. 2.6 as follows:

$$E^{\text{TCV}-\text{nlin}-\text{elas}}[\mathbf{U}] = E^{\text{TCV}}_{\text{image}}[\mathbf{U}] + \gamma E^{\text{nlin}-\text{elas}}_R[\mathbf{U}], \tag{2.39}$$
$$\text{with} \quad E^{\text{TCV}}_{\text{image}}[\mathbf{U}] = \int_\Omega H(I_T(\mathbf{x}+\mathbf{U}))(I-\mu_1)^2 + (1-H(I_T(\mathbf{x}+\mathbf{U})))(I-\mu_2)^2\, d\mathbf{x}.$$

where the template image I_T was chosen as a signed distance function. As mentioned previously in Section 2.1.1, the minimization of the above energy functional $E^{\mathrm{TCV-nlin-elas}}$ is performed using the variable splitting method [70].

2.2.2 Parametric deformable models

In parametric deformable models, the curve is represented explicitly through the use of either a local or a global parametrization. The curve can be locally parametrized simply by using the coordinates of the points on the curve as the parameters. An alternative way to locally parametrize the curve is to express the curve in terms of finite set of basis functions with a local support. In a similar manner, basis functions with a global support are employed to achieve a global parametrization of the curve. We discuss both the local and global parametrization based approaches below. In all the parametric deformable models discussed below, the explicit representation of the curve is employed with the exception of works by Huang et *al.* [55] and Li et *al.* [67] where a template-based representation of the curve is used.

Local parametrization

The easiest way to locally parametrize the curve $\mathcal{C}$ is by using a vector function $\mathbf{\Gamma} : [0\ 1] \rightarrow \mathbb{R}^2$, such that $\mathbf{\Gamma}(r) = (x(r), y(r)),\ r \in [0\ 1]$ are the coordinates of the points on the curve $\mathcal{C}$ (see Figure 2.4a). In the seminal work [60], Kass et *al.* employed this point coordinate parametrization of the curve and proposed the popular *snake* or *active contour* parametric deformable model:

$$
\begin{aligned}
E^{\mathrm{snake}}[\mathbf{\Gamma}] &= E^{\mathrm{snake}}_{\mathrm{image}}[\mathbf{\Gamma}] + E^{\mathrm{snake}}_{\mathrm{smooth}}[\mathbf{\Gamma}], \qquad (2.40)\\
\text{with} \quad E^{\mathrm{snake}}_{\mathrm{image}}[\mathbf{\Gamma}] &= \int_0^1 -|\nabla(G_\sigma * I)|^2\, ds,\\
E^{\mathrm{snake}}_{\mathrm{smooth}}[\mathbf{\Gamma}] &= \frac{1}{2}\int_0^1 w_1(r)|\partial_s \mathbf{\Gamma}|^2 + w_2(r)|\partial^2_{ss}\mathbf{\Gamma}|^2\, ds,
\end{aligned}
$$

where G_σ is a Gaussian kernel. In the above energy, the image-based energy $E^{\mathrm{snake}}_{\mathrm{image}}$ was defined using the *edge map* $-|\nabla(G_\sigma * I)|^2$ of the image and smoothness-based energy $E^{\mathrm{snake}}_{\mathrm{smooth}}$ consists of two terms, the *tension* and *rigidity* of the curve $\mathbf{\Gamma}$. The corresponding evolution for the snake energy is given by:

$$
\begin{aligned}
\partial_t \mathbf{\Gamma} &= \mathbf{f}^{\mathrm{snake}}_{\mathrm{image}}[\mathbf{\Gamma}] + \mathbf{f}^{\mathrm{snake}}_{\mathrm{smooth}}[\mathbf{\Gamma}], \qquad (2.41)\\
\text{with} \quad \mathbf{f}^{\mathrm{snake}}_{\mathrm{image}}[\mathbf{\Gamma}] &= \nabla(|\nabla(G_\sigma * I)|^2), \qquad \mathbf{f}^{\mathrm{snake}}_{\mathrm{smooth}}[\mathbf{\Gamma}] = \partial_s(w_1\partial_s\mathbf{\Gamma}) - \partial^2_{ss}(w_2\partial^2_{ss}\mathbf{\Gamma}).
\end{aligned}
$$

As the snake model is purely dependent on the edge map of the image, a limitation of the snake model is that, for the snake model to get attracted to the boundary of the object of interest, it has to be initialized near the object boundary. In order to increase the "range of attraction" of the snake model, Cohen et *al.* [29] added a new force to the original snake forces in Eq. 2.41, the *balloon*

force which moves the snake model in the normal direction, resulting in the following evolution:

$$\partial_t \mathbf{\Gamma} = \mathbf{f}_{\text{image}}^{\text{snake}}[\mathbf{\Gamma}] + \mathbf{f}_{\text{image}}^{\text{balloon}}[\mathbf{\Gamma}] + \mathbf{f}_{\text{smooth}}^{\text{snake}}[\mathbf{\Gamma}], \tag{2.42}$$
$$\text{with} \quad \mathbf{f}_{\text{image}}^{\text{balloon}}[\mathbf{\Gamma}] = w_{\text{balloon}}\mathbf{N}(\mathbf{\Gamma}).$$

where the magnitude of w_{balloon} controls the strength of the balloon force and sign of w_{balloon} determines the direction of the force along the normal $\mathbf{N}(\mathbf{\Gamma})$ to the curve. One of the drawbacks of the balloon forces is that the magnitude of w_{balloon} needs to be chosen carefully or else the balloon force might become too strong and move the snake model past the weak edges. Subsequently, Xu et *al.* [133] proposed the *gradient vector flow* (GVF) force which increases the attraction range of the snake model without the drawback entailed in the use of the balloon force. The basic idea behind the GVF force is to diffuse the gradient of the edge map to the regions away from the object boundary by solving the following diffusion PDE:

$$\partial_t \boldsymbol{v} = c\nabla^2 \boldsymbol{v} - |\nabla \mathbf{g}|^2(\boldsymbol{v} - \nabla \mathbf{g}), \tag{2.43}$$

where $\mathbf{g} = -|\nabla(G_\sigma * I)|^2$ is the edge map of the image and $\boldsymbol{v}$ is the desired smooth edge map. The GVF force is defined as $\mathbf{f}_{\text{image}}^{\text{GVF}}[\mathbf{\Gamma}] = \boldsymbol{v}^*$, where $\boldsymbol{v}^*$ is the steady state solution to the above PDE. The GVF evolution is then given by:

$$\partial_t \mathbf{\Gamma} = \mathbf{f}_{\text{image}}^{\text{snake}}[\mathbf{\Gamma}] + \mathbf{f}_{\text{image}}^{\text{GVF}}[\mathbf{\Gamma}] + \mathbf{f}_{\text{smooth}}^{\text{snake}}[\mathbf{\Gamma}]. \tag{2.44}$$

Recently, in an effort to incorporate region information into the snake model, Shen *et al.* [107] proposed the *active volume model* (AVM), by introducing an additional image-based energy term $E_{\text{image}}^{\text{AVM}}$ computed based on the region statistics into the snake energy in Eq. 2.40:

$$E^{\text{AVM}}[\mathbf{\Gamma}] = E_{\text{image}}^{\text{snake}}[\mathbf{\Gamma}] + E_{\text{image}}^{\text{AVM}}[\mathbf{\Gamma}] + E_{\text{smooth}}^{\text{snake}}[\mathbf{\Gamma}], \tag{2.45}$$
$$\text{with} \quad E_{\text{image}}^{\text{AVM}}[\mathbf{\Gamma}] = \int_0^1 \Phi_{\mathbf{\Gamma}}(\mathbf{\Gamma})\Phi_R(\mathbf{\Gamma})\, ds,$$

where $\Phi_{\mathbf{\Gamma}}$ the signed distance function corresponding to the current estimate of the segmentation boundary $\mathbf{\Gamma}$ and Φ_R is the signed distance function corresponding to the current prediction of the object region, the Region-of-Interest (ROI). The AVM evolution is given by:

$$\partial_t \mathbf{\Gamma} = \mathbf{f}_{\text{image}}^{\text{snake}}[\mathbf{\Gamma}] + \mathbf{f}_{\text{image}}^{\text{AVM}}[\mathbf{\Gamma}] + \mathbf{f}_{\text{smooth}}^{\text{snake}}[\mathbf{\Gamma}], \tag{2.46}$$
$$\text{with} \quad \mathbf{f}_{\text{image}}^{\text{AVM}}[\mathbf{\Gamma}] = -\nabla(\Phi_{\mathbf{\Gamma}}\Phi_R).$$

Segmentation using the AVM model proceeds by alternating the above evolution with the ROI prediction step until the true object boundary is reached. Given the current estimate of the segmentation boundary $\mathbf{\Gamma}$, the image domain Ω is partitioned into two disjoint regions, $\Omega_1 = \{\mathbf{x}|\Phi_{\mathbf{\Gamma}}(\mathbf{x}) \geq 0,\, \mathbf{x} \in \Omega\}$ corresponding to the object and $\Omega_2 = \{\mathbf{x}|\Phi_{\mathbf{\Gamma}}(\mathbf{x}) < 0,\, \mathbf{x} \in \Omega\}$ corresponding to the background. Then, the probability distributions p_1, p_2 corresponding to the object, background respectively are

estimated from the region intensity statistics. Now, the ROI is predicted as the largest connected region in the image where $p_1 \geq p_2$, i.e., the largest connected region which has the higher probability of belonging to the object than the background. A signed distance function Φ_R is computed on this ROI so that it can be used to evolve the segmentation boundary according to the above AVM evolution equation.

As an alternative to the above discussed *continuous* parametrization of the curve $\mathcal{C}$ using the coordinates of the points, $\mathbf{\Gamma}(r) = (x(r), y(r)),\ r \in [0\ 1]$, a *discrete* parametrization of the curve $\mathcal{C}$ using a finite set of basis functions can be defined as:

$$\mathbf{\Gamma}(r) = \sum_{n=1}^{N} \boldsymbol{\alpha}_n B_n(r), \quad r \in [0\ 1], \tag{2.47}$$

where the basis function coefficients $\boldsymbol{\alpha} = [\boldsymbol{\alpha}_n]_{n=1}^{N}$ are the parameters representing the curve $\mathcal{C}$. Using this discrete parametrization of the curve $\mathcal{C}$, the snake evolution in Eq. 2.41 can be written as:

$$\partial_t \boldsymbol{\alpha} = S_{\text{stiff}}^{\text{snake}} \boldsymbol{\alpha} - \mathbf{f}_{\text{image}}^{\text{snake}}, \tag{2.48}$$

where $S_{\text{stiff}}^{\text{snake}}$ is the *stiffness* matrix which is related to the smoothness force $\mathbf{f}_{\text{smooth}}^{\text{snake}}$ and $\mathbf{f}_{\text{image}}^{\text{snake}}$ is a vector of the image forces corresponding to $\mathbf{f}_{\text{image}}^{\text{snake}}$. This discrete parametrization based snake model has been employed for image segmentation using basis functions with local support, such as FEM basis functions B^{FEM} [30],[39], B-spline basis functions $B^{\text{B-spline}}$ [68] (see Section (2.1.2) for the definition of the FEM and B-spline basis functions). Shen et *al.* [106] also employed the FEM basis functions into the AVM model (see Eq. 2.46) resulting in the evolution:

$$\partial_t \boldsymbol{\alpha} = S_{\text{stiff}}^{\text{snake}} \boldsymbol{\alpha} - \mathbf{f}_{\text{image}}^{\text{snake}} - \mathbf{f}_{\text{image}}^{\text{AVM}}, \tag{2.49}$$

where $\mathbf{f}_{\text{image}}^{\text{AVM}}$ is the vector of region-based forces corresponding to $\mathbf{f}_{\text{image}}^{\text{AVM}}$. We emphasize that the parametrization of the AVM model using FEM basis functions still corresponds to an explicit representation of the curve (see Figure 2.4a) and not to a template-based representation of the curve (see Figure 2.4c) as employed by Huang et *al.* [55] (discussed below), where the deformation field is parametrized using a set of local basis functions.

Template-based curve representation: Huang et *al.* [55] proposed a parametric deformable model called the *metamorphs* using the template-based representation of the curve $\mathcal{C}$ (see Figure 2.4c). The metamorphs energy contains both edge-based and region-based image terms and is given by:

$$E^{\text{metamorphs}}[\varphi^{-1}] = E_{\text{image}}^{\text{metamorphs}}[\varphi^{-1}], \tag{2.50}$$

$$\text{with} \quad E_{\text{image}}^{\text{metamorphs}}[\varphi^{-1}] = \int_{\Omega_1} (I_T(\mathbf{x}) - \Phi(\varphi^{-1}(\mathbf{x})))^2\, d\mathbf{x} + \int_{\partial\Omega_1} \Phi(\varphi^{-1}(\mathbf{x}))^2\, d\mathbf{x} \ldots$$

$$\ldots + \int_{\Omega_1} (I_T(\mathbf{x}) - \Phi_R(\varphi^{-1}(\mathbf{x})))^2\, d\mathbf{x} - \int_{\partial\Omega_1} \log p_1\, d\mathbf{x},$$

where I_T is the template chosen as a signed distance function, $\Omega_1 = \{\mathbf{x}|I_T(\mathbf{x}) \geq 0, \mathbf{x} \in \Omega\}$ is the region corresponding to the object and p_1 is the probability modeling the region statistics in region Ω_1, Φ is the un-signed distance function corresponding to the edge map of the image I, Φ_R is the signed distance function corresponding to the Region-of-Interest (ROI), where the ROI is computed as the largest connected region that has the probability p_1 of being an object greater than a certain threshold. In the above, the first two terms of the image-based energy terms $E_{\text{image}}^{\text{metamorphs}}$ are dependent on the edge information in the image and the last two terms are derived from region statistics. The minimization of the above energy is performed using B-spline based free form deformation (FFD) deformable registration approach (see Section 2.1.2) where the transformation φ^{-1} is expressed using a set of FFD basis functions B^{FFD}. We observe that the smoothness-based energy term was not incorporated in the above energy $E^{\text{metamorphs}}$, this is because the regularization through the FFD parametrization was sufficient to guarantee a smooth transformation. On the other hand, Li et *al.* [67] used the bending regularizer E_R^{bending} in Eq. 2.17 as the smoothness-based energy term and incorporated the FFD deformation model into the region-based GCV energy in Eq. 2.33 and proposed the following "active image" (AI) deformable model for template-based segmentation:

$$\begin{aligned} E^{\text{AI}}[\varphi] &= E_{\text{image}}^{\text{AI}}[\varphi] + E_R^{\text{bending}}[\varphi], \\ \text{with} \quad E_{\text{image}}^{\text{AI}}[\varphi] &= \int_\Omega -I_T(\varphi(x)) \log\, p_1 - (1 - I_T(\varphi(x))) \log\, p_2 \, d\mathbf{x}. \end{aligned} \tag{2.51}$$

where I_T is chosen as a binary template image.

Global parametrization

Typically, most of the segmentation methods based on parametric deformable models employ a local parametrization of the curve $\mathcal{C}$ (as discussed in the previous section) because, they do not incorporate global properties of the curve like size, orientation into the segmentation process. However, there exist a few parametric deformable models that take into account the global shape properties of the curve for segmentation, and hence find the global parametrization of the curve useful.

The *Fourier snake* model proposed by Székely *et al.* [114] exemplifies the idea of employing a global parametrization of the curve $\mathcal{C}$ for image segmentation using parametric deformable models. In this work, the curve $\mathcal{C}$ is parametrized following Eq. 2.47 with a set of Fourier basis functions $B^{\text{Fourier}} := \{1, \cos(2\pi nr), \sin(2\pi nr)\}_{n=1}^{N}$ which have a global support. The curve $\mathcal{C}$ can be conveniently expressed using the Fourier representation as:

$$\mathbf{\Gamma}(r) = \begin{bmatrix} x(r) \\ y(r) \end{bmatrix} = \begin{bmatrix} a_0 \\ b_0 \end{bmatrix} + \sum_{n=1}^{N} \begin{bmatrix} a_n & b_n \\ c_n & d_n \end{bmatrix} \begin{bmatrix} \cos(2\pi nr) \\ \sin(2\pi nr) \end{bmatrix}, \quad r \in [0\ 1], \tag{2.52}$$

where $\boldsymbol{\alpha} = [a_0 \ldots a_N\, b_0 \ldots b_N\, c_0 \ldots c_N\, d_0 \ldots d_N]$ are the parameters describing the curve $\mathcal{C}$. In particular, the parameters a_0, c_0 define the global translation of the curve. Further, each term in the Fourier representation corresponds to the parametric representation of an ellipse and thus roughly

the global size and orientation of the curve $\mathcal{C}$ is defined by the linear combination of the sizes and orientations of the individual ellipses. Using the Fourier representation of the curve $\mathcal{C}$ in conjunction with the snake model in Eq. 2.40 yields an evolution of the form given in Eq. 2.48, through which image segmentation can be performed. Other basis functions with a global support like the spherical harmonics (SH) [61],[11] and spherical wavelets (SW) [77] have also been proposed for image segmentation.

2.3 Coupled registration and segmentation

Although *prima facie* image registration and segmentation might appear unrelated to each other, both of these image processing tasks are in fact complementary to one another. The registration of two images can be guided through the improved segmentation of the corresponding common objects of interest in those images and in turn segmentation of an object of interest in a given image can be guided by mapping the segmentation boundary of the corresponding common object of interest in another image into the given image through registration. In the previous sections, we have only discussed deformable energy minimization approaches that deal with registration and segmentation in isolation from each other. However, there also have been research efforts directed towards developing methods that can jointly achieve the goals of registration and segmentation. These methods take advantage of the aforementioned interdependence between registration and segmentation through a *coupled* energy minimization framework where the registration and segmentation energies are unified or coupled into a single energy functional, which is then minimized to achieve the objective of joint registration and segmentation. More formally, given two images $I : \Omega \rightarrow \mathbb{R}$, $I^{'} : \Omega^{'} \rightarrow \mathbb{R}$ with a corresponding common object of interest, let $\mathcal{C}, \mathcal{C}^{'}$ be two closed curves defined on Ω and $\Omega^{'}$ respectively and let $\varphi : \Omega \rightarrow \Omega^{'}$ be a transformation between the two images, such that $\mathcal{C}^{'} = \varphi(\mathcal{C})$, *i.e.*, the curve $\mathcal{C}^{'}$ is obtained by mapping the curve $\mathcal{C}$ into the image domain $\Omega^{'}$ using the transformation φ. Then, the goal of coupled registration and segmentation is to find the optimal curves $\mathcal{C}^{*}$, $\mathcal{C}^{'*}$ that define the segmentation boundary of the corresponding common object of interest in the images I, $I^{'}$ respectively while simultaneously estimating the transformation φ^{*} that registers the image $I^{'}$ with the image I. This is achieved through the minimization of an energy that is formulated by coupling the registration and segmentation energies using the relation $\mathcal{C}^{'} = \varphi(\mathcal{C})$:

$$
\begin{aligned}
&E[\varphi, \mathcal{C}, \mathcal{C}^{'}; I, I^{'}] = E[\varphi, \mathcal{C}, \varphi(\mathcal{C}); I, I^{'}], \\
&\varphi^{*}, \mathcal{C}^{*} = \underset{\varphi, \mathcal{C}}{\operatorname{argmin}}\ E[\varphi, \mathcal{C}, \varphi(\mathcal{C}); I, I^{'}].
\end{aligned} \tag{2.53}
$$

In the above, we note that the segmentation boundary $\mathcal{C}^{'*}$ in the image $I^{'}$ is obtained as $\mathcal{C}^{'*} = \varphi^{*}(\mathcal{C}^{*})$, *i.e.*, mapping the segmentation boundary $\mathcal{C}^{*}$ in the image I using the registration transformation φ^{*} into the image $I^{'}$.

The earliest work on coupled registration and segmentation is by Yezzi et *al.* [136], who coupled the region-based Chan-Vese (CV) segmentation energy functional E^{CV} with a *rigid* transformation

$\varphi^{\text{rigid}}(\mathbf{x}) = R\mathbf{x} + \mathbf{t}, \forall \mathbf{x} \in \Omega$, where R is the rotation matrix, $\mathbf{t}$ is the translational vector and proposed the following coupled energy functional:

$$E^{\text{CV}-\text{rigid}}[R, \mathbf{t}, \Phi] = E^{\text{CV}}_{\text{image}}[\Phi] + E^{\text{CV}}_{\text{image}}[\Phi^{'}] + E^{\text{Length}}_{\text{smooth}}[\Phi], \tag{2.54}$$

where $\Phi : \Omega \rightarrow \mathbb{R}$, $\Phi^{'} : \Omega^{'} \rightarrow \mathbb{R}$ are the level sets representing the curves $\mathcal{C}$, $\mathcal{C}^{'}$ respectively such that $\Phi(\mathbf{x}) = \Phi^{'}(\varphi^{\text{rigid}}(\mathbf{x})) = \Phi^{'}(R\mathbf{x} + \mathbf{t}), \forall \mathbf{x} \in \Omega$. Unal et *al.* [119] extended the above to the non-rigid registration case by adding a diffusion regularizer E^{diff}_{R}:

$$E^{\text{CV}-\text{diff}}[\mathbf{U}, \Phi] = E^{\text{CV}}_{\text{image}}[\Phi] + E^{\text{CV}}_{\text{image}}[\Phi^{'}] + E^{\text{Length}}_{\text{smooth}}[\Phi] + \gamma E^{\text{diff}}_{R}[\mathbf{U}], \tag{2.55}$$

where $\mathbf{U} : \Omega \rightarrow \Omega^{'}$ is the deformation field corresponding to the transformation φ, such that $\varphi(\mathbf{x}) = \mathbf{x} + \mathbf{U}(\mathbf{x})$ and $\Phi(\mathbf{x}) = \Phi^{'}(\varphi(\mathbf{x})) = \Phi^{'}(\mathbf{x} + \mathbf{U}(\mathbf{x}))$, $\forall \mathbf{x} \in \Omega$. Instead of the Chan-Vese energy E^{CV}, Lord et *al.* [69] coupled the more general Mumford-Shah (MS) functional E^{MS} with the Sum of Squared Differences (SSD) data term E^{SSD}_{D} and the bending energy regularization term E^{bending}_{R}, to perform joint non-rigid registration and region-based segmentation:

$$\begin{aligned} E^{\text{MS}-\text{SSD}}[\varphi, \mathcal{C}, \tilde{I}, \tilde{I}^{'}] = E^{\text{MS}}_{\text{image}}[\mathcal{C}, \tilde{I}] + E^{\text{MS}}_{\text{image}}[\mathcal{C}^{'}, \tilde{I}^{'}] \ldots \\ \ldots + E^{\text{SSD}}_{D}[\varphi, \tilde{I}, \tilde{I}^{'}] + E^{\text{bending}}_{R}[\varphi]. \end{aligned} \tag{2.56}$$

They minimized the above energy using the level set representation Φ, $\Phi^{'}$ of the curves $\mathcal{C}$, $\mathcal{C}^{'}$ respectively such that $\Phi(\mathbf{x}) = \Phi^{'}(\varphi(\mathbf{x}))$, $\forall \mathbf{x} \in \Omega$, and the transformation φ was parametrized using the thin-plate spline (TPS) basis functions $B^{\text{RBF-TPS}}_{n}(r) = r^2 \log r$. The TPS parametrization of the transformation was also employed by Bertelli et *al.* [14], but along with the *pairwise similarity* (PS) image-based energy term $E^{\text{PS}}_{\text{image}}$ to jointly register and segment images taken from two different views of the same scene:

$$E^{\text{PS}-\text{TPS}}[\varphi, \Phi] = E^{\text{PS}}_{\text{image}}[\varphi, \Phi; I, I^{'}], \tag{2.57}$$

$$\begin{aligned} \text{where} \quad E^{\text{PS}}_{\text{image}}[\varphi, \Phi; I, I^{'}] = \int_{\Omega}\int_{\Omega^{'}} |I(\mathbf{x}) - I^{'}(\hat{\mathbf{x}})| H(\Phi) H(\Phi^{'})\, d\mathbf{x} d\hat{\mathbf{x}} \ldots \\ \ldots + \int_{\Omega}\int_{\Omega^{'}} |I(\mathbf{x}) - I^{'}(\hat{\mathbf{x}})| (1 - H(\Phi))(1 - H(\Phi^{'}))\, d\mathbf{x} d\hat{\mathbf{x}}. \end{aligned} \tag{2.58}$$

We can see that the pairwise similarity term $E^{\text{PS}}_{\text{image}}$ essentially measures the similarity between a given pixel in the object (background) region of image I with every pixel corresponding to the object (background) region in image $I^{'}$.

The coupled registration and segmentation methodology is particularly useful for solving the *atlas-based* segmentation task commonly encountered in medical image analysis. In atlas-based segmentation, the goal is to find the segmentation boundary $\mathcal{C}^{*}$ of an object of interest in the image I using the *atlas* image $I_A : \Omega_A \rightarrow \mathbb{R}$ which is already segmented, *i.e.*, the segmentation boundary $\mathcal{C}^{*}_{A}$ of the corresponding object of interest in I_A is known (see Figure 2.5). By choosing $I^{'} \equiv I_A$, Wang et *al.* [126] proposed the following energy for atlas-based segmentation using the coupled

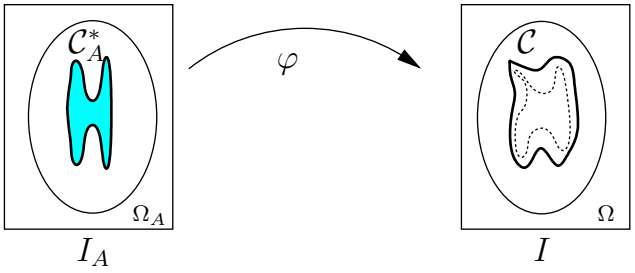

Figure 2.5: Illustration of atlas-based segmentation. The known boundary ($\mathcal{C}^*$) of the object of interest (shaded) in the atlas image I_A is mapped (using φ) into the image I to obtain the evolving segmentation boundary $\mathcal{C}$.

registration and segmentation methodology:

$$E^{\text{CV}-\text{CCRE}}[\mathbf{U}, \Phi] = E^{\text{CV}}_{\text{image}}[\Phi] + E^{\text{CCRE}}_{D}[\mathbf{U}; I, I_A] + E^{\text{atlas}}_{\text{couple}}[\Phi, \mathbf{U}; \Phi^*_A] + \gamma E^{\text{diff}}_{R}[\mathbf{U}], \quad (2.59)$$
$$\text{where} \quad E^{\text{atlas}}_{\text{couple}}[\Phi, \mathbf{U}; \Phi^*_A] = \text{dist}(\Phi(\mathbf{x}), \Phi^*_A(\mathbf{x} + \mathbf{U}(\mathbf{x}))).$$

where $\Phi^*_A : \Omega_A \rightarrow \mathbb{R}$ is the level set corresponding to the segmentation boundary $\mathcal{C}^*_A$. In the above energy, the CV energy E^{CV} has been coupled with the cross cumulative residual entropy (CCRE) data term E^{MI}_D using a special "coupling" term $E^{\text{atlas}}_{\text{couple}}$, that measures the distance between the evolving segmentation boundary Φ in image I and the warped atlas segmentation boundary $\Phi^*_A(\mathbf{x} + \mathbf{U}(\mathbf{x}))$. In [98], Rousson et *al.* proposed an atlas-based segmentation method for the sequential segmentation of the multiple anatomical structures. Here, they employed a *spatial or probabilistic atlas* $I^{\text{spatial}}_A : \Omega^{\text{spatial}}_A \rightarrow [0\ 1]$, which encodes the probabilities $p_{\mathcal{S}}(\mathbf{x})$, $p_{\bar{\mathcal{S}}}(\mathbf{x})$ of a pixel $\mathbf{x}$ belonging to the inside or outside of an anatomical structure $\mathcal{S}$ respectively. The basic idea of their segmentation methodology was to introduce an additional image-based energy term $E^{\text{GCV}-\text{spatial}}_{\text{image}}$ based on the spatial atlas into the region-based generalized Chan-Vese (GCV) segmentation framework (see Eq. 2.33) as follows:

$$E^{\text{GCV}-\text{spatial}}[\Phi] = E^{\text{GCV}}_{\text{image}}[\Phi] + E^{\text{GCV-spatial}}_{\text{image}}[\Phi] + \gamma E^{\text{Length}}_{\text{smooth}}[\Phi], \quad (2.60)$$
$$\text{with} \quad E^{\text{GCV-spatial}}_{\text{image}}[\Phi] = \int_{\Omega} -H(\Phi) \log p_{\mathcal{S}}(\mathbf{U}(\mathbf{x})) - (1 - H(\Phi)) \log p_{\bar{\mathcal{S}}}(\mathbf{U}(\mathbf{x}))\, d\mathbf{x}.$$

Here, the probabilities $p_{\mathcal{S}}(\mathbf{U}(\mathbf{x}))$, $p_{\bar{\mathcal{S}}}(\mathbf{U}(\mathbf{x}))$ are determined by mapping the probabilities defined in the spatial atlas domain $\Omega^{\text{spatial}}_A$ into the image domain Ω using the deformation field $\mathbf{U}$. The above segmentation methodology was then employed iteratively for the segmentation of multiple structures $\{\mathcal{S}_n\}_{n=1}^N$ in a sequential manner. At each iteration, the deformation field $\mathbf{U}$ was obtained through the registration of the spatial atlas I^{spatial}_A with the image I based on only those structures that are segmented in the image I. Pohl et *al.* [83] employed the spatial I^{spatial}_A atlas with intensity priors for the segmentation of anatomical structures using the Expectation-Maximization (EM) algorithm.

Deformable registration methods		Deformable models in segmentation	
Non-parametric	Parametric	Non-parametric	Parametric
Variational [15],[25], [72],[41] Demons [117],[81],[19], [112],[121],[122]	Radial basis [90], [94] B-spline [101],[99], [91],[50],[110] FEM [40],[89],[56] DFT [4],[26] DCT [9] **Proposed FEM diffusion-based in Section 4.2** [84]	Level set (Implicit): Edge-based [20],[21] Region-based: [23],[79],[80],[16] Template-based: TGCV [102], TCV [65]	Explicit: Snakes [60] Balloon [29] GVF [133] AVM [107] FEM snakes [30],[39] B-spline snakes [68] AVM-FEM [106] Fourier [114], SH [61], [11], SW [77] snakes Template-based: Metamorphs [55] Active-image [67] **Proposed FEM region-based diffusion-based in Section 4.3**

Table 2.2: Summary of the various deformable registration methods and the segmentation methods using deformable models updated with the FEM-based continuous registration and segmentation methods proposed in this thesis.

2.4 Discussion

The above review provides us with a context for placing the various algorithms proposed in the rest of this thesis among the existing works on deformable registration and segmentation using deformable models (see Table 2.2). In general, the proposed registration and segmentation algorithms belong to the group of parametric approaches (see Sections 2.1.2 and 2.2.2). Further, the proposed segmentation algorithms use the template-based curve representation (see Figure 2.4) similar to [55], [102], [67], [65]. More importantly, the proposed registration and segmentation methods extensively use the finite element method (FEM) as opposed to the finite difference method (FDM) which is used in the implementation of all the registration and segmentation methods discussed above, with exception of [40], [56], [89], [30], [39], [106]. The advantage in using the FEM method is that it allows for the use of non-uniform meshes leading to very computationally efficient registration and segmentation algorithms.

The existing FEM-based registration methods [40], [56], [89] employ complex bio-mechanical regularization terms which restrict their applicability to specific medical image registration tasks. But, the proposed FEM-based registration method uses the more general diffusion-based regularizer and thus can address a wider range of image registration tasks. The current works on FEM-based segmentation [30], [39], [106] use the explicit snakes-like curve representation as opposed to the template-based curve representation used in the proposed FEM-based segmentation method. Whereas, the popular template-based segmentation approaches [55], [102], [67], [65] use the FDM method along with a uniform mesh in contrast to the more computationally efficient non-uniform

mesh based implementation of the proposed FEM-based template-based segmentation method.

As a last note, it is important to understand that, in this thesis image registration and segmentation are treated as two separate tasks, even though a unified approach is developed to solve the energy minimization formulations that correspond to image registration and segmentation. Therefore, the proposed unified FEM-based registration and segmentation methodology should not be confused with the coupled registration and segmentation approach in Section 2.3.

Chapter 3

Introduction to the finite element method (FEM)

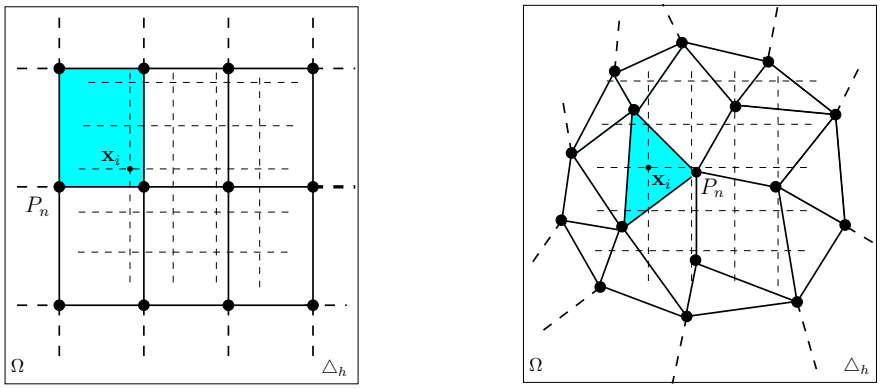

Uniform mesh Non-uniform mesh

Figure 3.1: A schematic of uniform and non-uniform meshes on the rectangular 2D domain is shown here. A sample node P_n, sample point $\mathbf{x}_i$ of the Cartesian grid overlapping the rectangular and triangular elements (shaded) of the uniform and non-uniform meshes respectively are highlighted. Note that, in image registration and segmentation formulations $\mathbf{x}_i$ corresponds to the image (pixel) co-ordinates.

The finite element method (FEM) is a powerful alternative to the finite difference method (FDM) for computing the numerical solution of partial differential equations (PDEs). While the FDM method is restricted only to use a uniform discretization of the problem domain, the FEM method can facilitate the use of both uniform and non-uniform meshes. The main advantage of using a non-uniform mesh is that, the mesh resolution can be chosen based on the desired accuracy of the solution in the various regions of the problem domain. In this chapter, we discuss some of the important aspects related to the FEM method.

3.1 Preliminaries

In the FEM method, the first step is to divide the problem domain $\Omega \subset \mathbb{R}^{\nu}$ [†] into a set of subdomains or *finite elements* denoted by a uniform or a non-uniform mesh $\mathcal{M} = (\{P_n\}_{n=1}^{N}, \triangle_h)$ (see Figure 3.1), where $\triangle_h$ is a set of elements (triangles or rectangles in 2D and tetrahedra or cuboids in 3D) and $\{P_n\}_{n=1}^{N}$ is a set of points called the *nodes*. Then, the unknown solution $u : \Omega \rightarrow \mathbb{R}$ of the PDE is approximated by the linear combination of a set of *nodal basis* functions $\{\phi_n\}_{n=1}^{N}$ with a compact support defined on the mesh $\mathcal{M}$ as follows:

$$u(\mathbf{x}) \approx \pi_h u(\mathbf{x}) = \sum_{n=1}^{N} u_n \phi_n(\mathbf{x}; \mathcal{M}), \qquad \mathbf{x} \in \Omega. \tag{3.1}$$

The different possible choices for the nodal basis functions are discussed in Section 3.3. Henceforth, the approximation of the unknown solution u using the nodal basis $\{\phi_n\}_{n=1}^{N}$ is referred to as the finite element approximation. The finite element approximation essentially reduces the problem of solving the PDE to finding the unknown nodal parameters $\{u_n\}_{n=1}^{N}$, $u_n \in \mathbb{R}$.

3.2 Solving the reaction-diffusion PDE

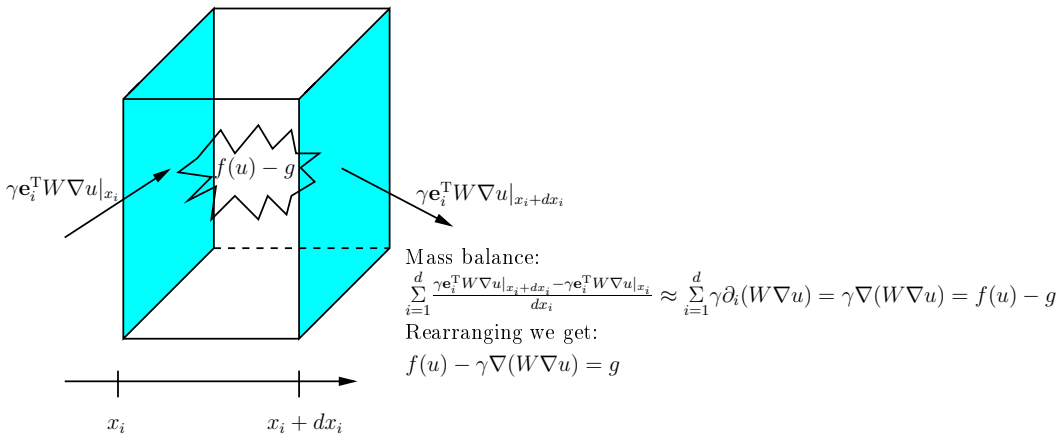

Figure 3.2: Illustration of the steady state mass-balance corresponding to the reaction-diffusion process across a small element in problem domain Ω.

We discuss the use of the FEM method for solving the following *reaction-diffusion* PDE (which is a non-linear elliptic PDE), that is extensively encountered in our proposed work on image registration and segmentation:

$$\begin{aligned} f(u) - \gamma \nabla (W \nabla u) &= g, \qquad \mathbf{x} \in \Omega, \\ (W \nabla u)^{\mathrm{T}} \mathbf{n} &= 0, \qquad \mathbf{x} \in \partial\Omega, \end{aligned} \tag{3.2}$$

where $f : \Omega \rightarrow \mathbb{R}$, $g : \Omega \rightarrow \mathbb{R}$, $\mathbf{n}$ is the outer normal vector to the boundary $\partial\Omega$ and γ is a constant. The reaction-diffusion PDE basically corresponds to the steady state mass balance in a

[†] $\nu = 2$ for 2D domain and $\nu = 3$ for 3D domain

reaction-diffusion process (see Figure 3.2), where the term $f(u)$ denotes the reaction process and $g \equiv g(\mathbf{x})$ is the spatially varying generation term independent of u. Further, the term $\gamma\nabla(W\nabla u)$ denotes the diffusion process, where the *diffusivity* or *stiffness field* $W \equiv W(\mathbf{x})$ in general varies over the domain Ω. It is a scalar in the case of *isotropic* diffusion, and a symmetric $\nu \times \nu$ matrix in the case of *anisotropic* diffusion. We present two different formulations of the FEM method, namely the *Galerkin* FEM method and the *Ritz* FEM method.

3.2.1 Galerkin FEM method

In the Galerkin FEM method, the first step is to derive the *weak form* of the PDE in Eq. 3.2 by multiplying a "test" function v to both sides of the PDE and integrating by parts as below:

$$\begin{aligned}
&\int_\Omega f(u)v\,d\mathbf{x} - \gamma\int_\Omega \nabla(W\nabla u)v\,d\mathbf{x} = \int_\Omega gv\,d\mathbf{x},\\
\Leftrightarrow &\int_\Omega f(u)v\,d\mathbf{x} + \gamma\int_\Omega (W\nabla u)^{\mathrm{T}}\nabla v\,d\mathbf{x} - \gamma\int_{\partial\Omega}(W\nabla u)^{\mathrm{T}}\mathbf{n}\,v\,ds = \int_\Omega gv\,d\mathbf{x},\\
\Leftrightarrow &\int_\Omega f(u)v\,d\mathbf{x} + \gamma\int_\Omega (W\nabla u)^{\mathrm{T}}\nabla v\,d\mathbf{x} = \int_\Omega gv\,d\mathbf{x} \qquad (\text{as}\int_{\partial\Omega}(W\nabla u)^{\mathrm{T}}\mathbf{n} = 0).
\end{aligned} \tag{3.3}$$

The problem of solving the PDE in Eq. 3.2 is equivalent to finding the unknown u that satisfies the above weak form for any test function v. Substituting the finite element approximation (see Eq. 3.1) into the above weak form and choosing the "test" function v as each one of the nodal basis functions $\{\phi_n\}_{n=1}^N$, we obtain the following set of N non-linear equations to be solved for the unknown nodal parameters $\{u_n\}_{n=1}^N$:

$$\int_\Omega f(\{u_n\}_{n=1}^N)\phi_n\,d\mathbf{x} + \gamma\sum_{m=1}^N u_m\int_\Omega (W\nabla\phi_m)^{\mathrm{T}}\nabla\phi_n\,d\mathbf{x} = \int_\Omega g\phi_n\,d\mathbf{x}, \qquad n \in \{1,2,\ldots,N\}. \tag{3.4}$$

3.2.2 Ritz FEM method

The Ritz FEM method proceeds by first transforming the problem of solving the PDE in Eq. 3.2 into a *variational energy minimization* problem as below:

$$u^* = \underset{u}{\operatorname{argmin}}\, E[u], \tag{3.5}$$

where:

$$E[u] = \int_\Omega F(u)\,d\mathbf{x} + \frac{\gamma}{2}\int_\Omega \nabla u^{\mathrm{T}}W\nabla u\,d\mathbf{x} - \int_\Omega gu\,d\mathbf{x} \qquad \text{with} \quad F'(u) = f(u).$$

We can observe that the PDE in Eq. 3.2 is in fact the Euler-Lagrange equation of the above energy functional E, which is obtained by setting the variational derivative of the energy E to zero, i.e., $\nabla_u E = f(u) - \gamma\nabla(W\nabla u) - g = 0 \equiv f(u) - \gamma\nabla(W\nabla u) = g$, where ∇_u denotes the variational derivative with respect to u. Thus, solving the PDE in Eq. 3.2 is equivalent to the minimization of the energy functional E in Eq. 3.5. Now, incorporating the finite element approximation of u

(see Eq. 3.1) into the energy functional E, we obtain a finite-dimensional approximation to the variational energy minimization problem as:

$$\{u_n^*\}_{n=1}^N = \underset{\{u_n\}_{n=1}^N}{\operatorname{argmin}} E(\{u_n\}_{n=1}^N), \tag{3.6}$$

where:

$$E(\{u_n\}_{n=1}^N) = \int_\Omega F(\{u_n\}_{n=1}^N)\, d\mathbf{x} + \frac{\gamma}{2}\sum_{n=1}^N u_n \sum_{m=1}^N u_m \int_\Omega (W\nabla\phi_n)^{\mathrm{T}}\nabla\phi_m\, d\mathbf{x} - \sum_{n=1}^N u_n \int_\Omega g\phi_n\, d\mathbf{x},$$
$$\text{with} \quad \partial_{u_n} F(\{u_n\}_{n=1}^N) = f(\{u_n\}_{n=1}^N)\phi_n \quad n \in \{1, 2, \ldots, N\}.$$

Thus, the problem of solving the PDE in Eq. 3.2 is transformed into to the multivariate minimization of the energy in Eq. 3.6 with respect to the nodal parameters $\{u_n\}_{n=1}^N$. In order to perform the minimization, we the set partial derivatives of the energy E with respect to each of the nodal parameters $\{u_n\}_{n=1}^N$ to zero, i.e., $\partial_{u_n} E = 0 \quad n \in \{1, 2, \ldots, N\}$. This results in exactly the same set of N non-linear equations as in Eq. 3.4, that are needed to be solved for the unknown nodal parameters $\{u_n\}_{n=1}^N$.

From the above discussion, it can be seen that the Galerkin and Ritz FEM methods are essentially equivalent and in fact yield the same set of non-linear equations corresponding to the PDE in Eq. 3.2 [†]. However, it can also be seen that it is more natural to use the Galerkin FEM method when the problem is posed as a PDE whereas in problems that are inherently posed using the variational energy minimization formulation, the use of the Ritz FEM method becomes obvious. In our proposed work on registration and segmentation, we encounter both PDEs and variational energy minimization formulations, therefore in our work we use both the Galerkin and Ritz FEM methods depending on how the problem is posed. Further, we note that the Ritz FEM method was previously referred to as parametrization using the FEM basis functions in Section 2.1.2 and Section 2.2.2, in the context of parametric deformable registration (see Section 2.1.2) and segmentation using parametric deformable models (see Section 2.2.2) respectively.

3.3 Nodal basis functions

In this section, we present three types of nodal basis functions that can be used in the FEM method.

3.3.1 Lagrange basis

The Lagrange nodal basis functions, also known as *hat* or *tent* functions due their shape (see Figure 3.3) are the most commonly used basis functions in FEM-based solution schemes. The main attraction of the Lagrange basis is that it is naturally suited for non-uniform meshes and thus lends itself to the flexibility of the FEM method. The Lagrange basis functions are given by piece-wise linear

[†] When the same nodal basis functions $\{\phi_n\}_{n=1}^N$ are used for approximating u and also choosing the "test" functions v in the Galerkin FEM method.

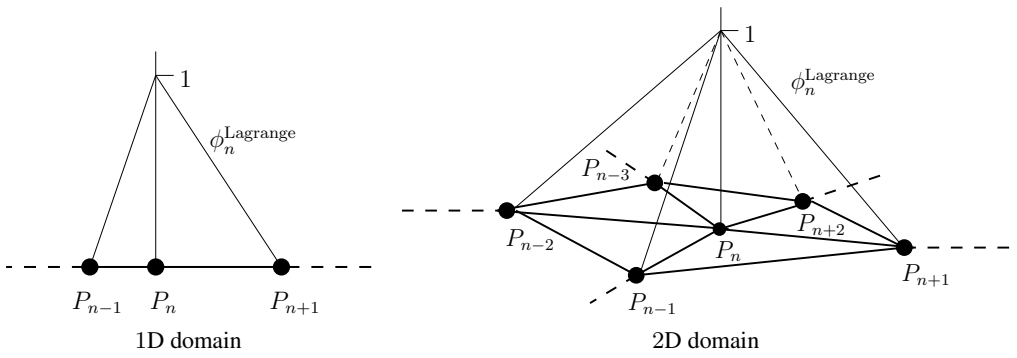

Figure 3.3: Illustration of the Lagrange nodal basis function.

polynomials that can be defined on both non-uniform and uniform meshes as [88]:

$$\phi_n^{\text{Lagrange}}(\mathbf{x}) = \begin{cases} & \text{is linear within each adjacent element,} \\ 1 & \text{at each node } P_n, \\ 0 & \text{at every other node } P_m \neq P_n. \end{cases} \tag{3.7}$$

Interestingly, when the Lagrange basis are used for the finite element approximation of u (see Eq. 3.1), the unknown nodal parameters $\{u_n\}_{n=1}^N$ actually correspond to the value of the solution of the PDE at the nodes $\{P_n\}_{n=1}^N$ respectively. This can be shown based on the definition of Lagrange basis in Eq. 3.7 as follows, for each $n \in \{1, 2, \ldots, N\}$:

$$u(P_n) = \sum_{n=1}^{N} u_n \phi_n^{\text{Lagrange}}(P_n) = u_n \phi_n^{\text{Lagrange}}(P_n) + \sum_{m \neq n} u_m \phi_m^{\text{Lagrange}}(P_m) = u_n. \tag{3.8}$$
$$\text{(as} \quad \phi_n^{\text{Lagrange}}(P_n) = 1 \quad \text{and} \quad \phi_m^{\text{Lagrange}}(P_m) = 0)$$

3.3.2 B-spline basis

The B-spline basis functions have been originally employed for data fitting and geometric modeling applications. However, Höllig [52] extensively studied the use of B-splines as the nodal basis functions in the FEM method. Consider a uniform mesh $N = N_x \times N_y \times N_z$ overlaid on the domain Ω, with a spacing $h_x \times h_y \times h_z$. The B-spline basis is then defined by a tensor-product of a set of cubic B-spline polynomials $\{b_0, b_1, b_2, b_3\}$ as follows :

$$\phi_n^{\text{B-spline}}(\mathbf{x}) = \prod_r \phi_{n_r}^{\text{B-spline}}(r), \qquad r \in \{x, y, z\}, \tag{3.9}$$

where:

$$\phi_{n_r}^{\text{B-spline}}(r) = \begin{cases} b_0(\frac{r}{h_r} - (n_r - 2)) & (n_r - 2)h_r \leq r < (n_r - 1)h_r, \\ b_1(\frac{r}{h_r} - (n_r - 1)) & (n_r - 1)h_r \leq r < n_r h_r, \\ b_2(\frac{r}{h_r} - n_r) & n_r h_r \leq r < (n_r + 1)h_r, \\ b_3(\frac{r}{h_r} - (n_r + 1)) & (n_r + 1)h_r \leq r < (n_r + 2)h_r, \\ 0 & \text{otherwise.} \end{cases}$$

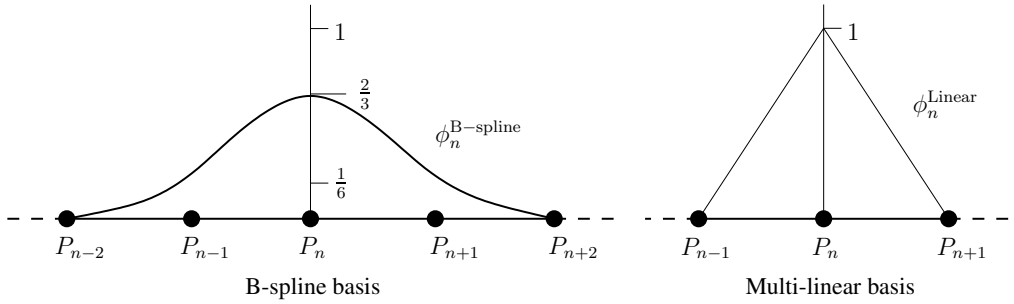

Figure 3.4: Illustration of the B-spline and Multi-linear nodal basis functions on the 1D domain.

Here, $n_r = \lfloor \frac{r}{h_r} \rfloor$ and the cubic B-spline polynomials are given by $b_0(t) = \frac{t^3}{6}$, $b_1(t) = \frac{-3t^3+3t^2+3t+1}{6}$, $b_2(t) = \frac{3t^3-6t^2+4}{6}$, $b_3(t) = \frac{-t^3+3t^2-3t+1}{6}$, $\forall\ t \in [0\,1]$. In Figure 3.4a, a schematic of the 1D B-spline nodal basis function is shown. Note that, unlike the Lagrange basis, in the case of the B-spline basis the nodal parameters $\{u_n\}_{n=1}^N$ do not necessarily represent the actual solution of the PDE at the corresponding nodes $\{P_n\}_{n=1}^N$.

3.3.3 Multi-linear basis

Similar to the B-spline basis, the multi-linear nodal basis functions are defined on a uniform mesh by a tensor product of a set of linear polynomials $\{b_0, b_1\}$ as [140]:

$$\phi_n^{\text{Linear}}(\mathbf{x}) = \prod_r \phi_{n_r}^{\text{Linear}}(r), \qquad r \in \{x, y, z\}, \tag{3.10}$$

where:

$$\phi_{n_r}^{\text{Linear}}(r) = \begin{cases} b_0(\frac{r}{h_r} - (n_r - 1)) & (n_r - 1)h_r \leq r < n_r h_r, \\ b_1(\frac{r}{h_r} - n_r) & n_r h_r \leq r < (n_r + 1)h_r, \\ 0 & \text{otherwise.} \end{cases}$$

Here, $n_r = \lfloor \frac{r}{h_r} \rfloor$ and the linear polynomials are given by $b_0(t) = t$, $b_1(t) = 1 - t$, $\forall\ t \in [0\,1]$. A schematic of the 1D multi-linear basis function is shown in Figure 3.4b. It is interesting to note that, when the mesh spacings $\{h_x, h_y, h_z\}$ are chosen equal to the underlying Cartesian grid resolution, the use of multi-linear basis with the FEM method can be seen as equivalent to the finite difference method (FDM). Further, the nodal parameters $\{u_n\}_{n=1}^N$ arising from the use of the multi-linear basis correspond to the actual solution of the PDE at the nodes $\{P_n\}_{n=1}^N$ respectively.

3.4 Non-uniform mesh generation

The non-uniform discretization of the problem domain is an important aspect of the FEM method. As opposed to the FDM method where the discretization has to be uniform, the FEM method allows for non-uniform meshes that can be adapted depending on the accuracy of the solution desired in the different regions of the problem domain. One of the standard approaches for non-uniform mesh generation is to choose (either manually or automatically) the mesh nodes such that the density of

the mesh nodes is dependent on the desired accuracy of the solution, i.e., the density of the mesh nodes is chosen to be relatively higher in regions where a more accurate solution is desired than in regions where an inaccurate solution can be tolerated. Then, Delaunay triangulation (tetrahedralization) is performed based on these chosen mesh nodes, which tessellates the domain into triangles (tetrahedra) to obtain a non-uniform mesh which has a finer resolution in the regions where a higher density of mesh nodes was chosen as opposed to a coarser resolution in the regions where a lower density of mesh nodes was chosen. In particular, if the domain can be represented using an image, as is the case in our work on image registration and segmentation, we can then use the image features to automatically guide the placement of mesh nodes. This is because, in general we desire a more accurate solution (hence a higher density of mesh nodes) in regions with high number of image features as opposed to homogeneous regions with fewer features. Therefore, in our work the following image-adaptive mesh generation procedure proposed by Yang et *al.* [134] is employed:

(1) Given an image $I : \Omega \rightarrow \mathbb{R}$, the feature map $I_f : \Omega \rightarrow \mathbb{R}$ is computed such that $I_f(\mathbf{x}) = \zeta(\mathbf{x})/\bar{\zeta}$ where $\zeta(\mathbf{x}) = \max |I_\theta^{''}(\mathbf{x})|$, $\theta \in [0, 2\pi]$ and $\bar{\zeta}$ is a normalizing constant. $I_\theta^{''}$ denotes the second order directional derivative of I.

(2) Halftone the feature image I_f to obtain a binary image $I_b : \Omega \rightarrow \{0, 1\}$.

(3) Input the locations of the "white" pixels in the binary image I_b as initial mesh nodes to a Delaunay mesh generation algorithm.

(4) Refine the mesh to obtain the final non-uniform mesh adapted to the salient image features.

In Figure 3.5, the above steps are illustrated on a 2D image. In the case of 3D images, we consider the 3D image as a collection of 2D slices and therefore input the union of all the initial mesh nodes chosen on each of the 2D slices to a Delaunay tetrahedralization algorithm. We used TRIANGLE [109] and TETGEN [111] packages for Delaunay triangulation and tetrahedralization respectively.

3.5 Summary

We introduced the basic concepts involved in devising finite element method (FEM) based solutions to partial differential equations (PDEs) and the equivalent variational energy minimization formulations. Specifically, we explored the various nodal basis functions that can be used for the finite element approximation and also discussed a content-adaptive strategy for the generation of a non-uniform mesh which is important for harnessing the full potential of the FEM method.

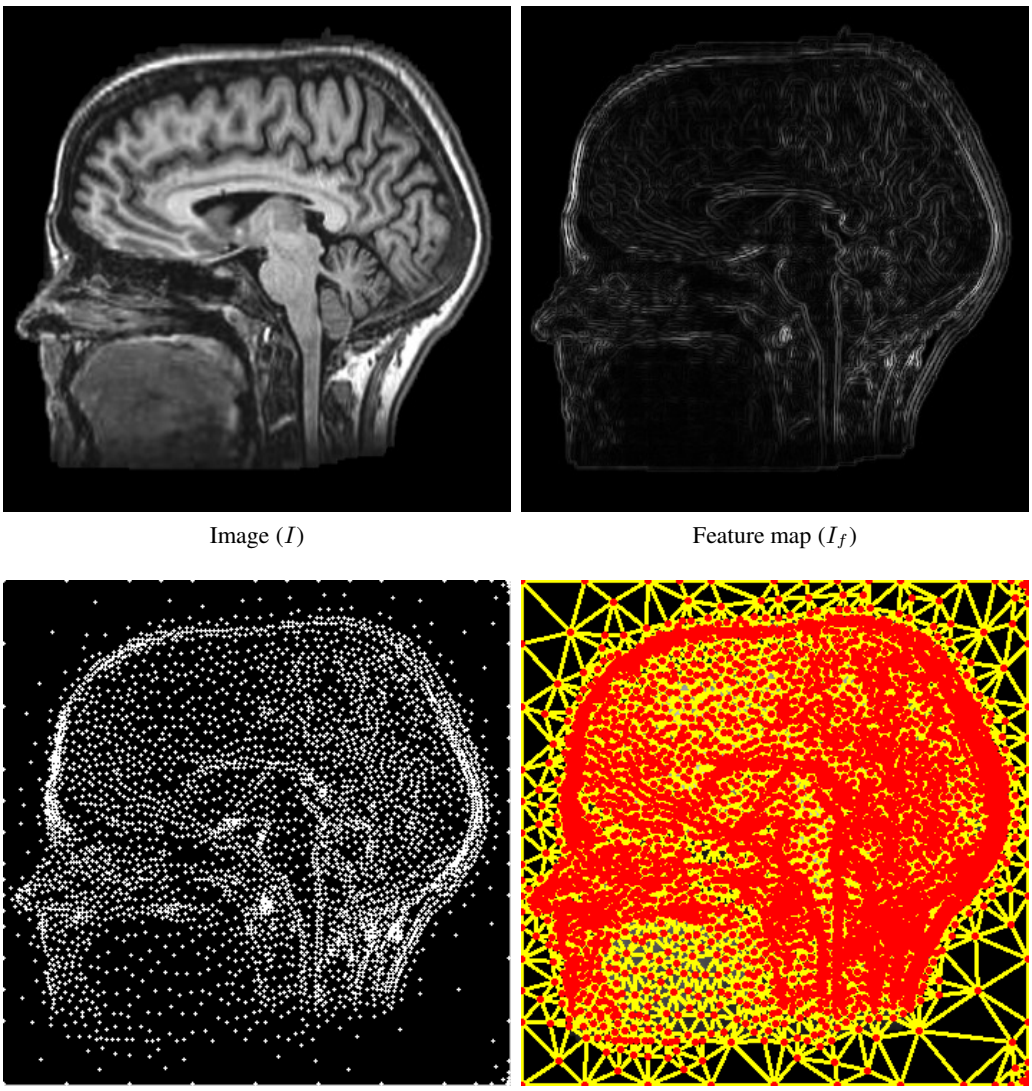

Image (I) Feature map (I_f)

Halftoned (I_b) Non-uniform mesh

Figure 3.5: Illustration of the non-uniform mesh generation. The basic idea here is to first compute a feature map I_f corresponding to the image I. Then, the feature map is converted into a binary halftoned image I_b. The "white" pixels in the halftoned image are input as initial node locations to a Delaunay mesh generation and refinement algorithm to obtain the final non-uniform mesh.

Chapter 4

A unified FEM-based framework for image registration and segmentation

In this chapter, new methods for image registration and segmentation are presented that comprise the core of the proposed work in this thesis. The registration and segmentation methods developed here make an extensive use of the finite element method (FEM) for computational efficiency. Firstly, a FEM-based parametric deformable registration method that employs diffusion-based regularization is presented. Then, a template-based parametric deformable model for multi-region segmentation is introduced, which uses a FEM deformable mesh smoothed by a diffusion-based regularizer. One of the main contributions in this thesis is to cast both these methods into a single unified FEM-based energy minimization framework with a common diffusion-based regularizer and a data term dependent on the specific method. Hence, an abstract construct is formulated under which both the deformable registration and template-based segmentation tasks can be seen as having the same goal. Further, this abstract formulation is general to also encompass the discrete deformable registration method proposed later in Chapter 5.

4.1 Abstract formulation of registration and segmentation

The fundamental abstraction to consider is that, all the registration and segmentation methods proposed in our work involve two images, $I_A : \Omega_A \rightarrow \mathbb{R}$, $\Omega_A \subset \mathbb{R}^\nu$ and $I_B : \Omega_B \rightarrow \mathbb{R}$, $\Omega_B \subset \mathbb{R}^\nu$, $\nu = 2$ or 3. In the proposed registration methods, I_B is chosen as the source image to be registered to the template image I_A, whereas in the template-based segmentation method I_A is chosen as the template image that is used to segment the image I_B. Further, Ω is denoted as the abstract domain on which the data term is defined. In the registration methods, the data term is computed on the template domain $\Omega \equiv \Omega_A$. In the template-based segmentation method, it is defined on the image domain $\Omega \equiv \Omega_B$. Next, abstractly the goal in all our proposed registration and segmentation methods can be seen as estimating an unknown vector field $\mathbf{V} : \Omega_A \rightarrow \mathbb{R}^K$, $K \in \mathbb{N}$ between the images I_A and I_B. This vector field $\mathbf{V}$ corresponds to the unknown deformation field in the con-

tinuous registration and template-based segmentation methods presented in this chapter. Lastly, we unify the terminology across the registration and segmentation methods and henceforth refer to the image-based E_{image} and smoothness-based E_{smooth} terms as data E_D and regularization E_R terms respectively. The terminology of image-based E_{image} and smoothness-based E_{smooth} terms was previously used in the context of segmentation using deformable models discussed in Section 2.2.

With these abstractions in place, the data E_D and diffusion-based regularization E_R^{diff} terms corresponding to the unified FEM-based energy minimization framework are defined as:

$$E_D[\mathbf{V}; I_A, I_B] = \frac{1}{2}\int_{\Omega} \Psi(\mathbf{V}; I_A, I_B)\, d\mathbf{x}, \qquad E_R^{\text{diff}}[\mathbf{V}] = \frac{1}{2}\sum_{k=1}^{K}\int_{\Omega_A} \nabla V_k^{\mathrm{T}} W \nabla V_k\, d\mathbf{x}, \tag{4.1}$$

where $\mathbf{V} = [V_k]_{k=1}^{K}$. The diffusivity or stiffness field W defines the "type" of diffusion-based smoothing constraints that are being enforced on the unknown vector field $\mathbf{V}$. If an isotropic (i.e., uniform in all directions) smoothing of the vector field is desired then W is chosen as a scalar. However, if an anisotropic smoothing is needed then W is chosen as symmetric $\nu \times \nu$ matrix. A typical anisotropic strategy would be to smooth mostly along the direction of the edges in the image while avoiding smoothing across the edges [129]. In both the isotropic and anisotropic cases, smoothing can be made inhomogeneous by choosing $W \equiv W(\mathbf{x})$ to vary over the image domain Ω_A. In general, it is desirable to perform more smoothing in the image regions with homogeneous intensities when compared to the regions with salient image features.

The finite element approximation (see Eq. 3.1) of the vector field $\mathbf{V}$ over a uniform or non-uniform mesh $\mathcal{M} = (\{P_n\}_{n=1}^{N}, \triangle_h)$ can be written as:

$$\mathbf{V}(\mathbf{x}) = \sum_{n=1}^{N} \mathbf{V}_n \phi_n(\mathbf{x}; \mathcal{M}), \qquad \mathbf{x} \in \Omega_A, \tag{4.2}$$

where $\{\mathbf{V}_n\}_{n=1}^{N}$, $\mathbf{V}_n \in \mathbb{R}^K$ are the unknown nodal vector field parameters corresponding to the nodes $\{P_n\}_{n=1}^{N}$ respectively. Further, the nodal basis functions $\{\phi_n\}_{n=1}^{N}$ can be chosen from the Lagrange, cubic B-spline or multi-linear basis functions, as described in Section 3.3. Following the Ritz FEM method discussed in Section 3.2.2, the finite element approximation of the vector field $\mathbf{V}$ is incorporated into Eq. 4.1 and the data and regularization terms are re-written as:

$$\begin{aligned} E_D(\{\mathbf{V}_n\}_{n=1}^{N}; I_A, I_B) &= \frac{1}{2}\int_{\Omega} \Psi(\{\mathbf{V}\}_{n=1}^{N}; I_A, I_B)\, d\mathbf{x}, \\ E_R^{\text{diff}}(\{\mathbf{V}_n\}_{n=1}^{N}) &= \frac{1}{2}\sum_{k=1}^{K}\sum_{n=1}^{N} V_{kn} \sum_{m=1}^{N} V_{km} \int_{\Omega_A} (W\nabla\phi_n)^{\mathrm{T}} \nabla\phi_m\, d\mathbf{x}, \end{aligned} \tag{4.3}$$

where $\mathbf{V}_n = [V_{kn}]_{k=1}^{K}$. Note that the parametrization using the Ritz FEM method is similar to the parametric deformable registration methodology discussed in Section 2.1.2 and the parametric deformable models approach described in Section 2.2.2. The goal of our unified FEM-based energy minimization framework for registration and segmentation is to find the optimal nodal vector field parameters $\{\mathbf{V}_n^*\}_{n=1}^{N}$ through the minimization of the data term E_D, while ensuring the smoothness of the deformation field based on the regularization constraints encoded in the diffusion-based

regularization term E_R^{diff}. Below, two different approaches are presented for estimating the optimal nodal vector field parameters $\{\mathbf{V}_n^*\}_{n=1}^N$ that arise in Eq. 4.3: (1) the *variational-like* approach where the diffusion-based regularization term E_R^{diff} is added to the data term E_D which is followed by the minimization of this combined energy; (2) the *demons-like* approach where the minimization of the data term E_D and smoothing of the deformation field using the diffusion-based regularization term E_R^{diff} are performed in separate steps.

4.1.1 Variational-like approach

In the variational-like approach, the data term E_D and the regularization term E_R^{diff} are combined together to obtain the following energy which is minimized:

$$\begin{aligned} E(\{\mathbf{V}_n\}_{n=1}^N) &= E_D(\{\mathbf{V}_n\}_{n=1}^N; I_A, I_B) + \gamma E_R^{\text{diff}}(\{\mathbf{V}_n\}_{n=1}^N), \\ \{\mathbf{V}_n^*\}_{n=1}^N &= \underset{\{\mathbf{V}_n\}_{n=1}^N}{\operatorname{argmin}} \; E(\{\mathbf{V}_n\}_{n=1}^N), \end{aligned} \tag{4.4}$$

where the regularization parameter γ controls the relative weighting of the data and regularization terms. In order to minimize the above energy, the gradient of the energy with respect to the nodal vector field parameters $\{\mathbf{V}_n\}_{n=1}^N$ is set to zero, which yields the following set of $N \times K$ non-linear equations:

$$\begin{aligned} &\partial_{\mathbf{V}_n} E = \partial_{\mathbf{V}_n} E_D + \gamma \partial_{\mathbf{V}_n} E_R^{\text{diff}} = 0 \qquad\qquad n \in \{1, 2, \ldots, N\}, \\ \text{with} \quad &\partial_{\mathbf{V}_n} E_D = \frac{1}{2} \int_\Omega \partial_{\mathbf{V}_n} \Psi(\mathbf{x}; \{\mathbf{V}_n\}_{n=1}^N, I_A, I_B) = \int_\Omega \boldsymbol{\psi}(\mathbf{x}; \{\mathbf{V}_n\}_{n=1}^N, I_A, I_B) \rho_n(\mathbf{x}) \, d\mathbf{x}, \\ &\partial_{\mathbf{V}_n} E_R^{\text{diff}} = \sum_{m=1}^N \mathbf{V}_m \int_{\Omega_A} (W \nabla \phi_m)^{\mathrm{T}} \nabla \phi_n \, d\mathbf{x}, \end{aligned} \tag{4.5}$$

where $\boldsymbol{\psi}(\mathbf{x}; \{\mathbf{V}_n\}_{n=1}^N, I_A, I_B) = [\psi_k(\mathbf{x}; \{\mathbf{V}_n\}_{n=1}^N, I_A, I_B)]_{k=1}^K$ are the referred to as the *forces* and $\rho_n(\mathbf{x})$ are referred to as the *weights*.

An iterative scheme is now discussed for solving the set of $N \times K$ non-linear equations in Eq. 4.5 to determine the unknown nodal vector field parameters $\{\mathbf{V}_n\}_{n=1}^N$. By choosing $\boldsymbol{\Theta} = [\boldsymbol{\Theta}_k]_{k=1}^K$, where $\boldsymbol{\Theta}_k = [V_{km}]_{m=1}^N$ is as a $N \times 1$ vector of nodal parameter values corresponding to the dimension k, the above system of non-linear equations can be compactly written in the following matrix form as:

$$S\boldsymbol{\Theta}_k - \mathbf{f}_k(\boldsymbol{\Theta}) = 0, \qquad\qquad k \in \{1, 2, \ldots, K\}, \tag{4.6}$$

where $S = [s_{m,n}]_{m=1,n=1}^{N,N}$ is the $N \times N$ *stiffness* matrix and $\mathbf{f}_k(\boldsymbol{\Theta}) = [f_{km}(\boldsymbol{\Theta})]_{m=1}^N$ is the $N \times 1$ *force* vector defined as:

$$s_{m,n} = \gamma \int_{\Omega_A} (W \nabla \phi_n)^{\mathrm{T}} \nabla \phi_m \, d\mathbf{x}, \qquad f_{km}(\boldsymbol{\Theta}) = -\int_\Omega \psi_k(\mathbf{x}; \boldsymbol{\Theta}, I_A, I_B) \rho_m \, d\mathbf{x}. \tag{4.7}$$

Then, an *incremental semi-implicit fixed-point iteration* scheme can be formulated as follows:

$$\partial_t \boldsymbol{\Theta}_k + S\boldsymbol{\Theta}_k - \mathbf{f}_k(\boldsymbol{\Theta}) \approx \frac{(\boldsymbol{\Theta}_k^{t+1} - \boldsymbol{\Theta}_k^t)}{\tau} + S\boldsymbol{\Theta}_k^{t+1} - \mathbf{f}_k(\boldsymbol{\Theta}^t) = 0, \qquad k \in \{1, 2, \ldots, K\}, \tag{4.8}$$

Algorithm 2 Variational-like unified FEM-based framework for registration and segmentation

Require: I_A, I_B, $\mathcal{M}(\{P_n\}_{n=1}^N, \Delta_h)$
Ensure: $\{\mathbf{V}_n^*\}_{n=1}^N$

1: At iteration $t = 0$, initialize $\mathbf{V}_n = \mathbf{V}_n^0$
2: **while** $t <=$ max_iter and convergence not reached **do**
3: Compute the forces $\boldsymbol{\psi}(\mathbf{x}; \{\mathbf{V}_n^t\}_{n=1}^N, I_A, I_B)$ for all pixels (voxels) $\mathbf{x} \in \Omega$
4: Compute the weights as $\rho_n^t(\mathbf{x})$ for all pixels (voxels) $\mathbf{x} \in \Omega$
5: Assemble the stiffness matrix S and the force vector $\mathbf{f}$ according to Eq. 4.7
6: Solve the linear system of equations in Eq. 4.11 to compute the nodal updates $\{\delta\mathbf{V}_n^t\}_{n=1}^N$
7: Update $\mathbf{V}_n^{t+1} = \mathbf{V}_n^t + \delta\mathbf{V}_n^t$
8: **end while**

where τ is a small time-step. Rearranging the above we get:

$$(\mathrm{Id}_N + \tau S)\boldsymbol{\Theta}_k^{t+1} = \boldsymbol{\Theta}_k^t + \tau \mathbf{f}_k(\boldsymbol{\Theta}^t), \qquad k \in \{1, 2, \ldots, K\}, \tag{4.9}$$

where Id_N is a $N \times N$ identity matrix. Now, $\boldsymbol{\Theta}_k^{t+1}$ can be expressed in terms of the nodal update field $\delta\boldsymbol{\Theta}_k^t$ as:

$$\boldsymbol{\Theta}_k^{t+1} = \boldsymbol{\Theta}_k^t + \delta\boldsymbol{\Theta}_k^t, \qquad k \in \{1, 2, \ldots, K\}. \tag{4.10}$$

By substituting the above into Eq. 4.9 and rearranging we obtain the following set of $N \times K$ linear equations to be solved for the nodal update $\delta\boldsymbol{\Theta}_k^t$ at every iteration t:

$$(\mathrm{Id}_N + \tau S)\delta\boldsymbol{\Theta}_k^t = (-\tau S\boldsymbol{\Theta}_k^t + \tau \mathbf{f}_k(\boldsymbol{\Theta}^t)), \qquad k \in \{1, 2, \ldots, K\}. \tag{4.11}$$

To summarize, in this scheme the final unknown nodal vector field parameters $\{\mathbf{V}_n^*\}_{n=1}^N \equiv \boldsymbol{\Theta}^*$ are computed incrementally by adding the current estimate of the unknown nodal vector field parameters $\{\mathbf{V}_n^t\}_{n=1}^N \equiv \boldsymbol{\Theta}^t$ with a nodal update field $\{\delta\mathbf{V}_n^t\}_{n=1}^N \equiv \delta\boldsymbol{\Theta}^t$ according to Eq. 4.10, i.e., $\{\mathbf{V}_n^{t+1} = \mathbf{V}_n^t + \delta\mathbf{V}_n^t\}_{n=1}^N$. The nodal updates $\{\delta\mathbf{V}_n^t\}_{n=1}^N \equiv \delta\boldsymbol{\Theta}^t$ at each iteration t are computed by solving the system of $N \times K$ linear equations in Eq. 4.11. The variational-like unified FEM-based minimization framework for registration and segmentation is outlined in Algorithm 2.

4.1.2 Demons-like approach

In the demons-like approach, the nodal update field parameters $\{\delta\mathbf{V}_n^t\}_{n=1}^N$ are computed solely based on the gradient of the data term as follows:

$$\delta\mathbf{V}_n^t = -\mathcal{F}((\partial_{\mathbf{V}_n} E_D)^t) = -\epsilon \frac{\int_\Omega \boldsymbol{\psi}(\mathbf{x}; \{\mathbf{V}_n^t\}_{n=1}^N, I_A, I_B)\rho_n^t(\mathbf{x})\, d\mathbf{x}}{\int_\Omega \rho_n^t(\mathbf{x})\, d\mathbf{x}}, \qquad n \in \{1, 2, \ldots, N\}, \tag{4.12}$$

where ϵ is a small time-step. The current estimate of the nodal deformation field parameters $\{\mathbf{V}_n^t\}_{n=1}^N$ is updated using the current nodal update field parameters $\{\delta\mathbf{V}_n^t\}_{n=1}^N$ as $\{\mathbf{V}_n^{t+1} = \mathbf{V}_n^t + \delta\mathbf{V}_n^t\}_{n=1}^N$. Then, the updated estimate of the deformation field $\mathbf{V}^{t+1}$ is smoothed using the diffusion-based

regularization term E_R^{diff} through the minimization of the following energy functional:

$$E[\hat{\mathbf{V}}] = \frac{1}{2}\int_{\Omega_A} ||\hat{\mathbf{V}} - \mathbf{V}||^2 \, d\mathbf{x} + \gamma E_R^{\text{diff}}[\hat{\mathbf{V}}], \tag{4.13}$$

where $\hat{\mathbf{V}}$ is the regularized deformation field we wish to estimate using the initial non-smooth deformation field $\mathbf{V}$ and γ is a parameter that controls the effect of the diffusion-based regularizer. We can see that the Euler-Lagrange equation corresponding to the above energy is given by the following reaction-diffusion PDE of the form given in Eq. 3.2:

$$\nabla_{\hat{\mathbf{V}}} E = (\hat{\mathbf{V}} - \mathbf{V}) - \gamma\nabla(W\nabla\hat{\mathbf{V}}) = 0 \equiv \hat{\mathbf{V}} - \gamma\nabla(W\nabla\hat{\mathbf{V}}) = \mathbf{V}. \tag{4.14}$$

Solving the above reaction-diffusion PDE is equivalent to smoothing the deformation field using the diffusion-based regularizer. Therefore, in order to solve the above PDE, the Ritz FEM method is followed and the finite element approximation in Eq. 4.2 is used to parametrize both the unknown smooth deformation field $\hat{\mathbf{V}}$ and the known non-smooth deformation field $\mathbf{V}$ to obtain a finite-dimensional approximation to the energy E in Eq. 4.13 as:

$$E(\{\hat{\mathbf{V}}_n\}_{n=1}^N) = \frac{1}{2}\int_{\Omega_A} \Big|\Big|\sum_{n=1}^{N}(\hat{\mathbf{V}}_n - \mathbf{V}_n)\,\phi_n\Big|\Big|^2 \, d\mathbf{x} + \gamma E_R^{\text{diff}}(\{\hat{\mathbf{V}}_n\}_{n=1}^N). \tag{4.15}$$

In order to minimize the above energy, it's gradient with respect to the nodal deformation field parameters $\{\hat{\mathbf{V}}_n\}_{n=1}^N$ is set to zero, which results in the following set of $N \times K$ linear equations:

$$\nabla_{\hat{\mathbf{V}}_n} E = \sum_{m=1}^{N}(\hat{\mathbf{V}}_m - \mathbf{V}_m)\int_{\Omega_A}\phi_m\phi_n \, d\mathbf{x} + \gamma\sum_{m=1}^{N}\hat{\mathbf{V}}_m\int_{\Omega_A}(W\nabla\phi_n)^{\mathrm{T}}\nabla\phi_m \, d\mathbf{x} = 0, \qquad n \in \{1,2,\ldots,N\}. \tag{4.16}$$

Again, by choosing $\hat{\mathbf{\Theta}} = [\hat{\mathbf{\Theta}}_k]_{k=1}^K$, where $\hat{\mathbf{\Theta}}_k = [\hat{\mathbf{V}}_{km}]_{m=1}^N$ is as a $N \times 1$ vector of nodal parameter values corresponding to the dimension k, the above system of linear equations can be compactly written in the following matrix form as:

$$S\hat{\mathbf{\Theta}}_k - \mathbf{f}_k = 0, \qquad k \in \{1,2,\ldots,K\}, \tag{4.17}$$

where $S = [s_{m,n}]_{m=1,n=1}^{N,N}$ is the $N \times N$ stiffness matrix and $\mathbf{f}_k = [f_{km}]_{m=1}^N$ is the $N \times 1$ *load* vector defined as:

$$S_{m,n} = \int_{\Omega_A}\phi_n\phi_m \, d\mathbf{x} + \gamma\int_{\Omega_A}(W\nabla\phi_n)^{\mathrm{T}}\nabla\phi_m \, d\mathbf{x}, \qquad f_{km} = V_{km}\int_{\Omega_A}\phi_n\phi_m \, d\mathbf{x}. \tag{4.18}$$

The above system of linear equations can be easily solved to obtain the unknown smooth vector field $\hat{\mathbf{\Theta}} \equiv \{\hat{\mathbf{V}}_n\}_{n=1}^N$. The demons-like unified FEM-based minimization framework for registration and segmentation is summarized in Algorithm 3.

In the rest of this chapter, our proposed continuous deformable registration and template-based segmentation methods are discussed in detail following the unified FEM-based energy minimization framework developed until now. The discussion primarily pertains to the data terms used in these methods as both these methods use the common diffusion-based regularization term.

Algorithm 3 Demons-like unified FEM-based framework for registration and segmentation

Require: I_A, I_B, $\mathcal{M}(\{P_n\}_{n=1}^N, \Delta_h)$
Ensure: $\{\mathbf{V}_n^*\}_{n=1}^N$

1: At iteration $t = 0$, initialize $\mathbf{V}_n = \mathbf{V}_n^0$
2: **while** $t <=$ max_iter and convergence not reached **do**
3: Compute the forces $\boldsymbol{\psi}(\mathbf{x}; \{\mathbf{V}_n^t\}_{n=1}^N, I_A, I_B)$ for all pixels (voxels) $\mathbf{x} \in \Omega$
4: Compute the weights as $\rho_n^t(\mathbf{x})$ for all pixels (voxels) $\mathbf{x} \in \Omega$
5: Compute the nodal updates according to Eq. 4.12:
$\delta\mathbf{V}_n^t = -\epsilon \frac{\int_\Omega \boldsymbol{\psi}(\mathbf{x}; \{\mathbf{V}_n^t\}_{n=1}^N, I_A, I_B)\rho_n^t(\mathbf{x})\, d\mathbf{x}}{\int_\Omega \rho_n^t(\mathbf{x})\, d\mathbf{x}}$
6: Update $\mathbf{V}_n^{t+1} = \mathbf{V}_n^t + \delta\mathbf{V}_n^t$
7: Smooth the deformation field $\mathbf{V}^{t+1}$ by solving a reaction-diffusion PDE on the mesh $\mathcal{M}$ using the FEM framework (see Eq. 4.13 - Eq. 4.17)
8: **end while**

4.2 FEM-based continuous deformable registration

Traditionally, uniform meshes along with the finite difference method (FDM) have been used in the implementation of deformable registration methods, as discussed in Section 2.1. However, such a uniform discretization approach is inefficient for deformable registration. This is because a finer resolution is needed to capture the deformation field in the regions that have a high number of image features, whereas in the homogeneous regions with fewer features relatively coarser resolution is sufficient. In this regard, the less explored FEM-based approach is ideal for the deformable registration task, especially for medical image registration. The main advantage in the FEM-based approach is that it allows for the use of a non-uniform discretization of the problem domain. By employing a non-uniform mesh well adapted to the image-features and the Lagrange basis functions (see Eq. 3.7), the deformation field can be parametrized with a significantly lower number of degrees of freedom (DOF) compared to the traditional deformation models defined on uniform meshes. Consequently, this leads to a more computationally efficient solution to the deformable registration problem. As discussed earlier in Section 2.1.2, there have been a few efforts [40], [56], [89] towards using the FEM method for deformable image registration. However, these methods use complex bio-mechanical models to model the elastic behavior of the underlying anatomy in medical images. These models are usually tuned to a specific type of medical image registration task and hence are not applicable for general deformable image registration. On the contrary, we propose the use of the FEM method for solving the problem of deformable registration using diffusion-based regularization constraints, which can be imposed in a wider range of image registration tasks. Further, apart from the Lagrange basis based deformation model, our FEM-based deformable registration method can also incorporate the traditional deformation models defined on uniform meshes. In particular, the diffusion-based non-parametric deformation model [72] discussed in Section 2.1.1 and the popular cubic B-spline free form deformation (FFD) model [101] discussed in Section 2.1.2 can be integrated into our FEM-based registration method through the use of the multi-linear basis functions in Eq.

3.10 and the cubic B-spline basis functions in Eq. 3.9 respectively.

4.2.1 Problem formulation

Consider a source image $I_S : \Omega_S \to \mathbb{R}, \Omega_S \subset \mathbb{R}^\nu$ to be registered to a template image $I_T : \Omega_T \to \mathbb{R}$, $\Omega_T \subset \mathbb{R}^\nu$ and $\mathbf{U} : \Omega_T \to \mathbb{R}^\nu$ be the unknown dense deformation field to be estimated between the source and template images. The data term corresponding to the proposed FEM-based parametric deformable registration method with diffusion-based regularization is given by the sum of squared differences (SSD) similarity measure:

$$E_D[\mathbf{U}; I_T, I_S] = \frac{1}{2}\int_{\Omega_T} (I_S(\mathbf{x} + \mathbf{U}(\mathbf{x})) - I_T(\mathbf{x}))^2 \, d\mathbf{x}. \tag{4.19}$$

The finite element approximation of the deformation field $\mathbf{U} = \sum_{n=1}^{N} \mathbf{U}_n \phi_n$ in Eq. 4.2 can be incorporated into the data term E_D in equation Eq. 4.19 to obtain:

$$E_D[\{\mathbf{U}_n\}_{n=1}^N; I_T, I_S] = \frac{1}{2}\int_{\Omega_T} (I_S(\xi(\mathbf{x}; \{\mathbf{U}_n\}_{n=1}^N)) - I_T(\mathbf{x}))^2 \, d\mathbf{x}, \tag{4.20}$$

$$\text{where} \quad \xi(\mathbf{x}; \{\mathbf{U}_n\}_{n=1}^N) = \mathbf{x} + \sum_{n=1}^{N} \mathbf{U}_n \phi_n(\mathbf{x}).$$

Following the unified FEM-based energy minimization framework in Section 4.1, the goal of our FEM-based parametric deformable registration method is to find the optimal nodal deformation field parameters $\{\mathbf{U}_n^*\}_{n=1}^N$ that minimize the data term E_D while ensuring smoothness using the diffusion-based regularizer E_R^{diff}. The minimization can be performed either using the variational-like approach in Algorithm 2 or the demons-like approach in Algorithm 3. Accordingly, the forces $\boldsymbol{\psi}(\mathbf{x}; \{\mathbf{U}_n\}_{n=1}^N, I_T, I_S)$ and the weights $\{\rho_n(\mathbf{x})\}_{n=1}^N$ corresponding to the data term E_D in Eq. 4.20 can be derived as:

$$\boldsymbol{\psi}(\mathbf{x}; \{\mathbf{U}_n\}_{n=1}^N, I_T, I_S) = (I_S(\xi(\mathbf{x}; \{\mathbf{U}_n\}_{n=1}^N)) - I_T(\mathbf{x}))\nabla I_S|_{\mathbf{x}=\xi(\mathbf{x};\{\mathbf{U}_n\}_{n=1}^N)}, \tag{4.21}$$

$$\rho_n(\mathbf{x}) = \phi_n(\mathbf{x}), \qquad n \in \{1, 2, \ldots, N\}.$$

In the variational-like approach, as an alternative to the additive update in step 7, Algorithm 2, the following compositional update can also be used:

$$\mathbf{U}_n^{t+1} = \mathbf{U}_n^t \circ \delta\mathbf{U}_n^t = \sum_{m=1}^{N} \mathbf{U}_m^t \phi_m(P_n + \delta\mathbf{U}_n^t) + \delta\mathbf{U}_n^t, \qquad n \in \{1, 2, \ldots, N\}. \tag{4.22}$$

In the case when the compositional update is employed, the warped gradient of the source image $\nabla I_S|_{\mathbf{x}=\xi(\mathbf{x};\{\mathbf{U}_n\}_{n=1}^N)}$ in the force term of Eq. 4.21 needs to be replaced with the gradient of the warped source image $\nabla I_S(\xi(\mathbf{x}; \{\mathbf{U}_n\}_{n=1}^N))$. Similarly, the compositional update can also be used in place of the additive update in step 6 of the demons-like approach given in Algorithm 3. Further, in the demons-like approach, the value of the nodal update field parameter $\delta\mathbf{U}_n^t$ computed using Eq. 4.12 at a node P_n of the mesh $\mathcal{M}$ can be interpreted as the weighted average of the forces

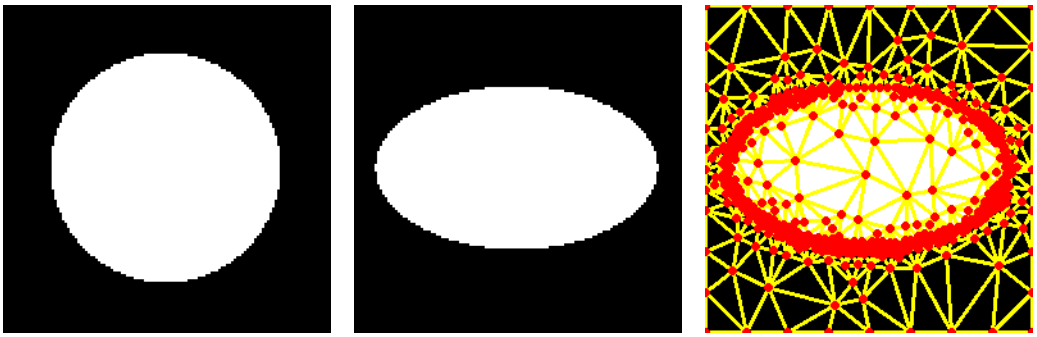

Source Template Non-uniform mesh

Figure 4.1: Binary image data used in the sanity check of the proposed FEM-based continuous deformable registration method. A binary circle was considered as the source to be registered to a binary ellipse template. The non-uniform mesh required for the Lagrange basis functions was generated on the binary ellipse template using the image-adaptive mesh generation procedure in Section 3.4.

$\psi(\mathbf{x}; \{\mathbf{U}_n^t\}_{n=1}^N, I_T, I_S)$ computed at each pixel (voxel) $\mathbf{x}_i$ overlapping the elements adjacent to the node P_n in the mesh $\mathcal{M}$. This weighted averaging implicitly acts as *fluid-like* regularization of the deformation field.

4.2.2 Sanity check

In this section, a sanity check of the proposed FEM-based continuous deformable registration method is performed before proceeding to the more elaborate validation experiments in Section 4.2.3. The goal of the sanity check testing was to determine if the proposed FEM-based minimization framework obtains a valid solution to the deformable registration problem. In particular, the focus was on testing whether the use of the Lagrange basis parametrization yields a valid solution. Also, both the variational-like approach in Algorithm 2 and the demons-like minimization approach in Algorithm 3 along with the additive and the compositional updates were tested for validity. In this regard, a binary circle source image was chosen to be registered to a template ellipse image as shown in Figure 4.1. Here, the isotropic homogeneous diffusivity model $W(\mathbf{x}) = 1.0$ was chosen and the regularization parameter was set to $\gamma = 1.0$. The corresponding results obtained using the four different minimization strategies, namely, demons-like with additive update, demons-like with compositional update, variational-like with additive update and variational-like with compositional update were shown in figures Figure 4.2-4.5 respectively. It can be observed that in all the four cases the FEM-based continuous registration method was able to deform the circle into the ellipse. Further, the recovered deformation fields were smooth and invertible as displayed by the vector (color) plots and the Jacobian maps. Also, it should be noted that the obtained solutions were stable as shown by the convergence plots of the sum of squared differences error (SSDE). Hence, in summary the FEM-based minimization framework using the Lagrange parametrization is a valid approach to solve the deformable registration problem.

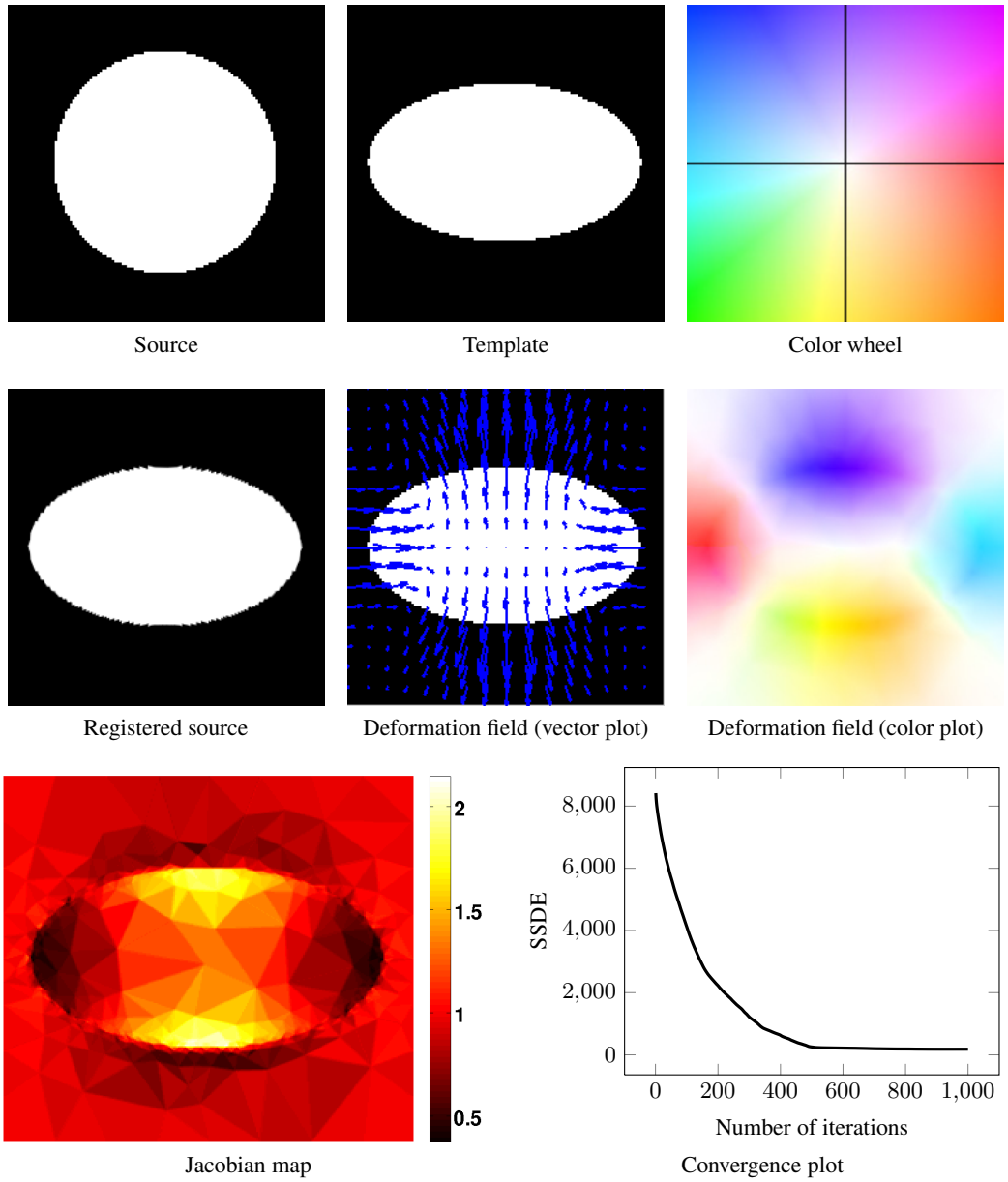

Figure 4.2: Simple illustration of the proposed FEM-based continuous deformable registration method implemented using Lagrange basis functions and the demons-like minimization with the additive update. Based on the Jacobian map and the color (vector) plot of the deformation field, it can be seen that a smooth and an invertible transformation was recovered between the circle and the ellipse. Further, this corresponds to a stable solution as shown by the convergence plot of the sum of squared differences error (SSDE). In the upcoming experiments on synthetic 2D brain MRI data shown in figures Figure 4.6 - 4.11, only the color plot of the deformation field is displayed.

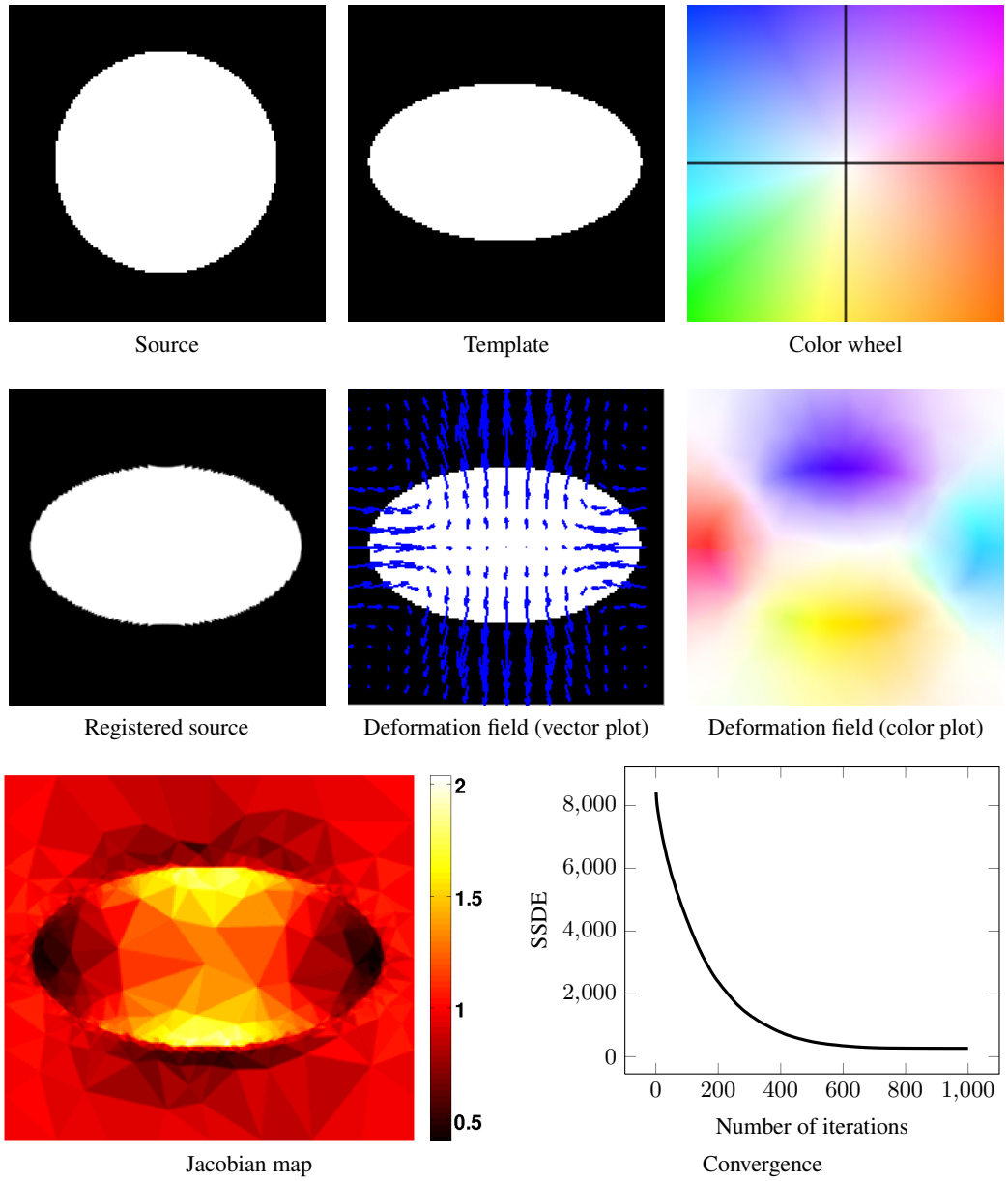

Figure 4.3: Simple illustration of the proposed FEM-based continuous deformable registration method implemented with Lagrange basis functions and the demons-like minimization using the compositional update. Based on the Jacobian map and the color (vector) plot of the deformation field, it can be seen that a smooth and an invertible transformation was recovered between the circle and the ellipse. Further, this corresponds to a stable solution as shown by the convergence plot of the sum of squared differences error (SSDE). In the upcoming experiments on synthetic 2D brain MRI data shown in figures Figure 4.6 - 4.11, only the color plot of the deformation field is displayed.

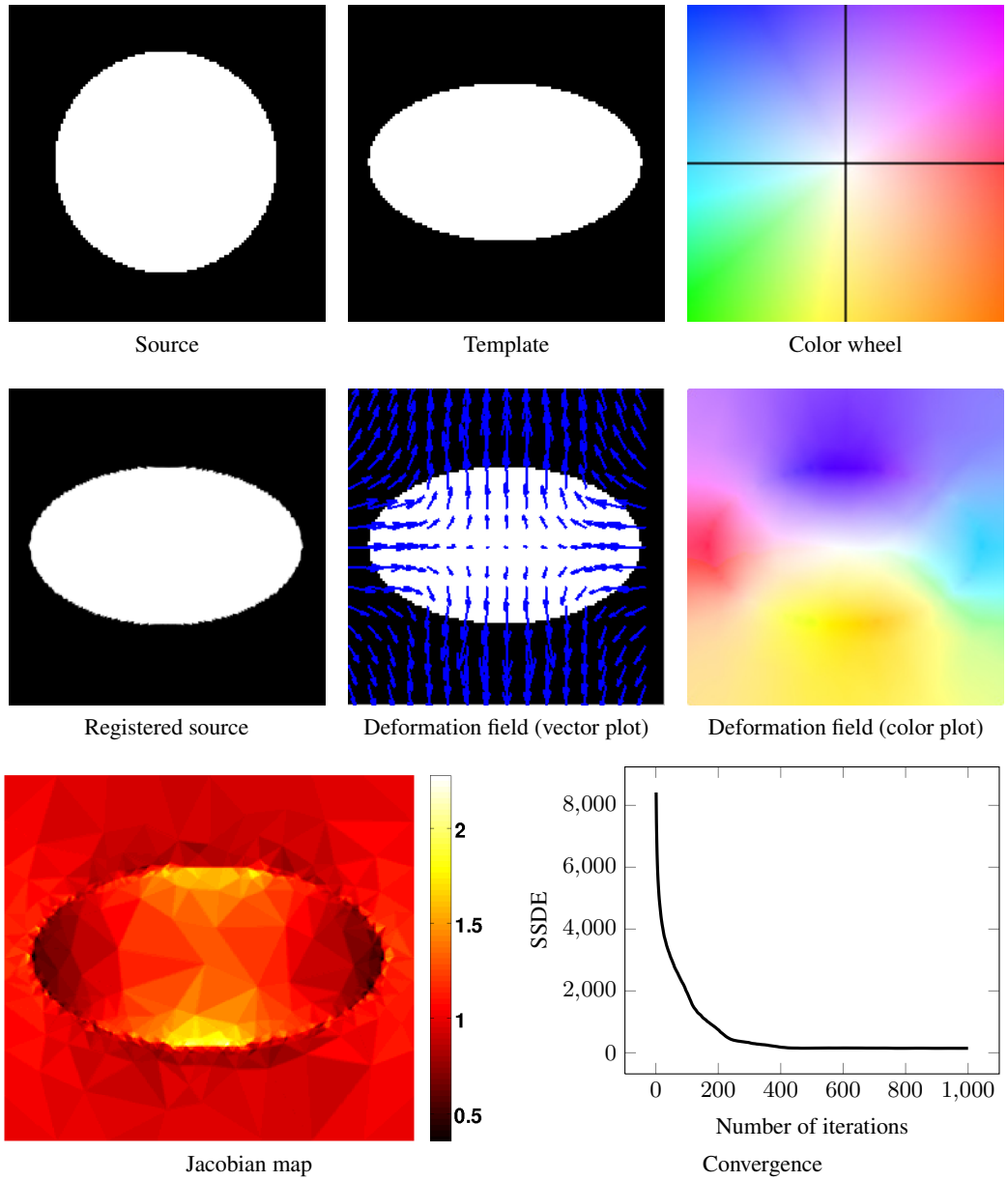

Figure 4.4: Simple illustration of the proposed FEM-based continuous deformable registration method implemented with Lagrange basis functions and the variational-like minimization using the additive update. Based on the Jacobian map and the color (vector) plot of the deformation field, it can be seen that a smooth and an invertible transformation was recovered between the circle and the ellipse. Further, this corresponds to a stable solution as shown by the convergence plot of the sum of squared differences error (SSDE). In the upcoming experiments on synthetic 2D brain MRI data shown in figures Figure 4.6 - 4.11, only the color plot of the deformation field is displayed.

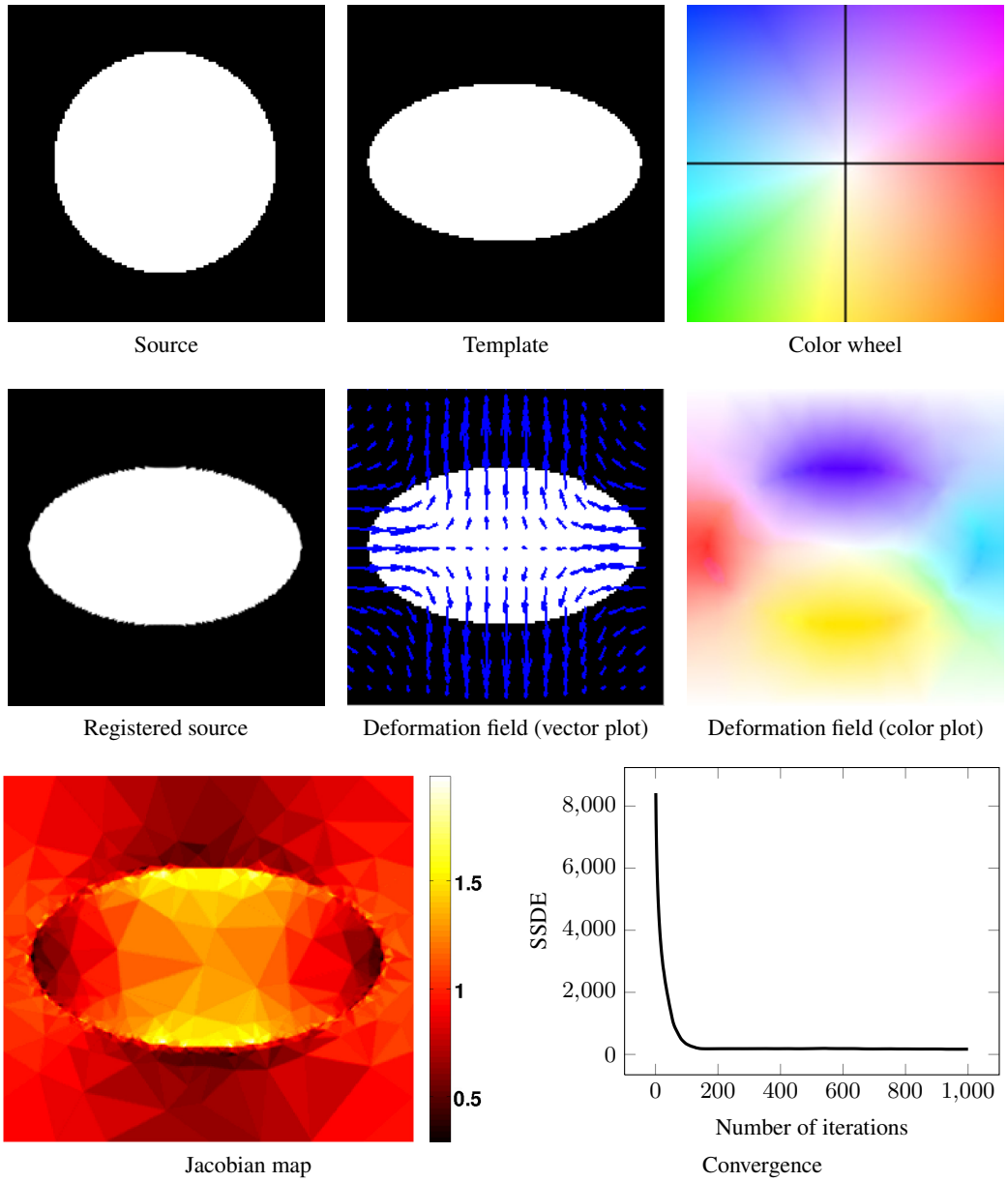

Figure 4.5: Simple illustration of the proposed FEM-based continuous deformable registration method implemented with Lagrange basis functions and the variational-like minimization using the compositional update. Based on the Jacobian map and the color (vector) plot of the deformation field, it can be seen that a smooth and an invertible transformation was recovered between the circle and the ellipse. Further, this corresponds to a stable solution as shown by the convergence plot of the sum of squared differences error (SSDE). In the upcoming experiments on synthetic 2D brain MRI data shown in figures Figure 4.6 - 4.11, only the color plot of the deformation field is displayed.

4.2.3 Experiments

In this section, the proposed FEM-based deformable registration method is tested on synthetic and real medical images. The general objective of the following experiments is to determine the best possible settings for the proposed FEM-based registration method with respect to the nodal basis functions, the optimization scheme and the diffusivity model. These settings are then fixed and the proposed FEM-based registration method is compared against the other popular deformable registration methods on a benchmark medical image data in Chapter 6. A short description of the three data sets used in the following experiments is given below and they are illustrated in Figure 4.6 and Figure 4.7:

- **Synthetic 2D MRI data**: A synthetic 353×354 magnetic resonance image (MRI) was chosen as the source image and 5 different template images were generated using known sinusoidal ground truth deformation fields, as shown in Figure 4.6. The use of sinusoidal deformation fields for the validation of registration algorithms is quite common [128], [18], [104].

- **Real 3D MRI brain data**: A subset of 6 MRI scans was chosen from the publicly available LPBA40 brain MRI database [105]. One of the 6 MRI images was arbitrarily fixed as the source image and the remaining 5 MRI images were chosen as the template images. The resolution of each scan was $217 \times 181 \times 181$ with a voxel spacing of 1mm $\times$ 1mm $\times$ 1mm. Manual segmentations of 56 anatomical regions were provided for each of the images (see Figure 4.7a).

- **Real 4D CT lung data**: A set of 5 pairs of 4D computed tomography (CT) images were selected from the DIR-Lab lung CT database [22]. Each image pair corresponds to the inhale and exhale phases of a breathing cycle. The inhale phase image was chosen as the template and the exhale phase image was selected as the source image. The resolution of the images was around $256 \times 256 \times 100$ with a voxel spacing of $\sim$ 1mm $\times$ 1mm $\times$ 2.5mm. Manual annotations of 300 corresponding landmark locations were provided for each image pair (see Figure 4.7b).

Note that, in order to ensure that the following experiments could be completed within a reasonable amount of time, only the synthetic 2D synthetic MRI data set was used in the basis comparison and optimization scheme comparison experiments. However, all three of the above data sets were used in the final diffusivity model comparison experiment. In all the following experiments, the proposed FEM-based registration method was implemented in a multi-resolution framework with 4 levels. Further, the regularization parameter was chosen manually as $\gamma = 0.1$. It should be noted that, as an alternative to the manual choice of the regularization parameter, the regularization parameter could be determined using the cross-validation experiments on a training dataset. In the below experiments, an isotropic homogeneous diffusivity model $W(\mathbf{x}) = 1.0$ was assumed unless

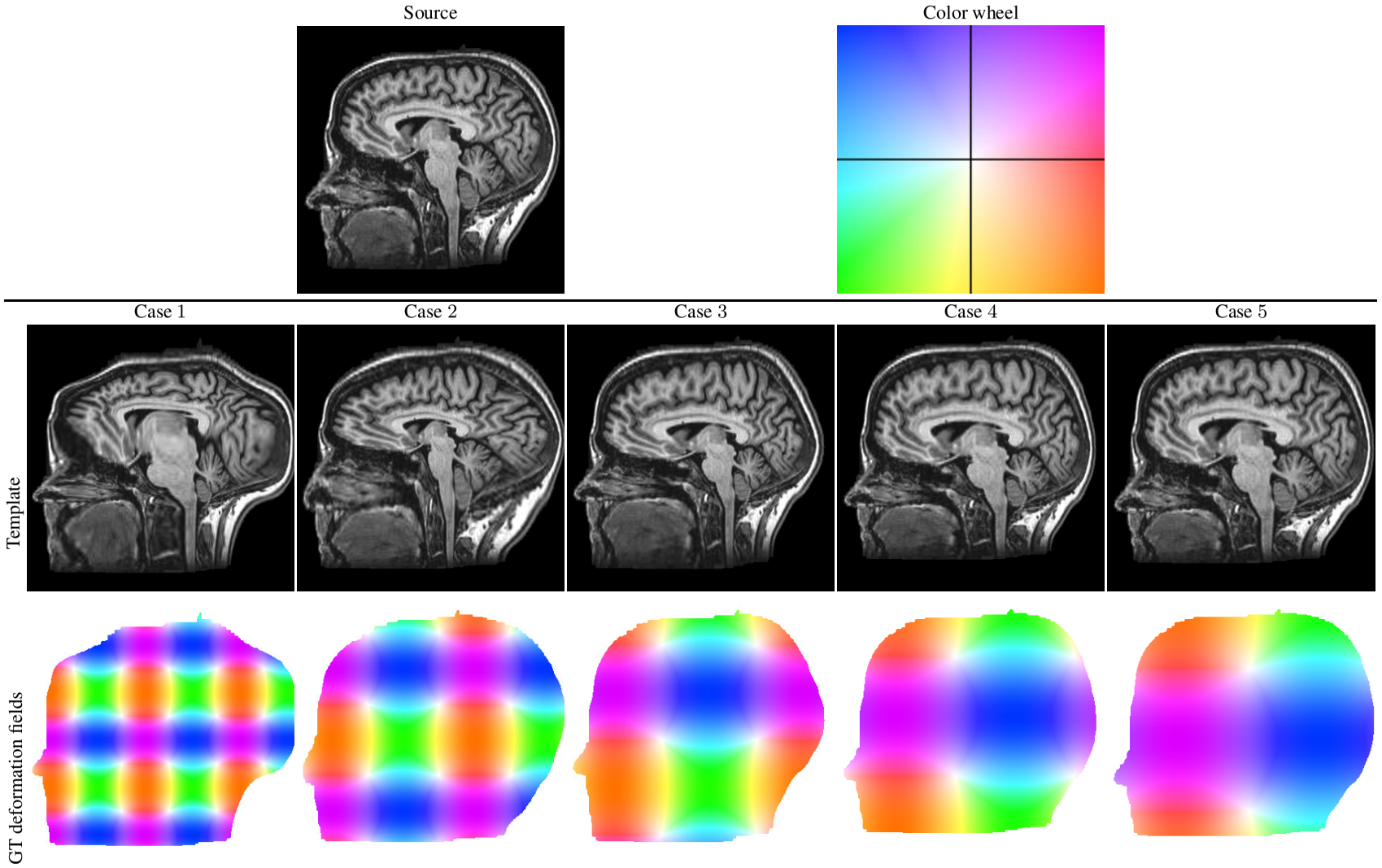

Figure 4.6: The synthetic 2D MRI data set generated using 5 different sinusoidal ground truth (GT) deformation fields.

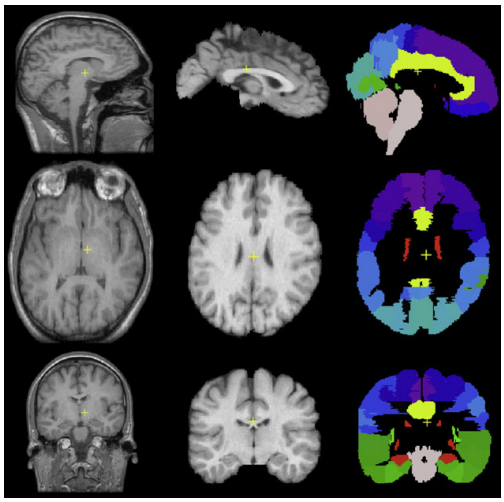

(a) The axial, saggital and coronal 2D slices of a sample brain from the LPBA40 dataset are shown with the various manually labeled anatomical regions (image was taken from Klein et *al.* [62]).

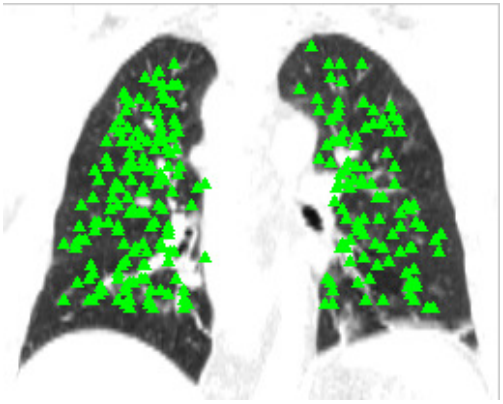

(b) A coronal 2D slice of the inhale phase image (which is used as the template) from the DIR-LAB 4D dataset is shown with the projected manually annotated landmarks (green triangles).

Figure 4.7: Illustration of the 3D data sets used for the evaluation of the registration methods.

specified otherwise. The proposed method was coded in MATLAB using the MEX facility and the experiments were performed on a Intel i7 3.60 GHZ machine with 64GB RAM.

Basis functions comparison

In the implementation of the proposed FEM-based registration method, the first choice is to decide the type of nodal basis functions to be used for the parametrization of the deformation field. In this regard, the comparative performance of the Lagrange, B-spline and multi-linear basis functions was evaluated on the synthetic 2D MRI data set. The B-spline and multi-linear basis parametrizations used a uniform mesh whereas the Lagrange basis parametrization employed a non-uniform mesh well adapted to the image features. The non-uniform mesh was generated on each of the 5 template images using the image-adaptive strategy described in Section 3.4. For this experiment, the demons-like minimization scheme in Algorithm 3 was used along with the compositional update. The demons minimization strategy with a compositional update is commonly used in diffusion-based deformable registration methods [112], [31]. The results obtained by registering the source image to each of the 5 template images using the different basis functions are reported in Table 4.1. Here, the registration accuracy was quantified using 4 measures, namely, the sum of squared difference error (SSDE) between the warped source and template images, the average angular error (AAE) between the ground truth and estimation deformation fields, the number of degrees of freedom (DOF) given as twice the number of nodes in the mesh and the computational time in seconds. The computational times reported in Table 4.1 correspond to the time taken for solving the set of linear equations in Eq. 4.17, which is the most computationally expensive step in the demons-like minimization scheme. Further, a plot of the deformation fields recovered using the different basis parametrizations between

	Source before regis.	**Lagrange basis parametrization**				B-spline basis parametrization				multi-linear basis parametrization			
Case	SSDE	**SSDE**	**AAE**	**DOF**	**Time**	SSDE	AAE	DOF	Time	SSDE	AAE	DOF	Time
1	5589.95	**140.39**	**12.18**	**12184**	**0.45**	524.04	14.86	43520	13.50	137.13	12.75	331588	24.34
2	4599.06	**46.22**	**2.98**	**10624**	**0.53**	240.29	2.50	43520	13.29	38.36	3.54	331588	24.23
3	5681.54	**35.02**	**3.24**	**11140**	**0.35**	300.52	2.13	43520	13.69	22.67	3.34	331588	24.18
4	4582.57	**36.41**	**1.64**	**11276**	**0.32**	352.19	2.83	43520	13.23	15.75	2.26	331588	24.34
5	5678.33	**23.62**	**1.74**	**11582**	**0.43**	357.62	1.72	43520	13.20	11.04	1.69	331588	24.65
Mean	5226.29	**56.33**	**4.36**	**11361**	**0.42**	354.93	4.81	43520	13.38	44.99	4.72	331588	24.35
Std.	581.30	**47.67**	**4.43**	**576**	**0.08**	105.73	5.63	0	0.21	52.54	4.56	0	0.18

Table 4.1: Comparative results obtained by the FEM-based deformable registration method with the different basis functions on the synthetic 2D MRI dataset. Here, the sum of squared differences error (SSDE), average angular error (AAE) in degrees, computational times in seconds and the number of degrees of freedom (DOF) are reported.

the source and the template images for case 1 are also shown in Figure 4.8. Based on the small mean SSDE and AAE values in Table 4.1, it can be inferred that the FEM-based registration method was successful in recovering the ground truth deformation fields using any of the three basis parametrizations. However, it can be clearly seen that the Lagrange basis parametrization of the deformation field offers a significant computational advantage over the other two basis parametrizations that are defined on uniform meshes. On an average, the use of the Lagrange basis parameterization resulted in at least 3 times lower DOF and hence made the FEM-based registration method run more than 30 times faster compared to when the B-spline and multi-linear basis parametrizations were used. More importantly, it can be clearly seen from the deformation field plots that the Lagrange basis parametrization obtained a higher accuracy near the skull regions compared to the B-spline basis parametrization. This better accuracy can be attributed to the spatially adaptive non-uniform mesh used by the Lagrange basis parametrization as opposed to the uniform mesh with a fixed resolution that was used by the B-spline parameterization. In Figure 4.8, notice that the non-uniform has a high node density near the skull region containing important image features leading to an improved performance of the Lagrange basis parametrization.

Optimization schemes comparison

In this experiment, the effect of the chosen optimization strategy on the accuracy of the proposed FEM-based registration method is investigated. Here, the deformation field was parametrized using the Lagrange basis functions. Both the variational-like approach in Algorithm 2 and demons-like approach in Algorithm 3 were considered along with the two possible update rules, i.e., additive and compositional updates. In Table 4.2, the performance of the different optimization schemes on the synthetic 2D MRI data set is presented. The computational times shown correspond to the time taken for solving the equations in Eq. 4.11 and Eq. 4.17 for the variational-like and demons-like minimization schemes respectively. It can be seen that both the variational-like and demons-like schemes require similar computational times. This is not surprising as both the schemes use the

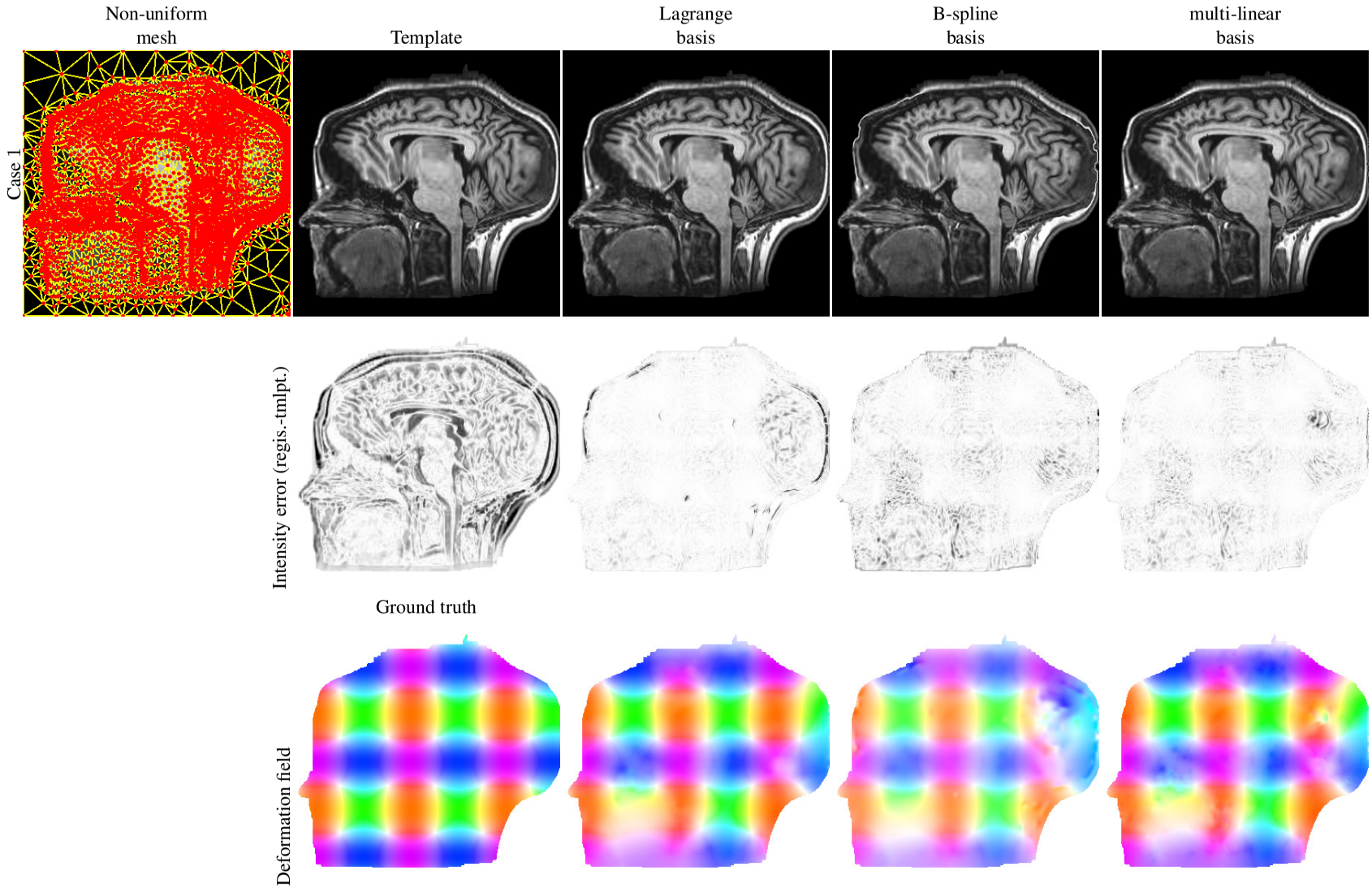

Figure 4.8: A sample visual result obtained by the FEM-based deformable registration method with the different basis functions on the synthetic 2D MRI dataset. Note that, in the intensity error (template-registered) images white means zero error and more dark the intensity implies more the error.

	Source before regis.	demons additive scheme			demons compositional scheme			**variational additive scheme**			variational compositional scheme		
Case	SSDE	SSDE	AAE	Time	SSDE	AAE	Time	**SSDE**	**AAE**	**Time**	SSDE	AAE	Time
1	5589.95	89.63	10.12	0.36	140.39	12.18	0.51	**50.39**	**4.22**	**0.49**	57.90	4.40	0.59
2	4599.06	37.46	2.47	0.35	46.22	2.98	0.39	**21.99**	**1.32**	**0.51**	42.51	1.60	0.52
3	5681.54	26.44	2.95	0.52	35.02	3.24	0.39	**4.31**	**0.56**	**0.53**	14.05	1.08	0.44
4	4582.57	19.49	1.63	0.40	36.41	1.64	0.45	**2.07**	**0.42**	**0.44**	18.33	0.89	0.59
5	5678.33	14.02	1.15	0.43	23.62	1.74	0.49	**2.89**	**0.44**	**0.46**	9.87	0.75	0.55
Mean	5226.29	37.41	3.66	0.41	56.33	4.36	0.45	**16.33**	**1.39**	**0.49**	28.53	1.74	0.54
Std.	581.30	30.48	3.68	0.07	47.67	4.43	0.06	**20.74**	**1.62**	**0.04**	20.73	1.52	0.06

Table 4.2: Comparative results obtained by the FEM-based deformable registration method using the Lagrange basis parametrization with the different optimization schemes on the synthetic 2D MRI dataset. Here, the sum of squared intensity errors error (SSDE), average angular error (AAE) in degrees and the computational times in seconds are reported.

same non-uniform mesh. However, the variational-like scheme achieves slightly more accurate registration results compared to the demons-like approach, as shown by the lower mean SSDE and AAE measures. Further, in the variational-like scheme, a small improvement in the registration accuracy is obtained by using the additive update instead of the compositional update. Particularly, it can seen from the deformation plots corresponding to case 1 in Figure 4.9 that the variational scheme (using either of the update rules) exhibits an improved accuracy in the tongue region (bottom-left region). Note in Figure 4.9 that the tongue region is relatively more homogeneous compared to the rest of the image. This implies that the variational scheme produced accurate results even in homogeneous regions with a lower node density (see the non-uniform mesh in Figure 4.8). Additionally, the variational-like scheme with the additive update exhibits a faster and a more stable convergence behavior as can be seen in Figure 4.10.

Diffusivity models comparison

The previous two experiments have established the Lagrange basis parametrization with a variational-like minimization scheme using the additive update as the ideal choice for the proposed FEM-based deformable registration method. However, until now only the simple homogeneous isotropic diffusivity model was considered. In this experiment, the more complex diffusivity models, namely, the Perona-Malik isotropic inhomogeneous diffusivity model [82] and the Nagel anisotropic inhomogeneous [76] diffusivity model are explored for a better registration performance of the FEM-based registration method, while using the Lagrange basis parametrization with the variational-additive minimization strategy. Here, the proposed FEM-based registration method was also tested on the 3D real MRI and 3D real CT data sets in addition to the 2D synthetic MRI data set. For the 3D real MRI data set, the registration accuracy was evaluated by mapping the 56 manual anatomical labels defined in the source image onto the template using the estimated deformation field. The Jaccard overlap measure was computed between the warped source labels and the template labels. For the 3D real CT data set, to evaluate the registration accuracy the 300 manual landmark positions in

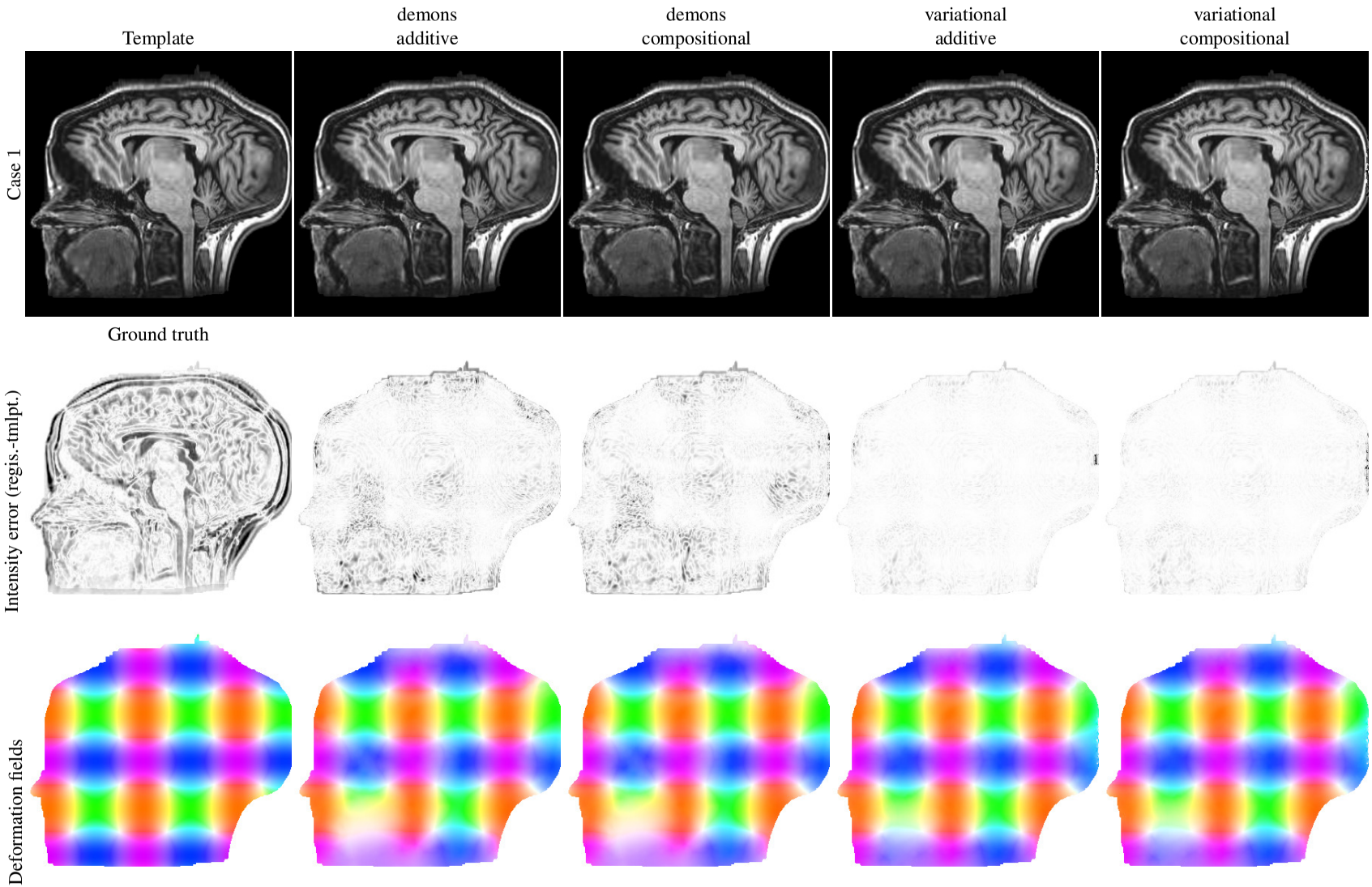

Figure 4.9: A sample visual result obtained by the FEM-based deformable registration method using the Lagrange basis parametrization with the different optimization schemes on the synthetic 2D MRI dataset. Note that, in the intensity error (template-registered) images white means zero error and more dark the intensity implies more the error.

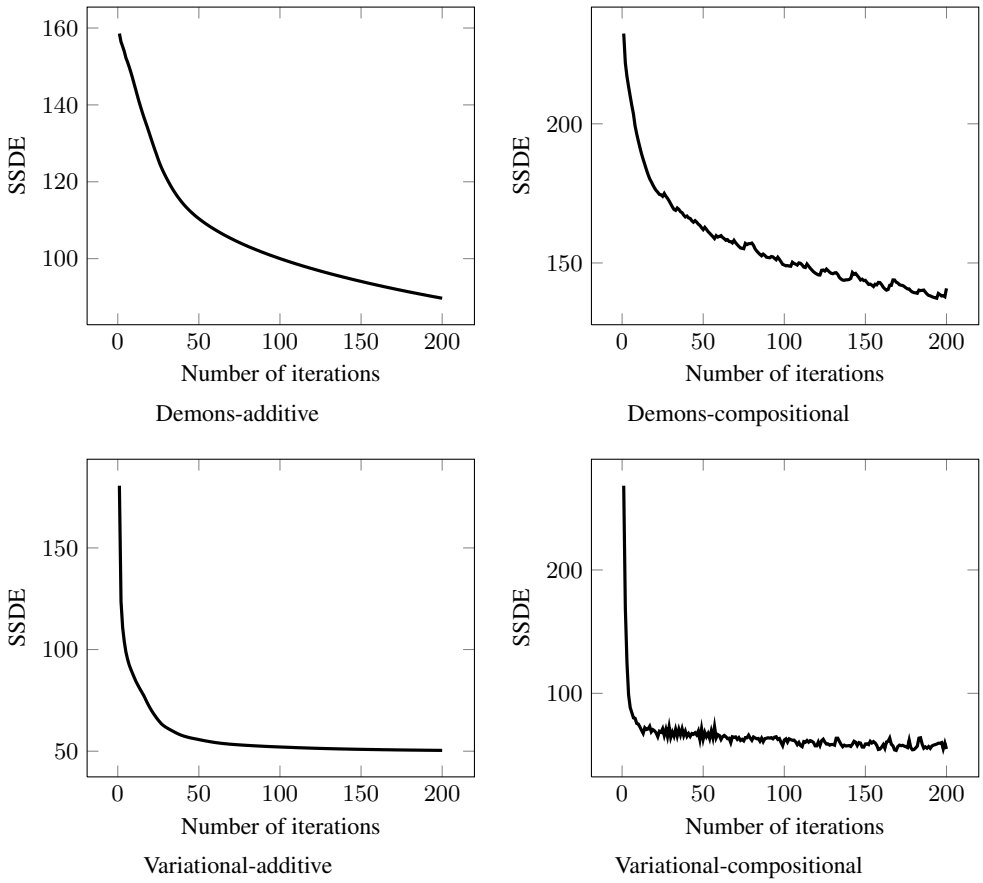

Figure 4.10: Convergence plots of the sum of squared intensity error error (SSDE) obtained using the FEM-based registration with Lagrange basis functions and the different optimization schemes on a sample case (case 1) of the synthetic 2D MRI data set. Note that the variational-like scheme with the additive update achieves a faster and a more stable convergence behavior compared to the other optimization schemes.

	Source before regis.			homogeneuous isotropic diffusivity				**Perona-Malik isotropic diffusivity**				Nagel anisotropic diffusivity			
	Synth. 2D	CT 3D	MRI 3D	Synth. 2D		CT 3D	MRI 3D	**Synth. 2D**		**CT 3D**	**MRI 3D**	Synth. 2D		CT 3D	MRI 3D
Case	SSDE	TRE	Jacc.	SSDE	AAE	TRE	Jacc.	**SSDE**	**AAE**	**TRE**	**Jacc.**	SSDE	AAE	TRE	Jacc.
1	5589.95	3.89	35.81	50.39	4.22	1.00	52.90	**52.09**	**3.95**	**1.00**	**53.03**	33.04	2.49	1.02	53.48
2	4599.06	4.34	47.18	21.99	1.32	1.00	56.76	**20.82**	**1.27**	**0.99**	**57.51**	17.03	1.19	1.01	57.15
3	5681.54	6.94	41.46	4.31	0.56	1.21	51.65	**4.12**	**0.61**	**1.16**	**51.99**	4.84	0.63	1.16	50.71
4	4582.57	9.83	38.68	2.07	0.42	1.47	56.11	**2.25**	**0.48**	**1.44**	**56.00**	1.34	0.35	1.43	56.72
5	5678.33	7.48	32.60	2.89	0.44	1.85	54.73	**3.04**	**0.57**	**1.65**	**54.09**	2.83	0.63	1.57	54.31
Mean	5226.29	6.50	39.15	16.33	1.39	1.30	54.43	**16.46**	**1.38**	**1.25**	**54.52**	11.81	1.06	1.24	54.48
Std.	581.30	4.83	13.73	20.74	1.62	1.07	9.73	**21.35**	**1.47**	**0.95**	**9.86**	13.39	0.86	0.92	10.25

Table 4.3: Comparative results obtained by the FEM-based deformable registration method using the Lagrange basis parametrization and the variational-additive optimization scheme with the different diffusivity models on the synthetic 2D MRI dataset, the real 3D brain MRI dataset and the real 3D CT lung dataset. Here, the sum of squared differences error (SSDE), average angular error (AAE) in degrees, Jaccard overlap score (%) and the target registration error (TRE) in millimeters are reported.

the inhale phase image were propagated to the exhale phase image using the estimated deformation fields. The target registration error (TRE) measure was computed between the warped and the actual landmark locations. The TRE measure is the Euclidean distance in millimeters (mm). In Table 4.3, the results obtained using the three different diffusivity models are shown and a sample visual result is shown in Figure 4.11 and Figure 4.12. It can be clearly seen that the use of an inhomogeneous diffusivity model (Perona-Malik or Nagel) results in a much better performance of the FEM-based registration method compared to the homogeneous diffusivity model on all the three data sets. However, the use of the anisotropic Nagel diffusivity model does not seem to improve results by much when compared to the isotropic Perona-Malik diffusivity. While the anisotropic Nagel diffusivity outperforms the isotropic Perona-Malik diffusivity on the 2D synthetic data set, it achieves similar results on the 3D real CT and 3D real MRI data sets. In fact it obtains a slightly worse average Jaccard score on the 3D MRI data set. In summary, the Perona-Malik inhomogeneous isotropic diffusivity model is chosen in the implementation of the proposed FEM-based deformable registration method.

4.3 FEM-based template-based multi-region segmentation

In medical image analysis tasks, the first step is often the segmentation of relevant anatomical structures from medical images. This is quite challenging as it typically involves the segmentation of multiple non-overlapping anatomical regions of interest (ROIs) with weak boundaries. The state-of-the-art methods for anatomical structure segmentation [98], [83], [87], [127] follow the atlas-based approach discussed previously in Section 2.3, where the image is segmented via deformable registration with a labeled intensity atlas. Similarly, our proposed method also employs the registration framework for multi-region segmentation. However, instead of using a labeled intensity atlas, a

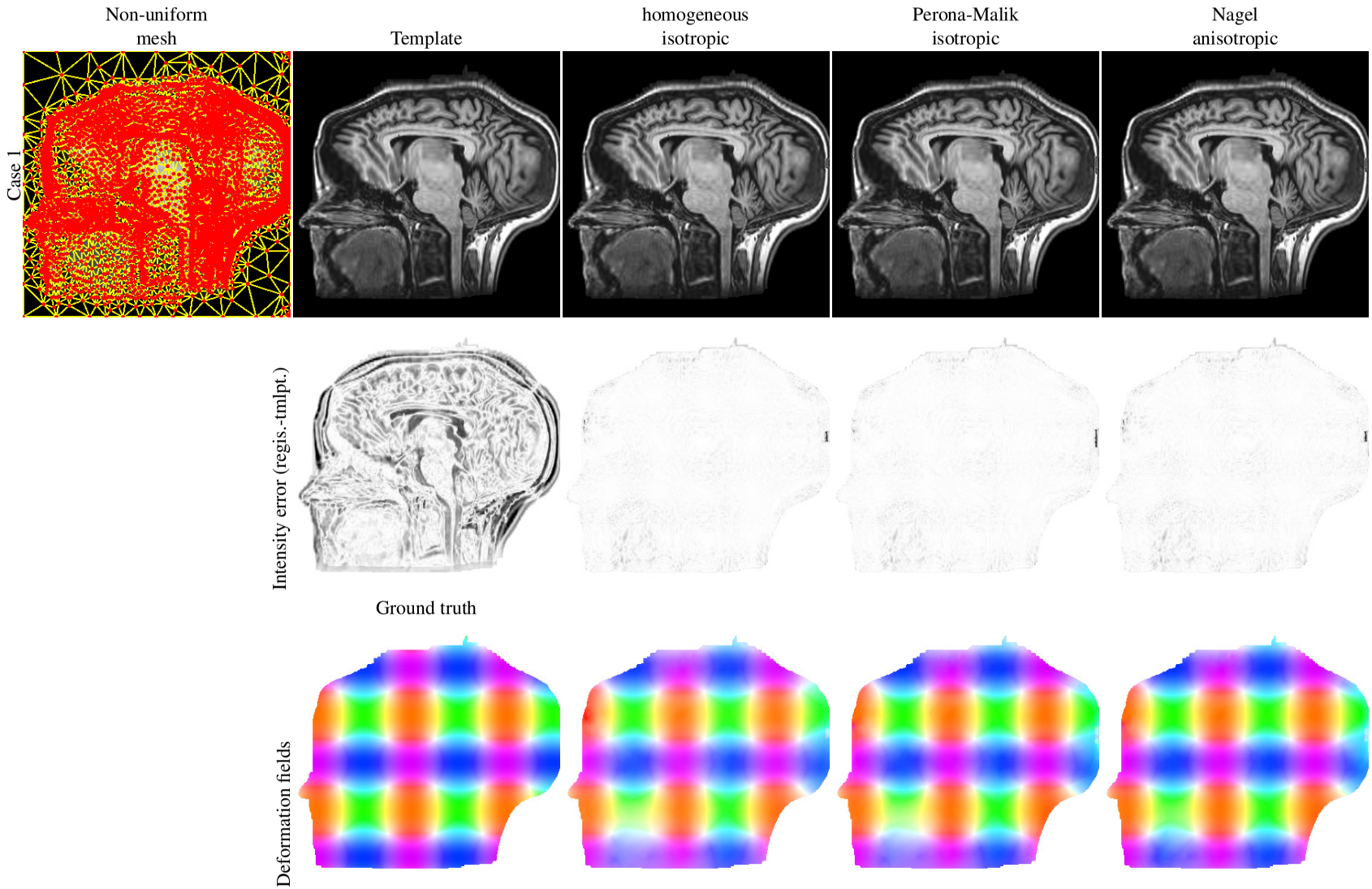

Figure 4.11: Sample visual comparative results obtained by the FEM-based deformable registration method using the Lagrange basis parametrization and the variational-additive optimization scheme with the different diffusivity models on the synthetic MRI 2D dataset. Note that, in the intensity error (template-registered) images white means zero error and more dark the intensity implies more the error.

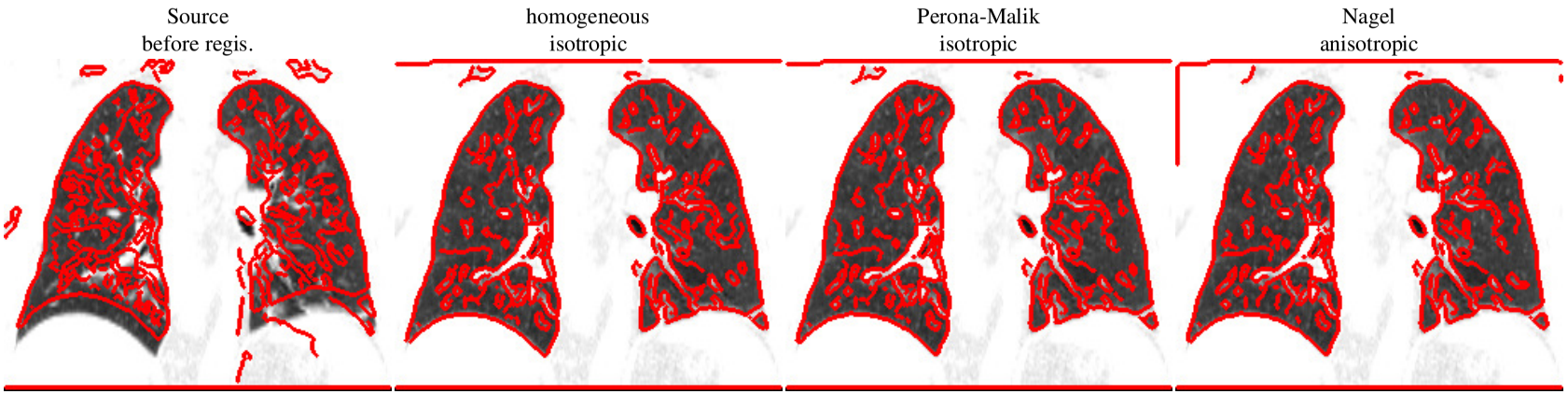

(a) 3D real CT image, Case 4 results. Here, contours of the original source image and the warped source image are overlayed on template image (a 2D slice was chosen).

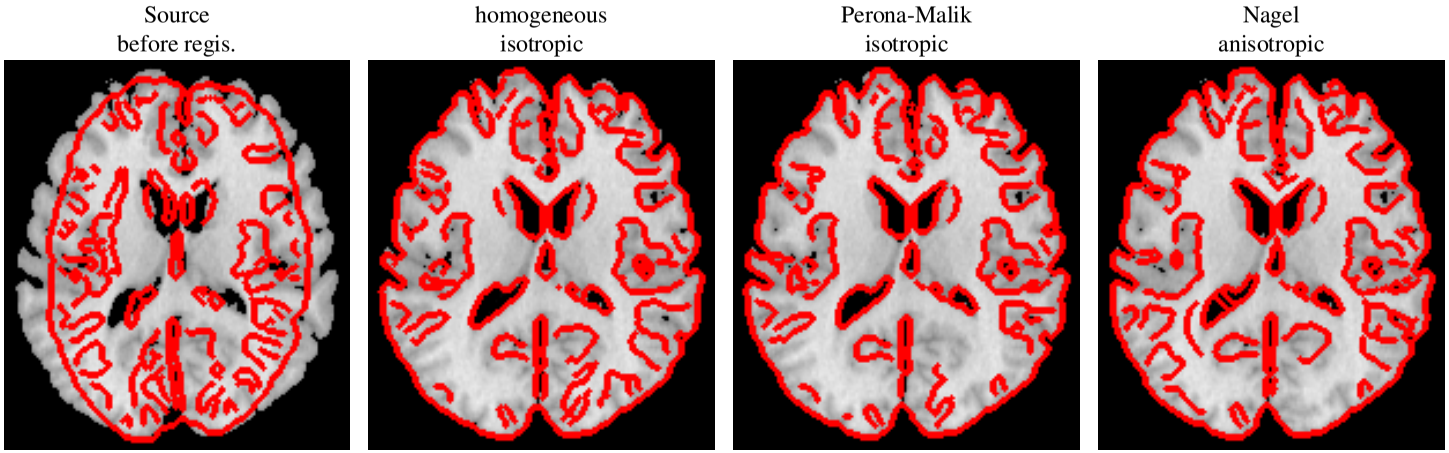

(b) 3D real MRI image, Case 5 results. Here, contours of the original source image and the warped source image contours are overlayed on template image (a 2D slice was chosen).

Figure 4.12: Sample visual comparative results obtained by the FEM-based deformable registration method using the Lagrange basis parametrization and the variational-additive optimization scheme with the different diffusivity models on the real 3D brain MRI dataset and the real 3D CT lung dataset.

label image defining the topology and layout of the ROIs is chosen as the template. Further, in contrast to the atlas-based approaches where a similarity score is minimized, in our proposed method the template is smoothly deformed such that a region-based segmentation energy is minimized. Such region-based segmentation energies were originally used within a level set based optimization framework [33], as discussed earlier in Section 2.2.1. But, in the context of anatomical structure segmentation the proposed template-based approach is more advantageous when compared to the level set approach. This is because the level sets are prone to topological changes which is not desirable, as the topology of the anatomical ROIs is already known and needs to be maintained throughout the segmentation process. On the other hand, in the template-based approach, the evolving segmentation boundaries are implicitly given by the contours of the initial ROIs defined in the template and the current estimate of the smooth deformation field between the template and the image. This template-based encoding of the segmentation boundaries naturally ensures that the topology of the ROIs is preserved. Moreover, it also allows us to directly handle multi-region segmentation that is not trivial within a level set formulation [132].

As discussed in Section 2.2.1 and Section 2.2.2, existing methods on template-based segmentation represent the deformation field between the template and the image using either a non-parametric deformation model [102], [65] or the popular cubic B-splines based free form deformation (FFD) model [55], [67]. However, a common drawback in both of these deformation models is that a uniform mesh is used to discretize the problem domain. This is inefficient because the deformation field is computed with the same accuracy everywhere even though detailed deformations are only needed along the contours of the ROIs. To address this issue, we propose to use the FEM method and parametrize the deformation field on a non-uniform mesh well adapted to the contours of the ROIs using the Lagrange basis functions defined in Eq. 3.7. This results in a computationally efficient solution to the template-based segmentation problem, as it involves minimization over a far fewer number of degrees of freedom (DOF) compared to the non-parametric and FFD deformation models. Further, the proposed FEM-based segmentation method is generalized so that it also encompasses the deformation models defined on uniform meshes. Specifically, the non-parametric and FFD deformation models are incorporated into the proposed FEM-based segmentation method through the use of multi-linear and cubic B-spline basis functions given in Eq. 3.10 and Eq. 3.9 respectively. Finally, it should be noted that the proposed FEM-based segmentation method is considerably different from the snakes energy based works [39], [106] discussed in Section 2.2.2. These works also use a FEM mesh for segmentation, but employ a explicit representation (see Figure 2.4a) of the segmentation boundary instead of the template-based representation used in our method (see Figure 2.4c).

In the template-based approach for segmentation, it is desirable to formulate the data term on the image domain using the original image I as opposed to formulating it on the template domain using the warped image $I(\mathbf{U})$. This is because the warped image $I(\mathbf{U})$ is a function of the deformation

field $\mathbf{U}$ and hence a data term formulated using the warped image $I(\mathbf{U})$ would result in a more complex overall energy landscape compared to the data term that was formulated using the original image I. While using a uniform mesh, it is quite straightforward to formulate the data term on the image domain [102], [65]. However, when a non-uniform mesh is used, this task becomes challenging because the non-uniform meshes are generated and defined on the template instead of the image. To address this issue, in the following sections, two different formulations, namely, the *inverse* and the *forward* formulations are developed for the proposed FEM-based multi-region template-based segmentation method. While the inverse formulation strictly assumes a non-uniform discretization and the Lagrange basis parametrization, the forward formulation can incorporate deformation models that are parametrized on either uniform or non-uniform meshes.

4.3.1 Inverse formulation

Consider an image $I : \Omega \rightarrow \mathbb{R}$, $\Omega \subset \mathbb{R}^{\nu}$ to be segmented using a template $I_T : \Omega \rightarrow \{1, 2, \ldots, R\}$, $\Omega \subset \mathbb{R}^{\nu}$, where R is the number of regions defined in the template. The segmentation task is formulated as finding the unknown dense deformation field $\mathbf{U} : \Omega_T \rightarrow \mathbb{R}^{\nu}$ to be estimated between the source and templates, where the region segmentation labels $\{1, 2, \ldots, R\}$ defined in the template I_T are mapped onto the image I using the inverse deformation field $\mathbf{U}^{-1} : \Omega \rightarrow \mathbb{R}^{\nu}$. The deformation field $\mathbf{U}$ corresponds to a transformation $\varphi : \Omega_T \rightarrow \Omega$, such that $\mathbf{x}^{'} = \varphi(\mathbf{x}) = \mathbf{x} + \mathbf{U}(\mathbf{x})$ and the inverse deformation field $\mathbf{U}^{-1}$ corresponds to a transformation $\varphi^{-1} : \Omega \rightarrow \Omega_T$, such that $\mathbf{x} = \varphi^{-1}(\mathbf{x}^{'}) = \mathbf{x}^{'} + \mathbf{U}^{-1}(\mathbf{x}^{'})$ as depicted in Figure 4.13. The inverse deformation field $\mathbf{U}^{-1}$ is used to formulate a data term similar to the one in the region-based Generalized Chan-Vese (GCV) energy in Eq. 2.33, on the image domain Ω as:

$$E_D[\mathbf{U}; I_T, I] = -\frac{1}{2}\sum_{r=1}^{R}\int_{\Omega} I_{Tr}(\mathbf{x}^{'} + \mathbf{U}^{-1}) \log(p_r(I(\mathbf{x}^{'}))) \, d\mathbf{x}^{'}, \tag{4.23}$$

where the probability density $p_r(I(\mathbf{x}^{'}))$ defines the intensity statistics for region r in Ω and $I_{Tr} : \Omega_T \rightarrow \{0, 1\}$ is a binary "region template" corresponding to each of the separate regions $r \in \{1, 2, \ldots, R\}$ defined in the template I_T. It can be seen in Figure 4.13 that the deformation field $\mathbf{U}$ induces a deformed mesh $\mathcal{M}^{'} = (\{P_n^{'}\}_{n=1}^{N}, \triangle_h)$ on the image domain Ω corresponding to the original mesh $\mathcal{M} = (\{P_n\}_{n=1}^{N}, \triangle_h)$. Consequently, the deformed mesh might not preserve the properties of the original mesh. Due to this reason the original mesh $\mathcal{M}$ needs to be strictly chosen as non-uniform mesh in the inverse formulation case. This is because, while a deformed non-uniform mesh would still behave as a non-uniform mesh, a deformed uniform mesh is not guaranteed to retain the uniform mesh characteristics. Hence, the following discussion is only valid for a non-uniform mesh and not for a uniform mesh. Similar to the finite element approximation of the deformation field $\mathbf{U} = \sum_{n=1}^{N} \mathbf{U}_n \phi_n$ in Eq. 4.2, the inverse deformation field $\mathbf{U}^{-1}$ can be approximated using the

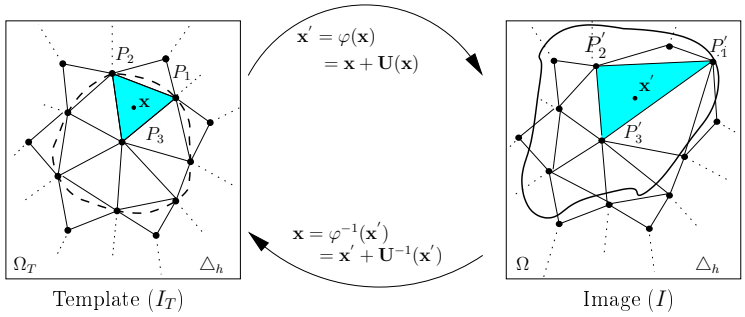

Figure 4.13: Illustration of the deformed mesh in the inverse formulation case. The dashed closed curve in the template (I_T) represents the boundary of the region of interest. The solid closed curve in the image I represents the actual region boundary.

nodal basis functions on the deformed mesh $\mathcal{M}'$ as:

$$\mathbf{U}^{-1}(\mathbf{x}') = \sum_{n=1}^{N} \mathbf{U}_n^{-1} \phi_n(\mathbf{x}'; \mathcal{M}'), \qquad \mathbf{x}' \in \Omega, \tag{4.24}$$

where $\{\mathbf{U}_n^{-1} = \mathbf{U}^{-1}(P_n')\}_{n=1}^N$ are the unknown nodal inverse deformation field parameters corresponding to the values of the inverse deformation field $\mathbf{U}^{-1}$ at the nodes $\{P_n'\}_{n=1}^N$ of the mesh $\mathcal{M}'$. Further, it can be easily shown that the nodal deformation field parameters $\{\mathbf{U}_n\}_{n=1}^N$ are related to the nodal inverse deformation field parameters $\{\mathbf{U}_n^{-1}\}_{n=1}^N$ as follows:

$$\begin{aligned} & P_n' = P_n + \mathbf{U}_n \quad \text{and} \quad P_n = P_n' + \mathbf{U}_n^{-1} \\ & \implies P_n = P_n + \mathbf{U}_n + \mathbf{U}_n^{-1} \\ & \implies \mathbf{U}_n^{-1} = -\mathbf{U}_n \end{aligned} \tag{4.25}$$

meaning that the value of the inverse deformation field at the nodes of the deformed mesh $\mathcal{M}'$ is the *negative* of the deformation field at the nodes of the original non-uniform mesh $\mathcal{M}$. The finite element approximation of the inverse deformation field in Eq. 4.24 along with the relation in Eq. 4.25 can be used to obtain a finite dimensional approximation of the data term E_D in Eq. 4.23 as:

$$E_D(\{\mathbf{U}_n\}_{n=1}^N; I_T, I) = -\frac{1}{2} \sum_{r=1}^{R} \int_{\Omega} I_{T_r}(\xi(\mathbf{x}'; \{-\mathbf{U}_n\}_{n=1}^N)) \log(p_r(I(\mathbf{x}'))) \, d\mathbf{x}'. \tag{4.26}$$

$$\text{where} \quad \xi(\mathbf{x}'; \{-\mathbf{U}_n\}_{n=1}^N) = \mathbf{x}' - \sum_{n=1}^{N} \mathbf{U}_n \phi_n(\mathbf{x}'; \mathcal{M}').$$

Following the unified FEM-based framework in section 4.1, the goal of the proposed template-based multi-region segmentation using the FEM method is to find the optimal nodal deformation field parameters $\{\mathbf{U}_n^*\}_{n=1}^N$ such that the data term E_D is minimized while ensuring the smoothness of the deformation field using the diffusion-based regularization term E_R^{diff}. The minimization can proceed using either the variational-like approach in Algorithm 2 or the demons-like approach in Algorithm 3. Accordingly, the forces $\boldsymbol{\psi}(\mathbf{x}'; \{\mathbf{U}_n\}_{n=1}^N, I_T, I)$ and the weights $\{\rho_n(\mathbf{x}')\}_{n=1}^N$ corresponding to

the data term E_D in Eq. 4.26 are given by:

$$\boldsymbol{\psi}(\mathbf{x}^{'};\{\mathbf{U}_n\}_{n=1}^{N},I_T,I) = \frac{1}{2}\sum_{r=1}^{R}\log(p_r(I(\mathbf{x}^{'})))\nabla I_{Tr}|_{\mathbf{x}'=\xi(\mathbf{x}';\{-\mathbf{U}_n\}_{n=1}^{N})},$$

$$\rho_n(\mathbf{x}^{'}) = \sum_{m=1}^{N}\frac{\partial\phi_m(\mathbf{x}^{'};\mathcal{M}^{'})}{\partial\mathbf{U}_n}\mathbf{U}_m + \phi_n(\mathbf{x}^{'};\mathcal{M}^{'}), \qquad n\in\{1,2,\ldots,N\}. \quad (4.27)$$

As discussed before in Section 4.2, the additive update in step 7, Algorithm 2 of the variational-like approach and step 6, Algorithm 3 of the demons-like approach can be replaced with the compositional update in Eq. 4.22. Similarly, while using the compositional update the warped gradient of the region template $\nabla I_{Tr}|_{\mathbf{x}'=\xi(\mathbf{x}';\{-\mathbf{U}_n\}_{n=1}^{N})}$ in the force term in Eq. 4.27 needs to be replaced with the gradient of the warped region template $\nabla I_{Tr}(\xi(\mathbf{x}^{'};\{-\mathbf{U}_n\}_{n=1}^{N}))$. Further, in the demons-like approach, the value of the nodal update field parameter $\delta\mathbf{U}_n^t$ computed using Eq. 4.12 at a node P_n of the original mesh $\mathcal{M}$ can be interpreted as the negative of the weighted average of the region forces $\boldsymbol{\psi}(\mathbf{x}^{'};\{\mathbf{U}_n^t\}_{n=1}^{N},I_T,I)$ at the pixels (voxels) in the image I that neighbor the corresponding node $(P_n^{'})^t$ of the deformed mesh $(\mathcal{M}^{'})^t$ at the iteration t. Again, this weighted averaging implicitly acts as fluid-like regularization.

4.3.2 Forward formulation

A disadvantage with the inverse formulation presented above is that, the nodal basis functions $\{\phi_n(\mathbf{x};(\mathcal{M}^{'})^t)\}_{n=1}^{N}$ corresponding to the deformed mesh $(\mathcal{M}^{'})^t$ have to be recomputed at every new iteration t. This adds considerably to the computational burden and therefore increases the overall run time of the proposed FEM-based multi-region template-based segmentation method. In order to avoid the recomputation of nodal basis functions, an alternate forward formulation of the template-based segmentation problem is devised. The basic idea in the forward formulation is to define the original mesh $\mathcal{M} = (\{P_n\}_{n=1}^{N},\triangle_h)$ on the image domain Ω instead of the template domain Ω_T. This is accomplished by mapping the original mesh generated on the template I_T at iteration $t = 0$ onto to the image domain Ω using an identity transformation, as illustrated in Figure 4.14. Consequently, the unknown deformation field $\mathbf{U}:\Omega\rightarrow\mathbb{R}^{\nu}$ now corresponds to the transformation from the image domain Ω to the template domain Ω_T, i.e., $\varphi:\Omega\rightarrow\Omega_T$, such that $\varphi(\mathbf{x}) = \mathbf{x}+\mathbf{U}(\mathbf{x})$. This is in contrast to the inverse formulation case, where the deformation field $\mathbf{U}$ represents a mapping from the template domain Ω_T to the image domain Ω. As a result of this modification, the region segmentation labels $\{1,2,\ldots,R\}$ defined in the template I_T can then be mapped onto the image I directly using the "forward" deformation field $\mathbf{U}:\Omega\rightarrow\mathbb{R}^{\nu}$, without having to rely on the inverse deformation field $\mathbf{U}^{-1}:\Omega_T\rightarrow\mathbb{R}^{\nu}$. Accordingly, the region-based data term E_D in Eq. 4.23 can be re-defined using the deformation field $\mathbf{U}$ as:

$$E_D[\mathbf{U};I_T,I] = -\frac{1}{2}\sum_{r=1}^{R}\int_{\Omega}I_{Tr}(\mathbf{x}+\mathbf{U})\log(p_r(I(\mathbf{x})))\,d\mathbf{x}. \quad (4.28)$$

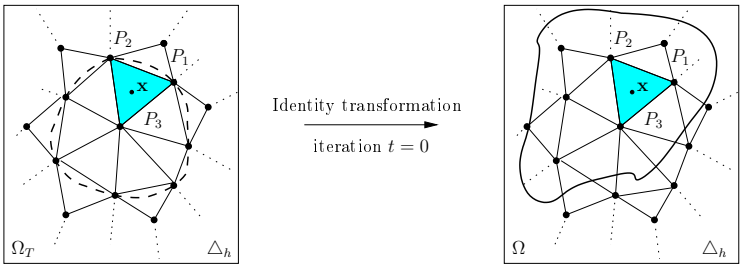

Template (I_T) Image (I)

Figure 4.14: Illustration of mapping the original mesh on to the image domain in the forward formulation case. The dashed closed curve in the template (I_T) represents the boundary of the region of interest. The solid closed curve in the source image I represents the actual region boundary.

Further, the diffusion-based regularization term E_D^{diff} in Eq. 4.1 is now be computed on the image domain Ω as opposed to the template domain Ω_T:

$$E_R^{\text{diff}}[\mathbf{U}] = \frac{1}{2}\sum_{k=1}^{\nu}\int_{\Omega} \nabla U_k^{\mathrm{T}} W \nabla U_k \, d\mathbf{x}. \tag{4.29}$$

Also, the finite element approximation in Eq. 4.24 can be re-written on the image domain Ω as follows:

$$\mathbf{U}(\mathbf{x}) = \sum_{n=1}^{N} \mathbf{U}_n \phi_n(\mathbf{x}; \mathcal{M}), \qquad \mathbf{x} \in \Omega, \tag{4.30}$$

where $\{\mathbf{U}_n\}_{n=1}^N$ are the unknown nodal deformation field parameters corresponding to the values of the deformation field $\mathbf{U}$ at the nodes $\{P_n\}_{n=1}^N$ of the mesh $\mathcal{M}$. Note that in the above there is no restriction on the choice of the mesh $\mathcal{M}$. It can be chosen as either a uniform or a non-uniform mesh and hence any of the Lagrange, cubic B-spline and multi-linear nodal basis functions discussed in Section 3.3 can used for the parametrization of the deformation field $\mathbf{U}$. This is in contrast to the inverse formulation where a non-uniform mesh with a Lagrange basis parametrization is required. The finite element approximation in Eq. 4.30 can be incorporated into the modified data E_D and regularization E_R^{diff} terms in Eq. 4.28 and Eq. 4.29 respectively to obtain:

$$E_D[\{\mathbf{U}_n\}_{n=1}^N; I_T, I] = -\frac{1}{2}\sum_{r=1}^{R}\int_{\Omega} I_{T_r}(\xi(\mathbf{x}; \{\mathbf{U}_n\}_{n=1}^N)) \log(p_r(I(\mathbf{x}))) \, d\mathbf{x},$$

$$E_R^{\text{diff}}(\{\mathbf{U}_n\}_{n=1}^N) = \frac{1}{2}\sum_{k=1}^{\nu}\sum_{n=1}^{N} U_{kn} \sum_{m=1}^{N} U_{km} \int_{\Omega} (W\nabla\phi_n)^{\mathrm{T}} \nabla\phi_m \, d\mathbf{x}, \tag{4.31}$$

$$\text{where} \quad \xi(\mathbf{x}; \{\mathbf{U}_n\}_{n=1}^N) = \mathbf{x} + \sum_{n=1}^{N} \mathbf{U}_n \phi_n(\mathbf{x}). \tag{4.32}$$

The corresponding modified expressions for the forces and weights are given as:

$$\boldsymbol{\psi}(\mathbf{x}; \{\mathbf{U}_n\}_{n=1}^N, I_T, I) = -\frac{1}{2}\sum_{r=1}^{R} \log(p_r(I(\mathbf{x}))) \nabla I_{Tr}|_{\mathbf{x}=\xi(\mathbf{x};\{\mathbf{U}_n\}_{n=1}^N)},$$

$$\rho_n(\mathbf{x}) = \phi_n, \qquad n \in \{1, 2, \ldots, N\}. \tag{4.33}$$

However, if the compositional update is used in either the variational-like approach in step 7, Algorithm 2 or the demons-like approach in step 6, Algorithm 3, then the warped gradient of the region template $\nabla I_{Tr}|_{\mathbf{x}=\xi(\mathbf{x};\{\mathbf{U}_n\}_{n=1}^N)}$ in the force term in Eq. 4.33 has to be replaced with the gradient of the warped region template $\nabla I_{Tr}(\xi(\mathbf{x};\{\mathbf{U}_n\}_{n=1}^N))$. Finally, it should be noted that, when the demons-like minimization approach is used with the forward formulation, the nodal update field parameters $\{\delta\mathbf{U}_n^t\}_{n=1}$ have a slightly different interpretation compared to the inverse formulation case. Here, $\delta\mathbf{U}_n^t$ computed using Eq. 4.12 at a node P_n of the original mesh $\mathcal{M}$ corresponds to the negative of the weighted average of the region forces $\boldsymbol{\psi}(\mathbf{x};\{\mathbf{U}_n^t\}_{n=1}^N, I_T, I)$ at the pixels (voxels) in the image I that neighbor the respective node P_n of the original mesh $\mathcal{M}$.

4.3.3 Experiments

In this section, the proposed FEM-based method for template-based multi-region segmentation is evaluated on real medical images containing various anatomical structures of interest. Three sets of experiments have been performed. The first two sets of experiments correspond to the binary segmentation case, where a single anatomical structure of interest needs to be segmented from the image. Further, in these two experiments the best settings for the proposed FEM-based segmentation method were determined in the context of basis functions, inverse or forward formulations and the optimization schemes. After fixing these settings, in the last set of experiments the performance of the proposed FEM-based template-based segmentation method was evaluated in the case of multi-region segmentation. Here, two instances were considered: one where the anatomical structures of interest share a common boundary and the other where the structures have separate boundaries. In the following experiments, the templates were obtained from available manual segmentations of the corresponding anatomical structures. The region intensity statistics in the image were modeled using the Parzen probability density in all the experiments and a homogeneous isotropic diffusivity model $W(\mathbf{x}) = 1$ was used. Further, the FEM-based segmentation method was implemented using a multi-resolution pyramid with three levels.

Basis functions comparison

In this experiment, the segmentation of three different anatomical structures namely, liver, spleen, muscle from 2D abdominal CT images and the segmentation of the left ventricle (LV) from a 3D MRI image was considered. For the purpose of this experiment, the proposed FEM-based segmentation method was implemented using the forward formulation discussed in Section 4.3.2 and the demons-like minimization strategy in Algorithm 3 with a compositional update. Here, the results obtained using the Lagrange, B-spline and multi-linear basis parametrizations of the deformation field were compared. The Lagrange parametrization employed a non-uniform mesh that is well adapted to the contours of the regions of interest (ROI) defined in the template. The non-uniform mesh was generated using the image-adaptive strategy described in Section 3.4. In Table 4.4 and Figure 4.15

	Lagrange basis parametrization			B-spline basis parametrization			multi-linear basis parametrization			Level set Chan-Vese [33]
Case	**Jacc.**	**DOF**	**Time**	Jacc.	DOF	Time	Jacc.	DOF	Time	Jacc.
Liver	**93.32**	**942**	**0.14**	93.60	43008	16.75	90.53	172032	14.17	83.65
Spleen	**91.28**	**774**	**0.08**	91.39	43008	13.65	92.53	172032	13.87	87.28
Muscle	**89.59**	**3310**	**0.13**	91.15	43008	13.55	86.68	172032	11.29	60.67
LV (3D)	**80.87**	**7551**	**0.78**	81.38	229467	2411.84	81.04	935031	2859.36	27.29
Mean	**88.76**	**3144**	**0.28**	89.38	89623	613.95	87.70	362782	724.67	64.72
Std.	**5.48**	**3158**	**0.33**	5.45	93230	1198.60	5.06	381500	1423.13	27.60

Table 4.4: Comparative binary segmentation results obtained by the FEM-based template-based segmentation method using the forward formulation with the different basis functions. Here, the Jaccard overlap score (%), the number of degrees of freedom (DOF) and the computational time in seconds are reported.

the Jaccard scores and the visual segmentation results obtained using the three basis parametrizations on the four different images are shown respectively. In Table 4.4, the number of degrees of freedom (DOF) corresponding to each of these parametrizations was computed as twice the sum of the number of nodes used in the mesh at each multi-resolution level. The computational times reported in Table 4.4 correspond to the time taken for solving the set of linear equations in Eq. 4.17. Further, the results obtained using the classic level set based Chan-Vese segmentation method [33] are also shown in Table 4.4, Figure 4.15 and Figure 4.16. All the methods were initialized with same the template. Firstly, it can be clearly observed that the proposed FEM-based method outperforms the Chan-Vese segmentation method irrespective of the basis functions used for the parametrization of the deformation field. This is due to the fact that the proposed FEM-based method was successful in preserving the initial topology of the anatomical structures defined in the template. Whereas, the naive region based Chan-Vese segmentation method "leaked" into surrounding structures with overlapping intensities, disturbing the initial topology. Secondly, it can be seen that the use of a Lagrange basis parametrization leads to a significantly lower DOF ($1-2$ orders of magnitude) deformation model compared to the B-spline and multi-linear basis parametrizations. Consequently, the Lagrange basis parametrization also obtains the lowest computational times among all the three different basis parametrizations, while achieving Jaccard scores similar to the B-spline and multi-linear basis parametrizations.

Inverse versus forward formulation and optimization schemes comparison

The objective of this experiment is two fold. Firstly, to compare the performance of the inverse and forward formulations with each other. Secondly, to determine the best optimization strategy among the four possible strategies, namely, variational-like (see Algorithm 2) with an additive or compositional update and demons-like (see Algorithm 3) with an additive or compositional update. Based on the inference from the previous experiment, the Lagrange basis parametrization is chosen to implement the proposed FEM-based template-based segmentation in this experiment. Here, the

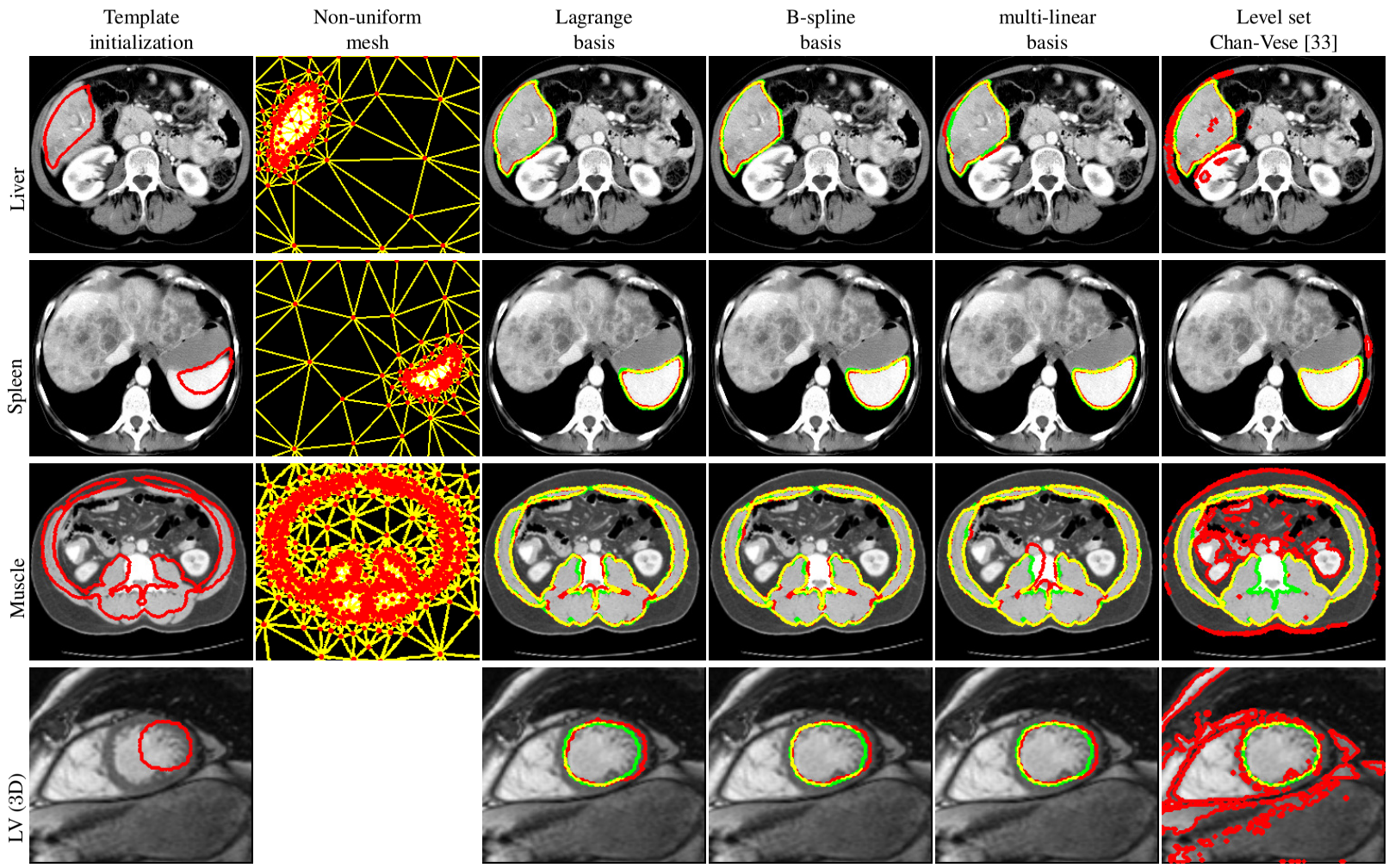

Figure 4.15: Visual segmentation results obtained by the FEM-based template-based segmentation method using the forward formulation comparing different basis functions. The segmentation result obtained using the Chan-Vese [33] segmentation method is also shown for comparison. Here, the estimated contours (red), the ground truth contours (green) and the overlap between them (yellow) are shown.

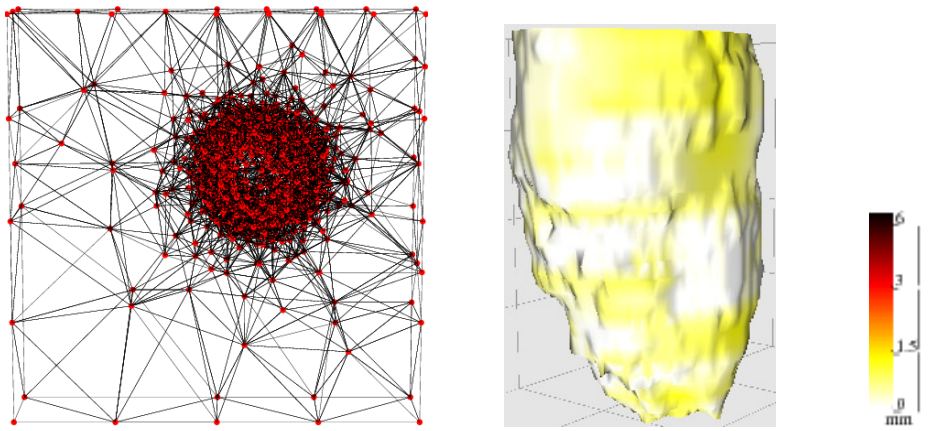

Non-uniform mesh | Lagrange result (3D rendering) | Color encoding

Figure 4.16: The 3D rendering of the segmentation surface obtained by the FEM-based template-based segmentation method using the Lagrange basis and the forward formulation in the left ventricle (LV) case. The color of the surface denotes the deviation between the estimated and ground truth segmentation surfaces. The deviation is computed as the Hausdorff distance between the two surfaces. The corresponding non-uniform mesh is also shown.

same set of images from the previous experiment are used for evaluation. In Table 4.5, the Jaccard scores and the computational times corresponding to the different implementations of the proposed FEM-based segmentation method are shown. In the forward formulation case, the computational times shown correspond to the time taken for solving the equations in Eq. 4.11 and Eq. 4.17, for the variational-like and demons-like minimization schemes respectively. However, in the inverse formulation case, the additional computational time incurred in the re-computation of the nodal basis functions on the deformed mesh at every iteration is also taken into account. It can be seen in Table 4.5 that the computational times for the inverse formulation case are considerably greater than the forward formulation as expected. Further, the variational-like minimization strategy with an additive update obtains the highest mean Jaccard score among all the optimization schemes in both the inverse and forward formulation cases.

Multi-region segmentation

In this experiment, the proposed method was implemented using the forward formulation with a Lagrange basis parametrization and the variational-additive optimization scheme and was tested on real medical images with multiple anatomical structures of interest. Here, a combined segmentation of the cerebral white matter (WM) along with the ventricle and cerebral white matter along with the brain stem from 2D brain MRI images was performed. The corresponding visual segmentation results and the Jaccard scores are shown in Figure 4.17. It can be seen that the cerebral white matter and the ventricle share a common boundary, whereas the brain stem has separate boundaries from the cerebral white matter. In both cases, the proposed method achieves good segmentation results.

	demons additive scheme				demons compositional scheme				**variational additive scheme**				variational compositional scheme			
	Forward formulation		Inverse formulation		Forward formulation		Inverse formulation		**Forward formulation**		**Inverse formulation**		Forward formulation		Inverse formulation	
Case	Jacc.	Time	Jacc.	Time	Jacc.	Time	Jacc.	Time	**Jacc.**	**Time**	**Jacc.**	**Time**	Jacc.	Time	Jacc.	Time
Liver	90.17	0.05	90.42	7.60	93.32	0.12	92.92	7.45	**93.31**	**0.16**	**93.25**	**7.60**	93.14	0.12	92.31	7.67
Spleen	91.93	0.08	93.43	7.47	91.28	0.15	89.51	7.40	**92.66**	**0.13**	**92.41**	**7.49**	92.46	0.16	91.57	7.44
Muscle	86.45	0.13	83.50	9.06	89.59	0.13	85.59	8.88	**86.97**	**0.20**	**86.66**	**9.10**	86.74	0.25	86.71	9.10
LV (3D)	75.18	0.72	51.55	127	80.87	0.67	63.69	117	**82.19**	**0.69**	**77.39**	**117**	80.11	0.80	71.37	114
Mean	85.93	0.25	79.73	38	88.76	0.27	82.93	35	**88.78**	**0.30**	**87.43**	**35**	88.11	0.33	85.49	35
Std.	7.52	0.32	19.24	59	5.48	0.27	13.17	55	**5.24**	**0.26**	**7.31**	**54**	6.06	0.32	9.73	53

Table 4.5: Comparative results obtained by the FEM-based template-based segmentation method using the forward and inverse formulations with the Lagrange basis parametrization and using different optimization schemes. Here, the Jaccard overlap score (%), the computational time in seconds are reported.

4.4 Discussion

This chapter presented an elaborate unified theoretical framework for image registration and segmentation using the less explored finite element method (FEM) and the non-uniform discretization of the problem domain. In addition, algorithms have also been developed for the practical implementation of the proposed FEM-based registration and segmentation methods. The experimental analysis in this chapter focused on tuning the proposed FEM-based registration and segmentation methods. Based on this analysis, the general conclusion was that the Lagrange basis parametrization along with an variational-like minimization strategy was the best choice for the FEM-based proposed registration and segmentation methods.

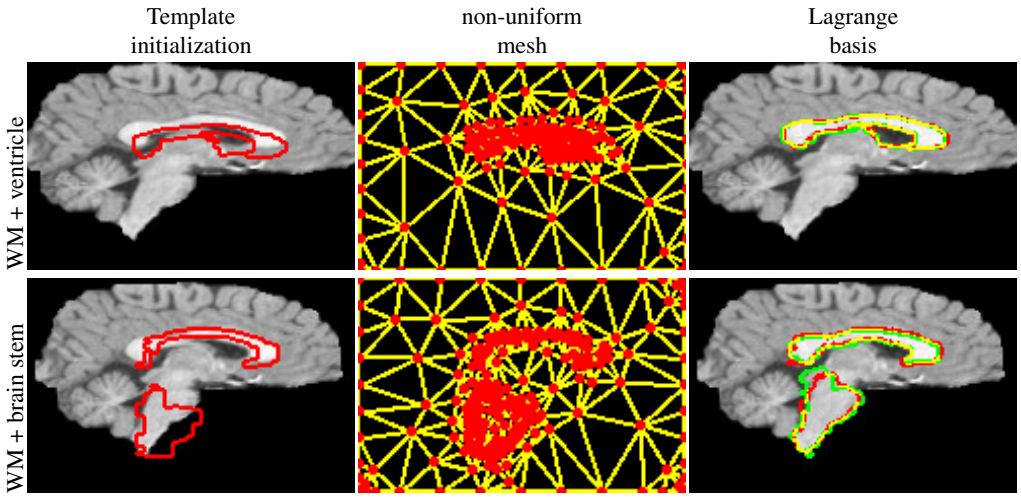

	Region 1	Region 2
Case	Jacc.	Jacc.
WM (1) + Ventricle (2)	83.36	79.31
WM (1) + Brain stem (2)	73.40	74.71
Mean	78.38	77.01
Std.	7.04	3.25

Figure 4.17: Multi-region segmentation results obtained by the FEM-based template-based segmentation method using the forward formulation with the Lagrange basis parametrization and variational-additive optimization scheme. Here, the Jaccard overlap score (%) is reported.

Chapter 5

FEM-based variational discrete deformable registration

This chapter introduces a new discrete deformable registration method that counts as one of the main contributions of this thesis. The primary novelty of the proposed method is in the variational formulation of the discrete deformable registration task, which entails the minimization of a convex energy functional involving diffusion-based regularization. It is shown that a finite difference method (FDM) based solution of the variational formulation is equivalent to a continuous-valued Gaussian Markov random field (MRF) energy minimization formulation previously proposed as the random walker (RW) based discrete registration method [28]. However, in this chapter, a more computationally efficient discrete deformable registration methodology is devised through the integration of the variational formulation into the unified FEM-based minimization framework developed earlier in Section 4.

5.1 Introduction

Most of the existing works on deformable registration estimate the unknown deformation field between the template and source images through the continuous optimization of energy functionals, as discussed in Section 2.1. Alternatively, there has been some interest towards formulating the deformable registration task as a discrete labeling problem. The basic idea in this approach is to discretize the space of possible deformations and minimize a Markov random field (MRF) energy corresponding to the deformable registration objective. As the MRF energy minimization is NP-hard in general, graph cuts [115] and linear programming [45] optimization methods have been explored for finding good quality approximate solutions to the MRF-based discrete deformable registration problem. A common feature among these discrete registration formulations was that, they were inherently discrete in both the spatial image domain and the space of possible deformations. In this chapter, a formulation that keeps the spatial image domain continuous is sought, resulting in a variational formulation for discrete deformable registration. The proposed formulation results in a

convex functional which can be conveniently minimized to obtain a unique solution. Specifically, a continuous prior probability map is associated with each of the possible deformation values using image similarities. The prior probability maps denote how likely the corresponding deformation value is at a particular spatial location in the continuous image domain. The discrete deformable registration task is then posed as a variational problem corresponding to the diffusion-based smoothing of prior probability maps. For solving this variational problem, the FEM method is used along with the Lagrange nodal basis functions defined on a non-uniform mesh well adapted to the salient image features. This significantly reduces the number of degrees of freedom (DOF) involved in the minimization compared to conventional uniform mesh based finite difference method (FDM) and therefore results in a highly computationally efficient solution. Moreover, it is shown that the FDM-based solution to the variational formulation is equivalent to the random walker (RW) based discrete registration method recently proposed by Cobzas et *al.* [28].

The closest related works to the proposed FEM-based discrete registration method are the above mentioned MRF-based discrete registration methods [115], [45]. Similar to these MRF-based methods, the proposed method also determines the unknown deformation field using a quantized search space of possible deformation values. However, in contrast to the MRF-based methods, the deformation field is not directly estimated through the minimization of a formal registration energy. Instead, the desired deformation field is constructed by pooling the solutions obtained from a set of convex energy minimization problems. These convex minimizations correspond to the smoothing of prior probability maps using a diffusion-based regularizer. Finally, it should be noted that, in the proposed FEM-based discrete registration method, the Lagrange nodal basis functions are only used to parametrize unknown smooth probability maps and not the deformation field. This is a major difference from the earlier proposed FEM-based continuous registration method in Section 4.2 and also from the other FEM-based parametric registration methods [40], [56], [89] discussed in Section 2.1.2, which use the Lagrange basis functions for the interpolation of the deformation field.

Formally, consider a source image $I_S : \Omega_S \rightarrow \mathbb{R}$, $\Omega_S \subset \mathbb{R}^\nu$ to be registered to a template image $I_T : \Omega_T \rightarrow \mathbb{R}$, $\Omega_T \subset \mathbb{R}^\nu$, $\nu = 2$ or 3 and the unknown deformation field $\mathbf{U} : \Omega_T \rightarrow \mathbb{R}^\nu$ to be estimated between the source and template images. In a discrete approach to deformable registration, the space of possible deformations is discretized or quantized such that it corresponds to a finite set of K vectors, i.e., $\mathbf{U} : \Omega_T \rightarrow \mathcal{D}$, where $\mathcal{D} = \{\mathbf{d}^k\}_{k=1}^K$, $\mathbf{d}^k \in \mathbb{R}^\nu$. In the following sections, three different approaches for discrete deformable registration are discussed:

- **Discrete-valued Markov random field**: The traditional discrete registration approach based on the Markov random field (MRF) is presented in Section 5.2. This formulation employs a uniformly discretized image domain along with a set of discrete-valued variables to represent the unknown deformation values at the respective discrete spatial locations.

- **Continuous-valued MRF or random walker (RW)**: The random walker (RW) based discrete deformable registration method proposed by Cobzas et *al.* [28] is described in Sec-

tion 5.3. This method follows a convex Gaussian MRF energy formulation, where a set of continuous-valued variables are used to denote the unknown deformations at spatial locations on a uniformly discretized image domain.

- **Variational formulation**: The proposed novel variational formulation of discrete registration on a spatially continuous image domain is introduced in Section 5.4. This involves the minimization of a convex energy functional that corresponds to diffusion-based smoothing. It is shown that a FDM-based solution to this variation problem is exactly equivalent to the Gaussian MRF-based or RW-based discrete registration. However, here a more computationally efficient solution to the variational formulation of discrete registration is proposed by employing the unified FEM-based minimization framework developed earlier in Chapter 4.

5.2 Discrete-valued MRF-based discrete registration

Let $\mathcal{G} = (\{\mathbf{x}_i\}_{i=1}^P, \mathcal{N})$ be a uniform discretization of the template image domain Ω_T, where $\{\mathbf{x}_i\}_{i=1}^P$ is the set of pixels (voxels) and $\mathcal{N}$ denotes the pixel (voxel) neighborhood. Now, consider a set of discrete-valued variables $\{L_i\}_{i=1}^P$, $L_i \in \{1, 2, \ldots, K\}$ such that $L_i = k$ corresponds to the unknown deformation field value $\mathbf{U}(\mathbf{x}_i) = \mathbf{d}^k \in \mathcal{D}$ at the pixel (voxel) $\mathbf{x}_i$. Here, $\mathcal{D} = \{\mathbf{d}^k\}_{k=1}^K$ is the space of all possible deformations. The discrete deformable registration task can be formulated as a finding the optimal values of the discrete-valued variables $\{L_i^*\}_{i=1}^P$ at the pixels (voxels) $\{\mathbf{x}_i\}_{i=1}^P$, through the minimization of the following discrete-valued MRF energy:

$$\mathbf{L}^* = \underset{\mathbf{L}\in\{1,2,\ldots,K\}^P}{\operatorname{argmin}} \sum_{i=1}^{P} A_i(L_i; I_T, I_S) + \gamma \sum_{i=1}^{P} \sum_{j\in\mathcal{N}(i)} V_{ij}(L_i, L_j), \tag{5.1}$$

where $\mathbf{L} = [L_i]_{i=1}^P$, $\mathbf{L}^* = [L_i^*]_{i=1}^P$ and γ is the regularization constant. The terms $A_i(L_i; I_T, I_S)$ and $V_{ij}(L_i, L_j)$ can be interpreted as the pixel-wise (voxel-wise) data and regularization terms respectively. They are commonly chosen as the squared difference similarity measure and the squared Euclidean distance measure respectively [115], [45]:

$$\begin{aligned} A_i(L_i = k; I_T, I_S) &= \Psi(\mathbf{x}_i; \mathbf{d}^k, I_T, I_S) = (I_S(\mathbf{x}_i + \mathbf{d}^k) - I_T(\mathbf{x}_i))^2, \\ V_{ij}(L_i = k, L_j = r) &= ||\mathbf{d}^k - \mathbf{d}^r||^2. \end{aligned} \tag{5.2}$$

In previous work, the discrete-valued MRF energy in Eq. 5.1 was minimized using the popular graph cuts technique in [115] or using the linear programming method [45]. The estimated optimal deformation field value at each of the pixels (voxels) $\{\mathbf{x}_i\}_{i=1}^P$ is obtained as $\mathbf{U}(\mathbf{x}_i) = \mathbf{d}^k$, where $L_i^* = k$.

5.3 Continuous-valued MRF or random walker (RW) based discrete registration

Recently in [28], the above discussed standard discrete-valued MRF based registration approach was modified to formulate a discrete deformable registration method based on the random walker (RW) with priors algorithm [47]. The key idea in this method was to relax the set of unknown discrete-valued variables $\{L_i\}_{i=1}^{P}$ to a set of continuous-valued variables $\{L_i^k\}_{i=1,k=1}^{P,K}$, such that $L_i^k \in \mathbb{R}$ denotes the unknown probability of the pixel (voxel) $\mathbf{x}_i$ having the deformation field value $\mathbf{U}(\mathbf{x}_i) = \mathbf{d}^k$. Then, following the RW with priors framework [47], the so-called pixel-wise (voxel-wise) prior probabilities $\{\lambda_i^k\}_{i=1,k=1}^{P,K}$ are defined using the squared difference similarity measure Ψ (see Eq. 5.2) as:

$$\lambda_i^k = \exp(-\beta\Psi(\mathbf{x}_i; \mathbf{d}^k, I_T, I_S)). \tag{5.3}$$

In the above, it can be noted that the pixel-wise (voxel-wise) prior λ_i^k essentially encodes the belief that the deformation value $\mathbf{d}^k$ is more likely at a pixel (voxel) $\mathbf{x}_i$, when the similarity measure between the warped source image and the template image at the pixel (voxel) $\mathbf{x}_i$ is small. The discrete deformable registration task can be re-formulated as the minimization of a continuous-valued Gaussian MRF energy (as opposed to the discrete-valued MRF energy in Eq. 5.1) given by:

$$\mathbf{L}^* = \underset{\mathbf{L}\in\mathbb{R}^{KP}}{\operatorname{argmin}} \sum_{i=1}^{P} A_i(\mathbf{L}_i; I_T, I_S) + \gamma \sum_{i=1}^{P} \sum_{j\in\mathcal{N}(i)} V_{ij}(\mathbf{L}_i, \mathbf{L}_j), \tag{5.4}$$

where $\mathbf{L} = [\mathbf{L}_i]_{i=1}^{P}$, $\mathbf{L}_i = [L_i^k]_{k=1}^{K}$, $\mathbf{L}^* = [\mathbf{L}_i^*]_{i=1}^{P}$, $\mathbf{L}_i^* = [L_i^{*k}]_{k=1}^{K}$ and γ is the regularization constant. Here, the data term $A_i(\mathbf{L}_i; I_T, I_S)$ is defined using the pixel-wise (voxel-wise) priors $\{\lambda_i^k\}_{i=1,k=1}^{P,K}$and the regularization term $V_{ij}(\mathbf{L}_i, \mathbf{L}_j)$ is chosen again using the RW framework [47] as:

$$\begin{aligned} A_i(\mathbf{L}_i; I_T, I_S) &= \sum_{k=1}^{K} \sum_{m\neq k} \lambda_i^m (L_i^k)^2 + \lambda_i^k (1 - L_i^k)^2, \\ V_{ij}(\mathbf{L}_i, \mathbf{L}_j) &= \sum_{k=1}^{K} w_{ij} (L_i^k - L_j^k)^2, \end{aligned} \tag{5.5}$$

where $w_{ij} = \exp(-\varrho(I_T(\mathbf{x}_i) - I_T(\mathbf{x}_j))^2)$ are image dependent edge weights. It can be seen that the data term encourages a high probability L_i^k for the deformation value $\mathbf{d}^k$ at the pixel (voxel) $\mathbf{x}_i$ when the pixel-wise (voxel-wise) prior λ_i^k is large at that pixel (voxel) $\mathbf{x}_i$. Whereas, the regularization term encourages the neighboring pixels (voxels) with similar intensity values in the template image I_T to have a similar probability distribution over the deformation values. Further, it can be seen that unlike the standard discrete-valued MRF energy in Eq. 5.1, the continuous-valued Gaussian MRF energy in Eq. 5.4 does not correspond to a formal registration energy. Consequently, minimization of the Gaussian MRF energy in Eq. 5.4 does not directly yield the unknown deformation field. Instead, at

first the optimal probabilities $\mathbf{L}^*$ are obtained through the minimization of the energy in Eq. 5.4 and then the unknown deformation field is constructed using these optimal probabilities.

A desirable aspect of the Gaussian MRF energy in Eq. 5.4 is that it is convex and thus has a unique minimum. In order to find this unique minimum, the energy in Eq. 5.4 is first compactly re-written as:

$$\mathbf{L}^* = \underset{\mathbf{L}\in\mathbb{R}^{KP}}{\operatorname{argmin}} \sum_{k=1}^{K}\sum_{m\neq k}^{K} \mathbf{L}^{k\mathrm{T}}\Lambda^m\mathbf{L}^k + (1-\mathbf{L}^k)^{\mathrm{T}}\Lambda^k(1-\mathbf{L}^k) + \gamma(\mathbf{L}^{k\mathrm{T}}\triangle_{\mathcal{G}}\mathbf{L}^k), \tag{5.6}$$

where $\Lambda^k = \mathrm{diag}(\boldsymbol{\lambda}^k)$, $\boldsymbol{\lambda}^k = [\lambda_i^k]_{i=1}^P$, $\mathbf{L}^k = [L_i^k]_{i=1}^P$ and $\triangle_{\mathcal{G}}$ is the discrete mesh Laplacian defined on the uniform mesh $\mathcal{G}$ as:

$$(\triangle_{\mathcal{G}})_{ij} = \begin{cases} \sum\limits_{r\in\mathcal{N}(i)} w_{ir} & \text{if } i=j \\ -w_{ij} & \text{if } j\in\mathcal{N}(i) \\ 0 & \text{otherwise} \end{cases}. \tag{5.7}$$

The unique minimum is found by setting the gradient of Eq. 5.6 with respect to each of $\{\mathbf{L}^k\}_{k=1}^K$ to zero. This leads to the following set of P linear equations for each $k \in \{1, 2, \ldots, K\}$ as:

$$\left(\sum_{m=1}^{K}\Lambda^m + \gamma\triangle_{\mathcal{G}}\right)\mathbf{L}^k = \boldsymbol{\lambda}^k. \tag{5.8}$$

Then, the optimal probabilities $\mathbf{L}^* = [\mathbf{L}_i^*]_{i=1}^P$, $\mathbf{L}_i^* = [L_i^{*k}]_{k=1}^K$ at the pixels (voxels) $\{\mathbf{x}_i\}_{i=1}^P$ are found by solving the above K systems of P linear equations. Now, the estimated deformation field value at each pixel (voxel) $\{\mathbf{x}_i\}_{i=1}^P$ is obtained as follows:

$$\mathbf{U}(\mathbf{x}_i) = \mathbf{d}^k, \tag{5.9}$$
$$\text{where} \quad k = \underset{r\in\{1,2,\ldots,K\}}{\operatorname{argmax}} L_i^{*r}.$$

However, it should be noted that even though the above deformation field is constructed from the optimal probabilities $\mathbf{L}^*$, this estimated deformation field by itself does not necessarily minimize any formal registration energy.

5.4 Variational formulation of discrete deformable registration

A major drawback in the random walker (RW) based discrete deformable registration method [28] discussed in the previous section is the use of a uniform mesh $\mathcal{G}$ for spatial discretization. As emphasized before in Section 4.2, the use of a uniform discretization is inefficient in the case of deformable registration. This is because, it leads to the computation of the deformation field with the same accuracy in every region of the domain, while it is desirable to be able to compute the deformation field with variable accuracy in different regions of the domain depending on the density of salient image features. Therefore, we propose the use of a non-uniform mesh and the FEM method to devise a new discrete deformable registration method. The proposed method borrows the

idea of deformation value priors from the RW-based discrete registration method [28] discussed in Section 5.3. To begin with, consider the following variational energy minimization problem defined on the unknown spatially continuous probability maps $L^k : \Omega_T \rightarrow \mathbb{R}$ corresponding to each of the deformation values $\mathbf{d}^k \in \mathcal{D}$:

$$\mathbf{L}^* = \underset{\mathbf{L}}{\operatorname{argmin}}\ E_D[\mathbf{L}; I_T, I_S, \mathcal{D}] + \gamma E_R^{\text{diff}}[\mathbf{L}], \tag{5.10}$$

$$\text{with} \quad E_D[\mathbf{L}; I_T, I_S, \mathcal{D}] = \frac{1}{2}\int_{\Omega_T} ||\mathbf{L}(\mathbf{x}) - \bar{\boldsymbol{\lambda}}(\mathbf{x}; \mathcal{D})||^2 \, d\mathbf{x},$$

$$E_R^{\text{diff}}[\mathbf{L}] = \frac{1}{2}\sum_{k=1}^{K}\int_{\Omega_T} \nabla L^{k\text{T}}(\mathbf{x}) W(\mathbf{x}) \nabla L^k(\mathbf{x}) \, d\mathbf{x},$$

where $\mathbf{L} = [L^k]_{k=1}^K$, $\mathbf{L}^* = [L^{*k}]_{k=1}^K$ and γ is a regularization constant. Further, $\bar{\boldsymbol{\lambda}} = [\bar{\lambda}^k]_{k=1}^K$, $\bar{\lambda}^k : \Omega_T \rightarrow [0\,1]$ are the normalized prior probability maps corresponding to each of the deformation values $\mathbf{d}^k \in \mathcal{D}$ defined as follows:

$$\bar{\lambda}^k(\mathbf{x}; \mathbf{d}^k) = \frac{\lambda^k(\mathbf{x}; \mathbf{d}^k)}{\sum_{r=1}^{K} \lambda^r(\mathbf{x}; \mathbf{d}^r)}, \tag{5.11}$$

$$\text{with} \quad \lambda^k(\mathbf{x}; \mathbf{d}^k) = \exp(-\beta \Psi(\mathbf{x}; \mathbf{d}^k, I_T, I_S)),$$

where Ψ is the squared difference similarity measure defined in Eq. 5.2. The above energy minimization formulation in Eq. 5.10 essentially corresponds to the anisotropic diffusion-based smoothing of the normalized prior probability maps $\{\bar{\lambda}^k\}_{k=1}^K$. In other words, the minimization attempts to find a smooth probability map L^k associated with the deformation value $\mathbf{d}^k$ such that it is as "close" as possible to the corresponding normalized prior probability map $\bar{\lambda}^k$. The smoothness is enforced through the anisotropic diffusion-based regularization term E_R^{diff}, where W is a $\nu \times \nu$ symmetric matrix denoting the diffusivity or the stiffness field. Note that, in the above there is no need for an explicit constraint to make sure that the unknown probability maps $\{L^k\}_{k=1}^K$ sum to 1. This because the unique minimizer of Eq. 5.10 should naturally satisfy this constraint, as the normalized prior probability maps $\{\bar{\lambda}^k\}_{k=1}^K$ were defined such that they sum to 1 (like in [47]). The estimated deformation field $\mathbf{U}(\mathbf{x})$ at a spatial location $\mathbf{x} \in \Omega_T$ is obtained by choosing the deformation value $\mathbf{d}^k$ with the highest optimal probability at that spatial location:

$$\mathbf{U}(\mathbf{x}) = \mathbf{d}^k \qquad \forall\, \mathbf{x} \in \Omega_T, \tag{5.12}$$

$$\text{where} \quad k = \underset{r \in \{1,2,\ldots,K\}}{\operatorname{argmax}}\ L^{*r}(\mathbf{x}).$$

5.4.1 Equivalence to random walker (RW) based discrete registration

We claim that the variational formulation of discrete registration in Eq. 5.10 is equivalent to the continuous-valued Gaussian MRF energy minimization formulation in Eq. 5.4 referred to as the random walker (RW) based discrete registration method [28]. This can be easily proved by considering the Euler-Lagrange equations corresponding to the energy functional in Eq. 5.10 for each

$k \in \{1, 2, \ldots, K\}$:

$$\nabla_{L^k}(E_D + \gamma E_R^{\text{diff}}) = (L^k - \bar{\lambda}^k) - \gamma\nabla(W\nabla L^k) = 0. \tag{5.13}$$

Rearranging we get for each $k \in \{1, 2, \ldots, K\}$:

$$L^k - \gamma\nabla(W\nabla L^k) = \bar{\lambda}^k. \tag{5.14}$$

Multiplying both sides by $\sum_{r=1}^{K} \lambda^r$ and setting the arbitary regularization constant $\gamma \equiv \left(\sum_{r=1}^{K} \lambda^r\right)\gamma$ we get for each $k \in \{1, 2, \ldots, K\}$:

$$\left(\sum_{r=1}^{K} \lambda^r\right) L^k - \gamma\nabla(W\nabla L^k) = \lambda^k. \tag{5.15}$$

Now, choosing a diffusivity $W(\mathbf{x}) = \exp(-\varrho(\text{diag}(\nabla I_T))^2))$, it is easy to observe that a FDM discretization (on the uniform grid $\mathcal{G}$) of the Euler-Lagrange equations in Eq. 5.15 corresponds to the set of linear equations in Eq. 5.8 that arise from the minimization of the continuous-valued Gaussian MRF-based discrete registration problem in Eq. 5.4. Hence, the equivalence between the proposed variational formulation of discrete registration and the RW-based discrete registration method [28] is established.

5.4.2 FEM-based solution for variational discrete registration

We present a computationally efficient solution to the proposed variational formulation of discrete registration in Eq. 5.10 using the FEM method. In this regard, it can be clearly seen that the data term E_D in Eq. 5.10 is essentially of the same form as the data term in Eq. 4.1 corresponding to the unified FEM-based minimization framework proposed in Section 4.1. Note that, the diffusion-based regularization term E_R^{diff} is of course the same. Therefore, the variational problem in Eq. 5.10 can be solved using the unified FEM-based energy minimization framework. Accordingly, based on Eq. 4.2, the finite element approximation of the probability map $\mathbf{L}$ over the non-uniform mesh $\mathcal{M} = (\{P_n\}_{n=1}^N, \triangle_h)$ using the Lagrange nodal basis functions $\{\phi_n\}_{n=1}^N$ in Eq. 3.7 can be written as:

$$\mathbf{L} = \sum_{n=1}^{N} \mathbf{L}_n \phi_n(\mathbf{x}; \mathcal{M}), \qquad \mathbf{x} \in \Omega_T, \tag{5.16}$$

where $\mathbf{L}_n = \mathbf{L}(P_n)$ represents the value of the probability map at node P_n of the non-uniform mesh $\mathcal{M}$. Using the above, the finite dimensional approximation of the data term E_D in Eq. 5.10 is obtained as:

$$E_D(\{\mathbf{L}_n\}_{n=1}^N; I_T, I_S, \mathcal{D}) = \frac{1}{2}\int_{\Omega_T} ||\sum_{n=1}^{N} \mathbf{L}_n \phi_n(\mathbf{x}) - \bar{\boldsymbol{\lambda}}(\mathbf{x}; \mathcal{D})||^2 \, d\mathbf{x}, \tag{5.17}$$

Thus, following the unified FEM-based minimization framework in Section 4.1, the goal of the variational formulation of discrete registration is to find the optimal nodal probability map parameters

$\{\mathbf{L}_n^*\}_{n=1}^N$ such that the data term E_D is minimized while ensuring the smoothness of the deformation field using the diffusion-based regularization term E_R^{diff}. However, as the data term E_D in Eq. 5.17 is *convex*, the iterative demons-like scheme in Algorithm 3, Section 4.1.2 becomes redundant and hence only the variational-like scheme in Algorithm 2, Section 4.1.1 is relevant in this case. Further, as the data term E_D in Eq. 5.17 is not only convex but also *quadratic* in terms of $\{\mathbf{L}_n\}_{n=1}^N$, the set of equations in Eq. 4.6 resulting from the variation-like scheme are linear. This is in contrast to the continuous deformable registration and template-based segmentation cases discussed in Section 4.2 and Section 4.3 respectively, where a set of non-linear equations arise. The forces $\boldsymbol{\psi}(\mathbf{x}; \{\mathbf{L}_n\}_{n=1}^N, I_T, I_S)$ and weights $\{\rho_n(\mathbf{x})\}_{n=1}^N$ corresponding to the data term in Eq. 5.17 are given as:

$$\begin{aligned} \boldsymbol{\psi}(\mathbf{x}; \{\mathbf{L}_n\}_{n=1}^N, I_T, I_S) &= \sum_{n=1}^{N} \mathbf{L}_n \phi_n(\mathbf{x}) - \bar{\boldsymbol{\lambda}}(\mathbf{x}; \mathcal{D}), \\ \rho_n(\mathbf{x}) &= \phi_n(\mathbf{x}), \qquad\qquad n \in \{1, 2, \ldots, N\}. \end{aligned} \tag{5.18}$$

After the system of linear equations in Eq. 4.6 is solved to obtain the optimal nodal probabilities $\{\mathbf{L}_n^*\}_{n=1}^N$, $\mathbf{L}_n^* = [L_n^{*k}]_{k=1}^K$, the optimal probabilities $\mathbf{L}^*(\mathbf{x}) = [L^{*k}(\mathbf{x})]_{k=1}^K$ at any spatial location $\mathbf{x} \in \Omega_T$ can found through interpolation of the optimal nodal probabilities $\{\mathbf{L}_n^*\}_{n=1}^N$ based on the finite element approximation in Eq. 5.16. Then, the estimated deformation field $\mathbf{U}(\mathbf{x})$ at $\mathbf{x} \in \Omega_T$ is obtained by choosing the deformation value $\mathbf{d}^k$ with the highest optimal probability at that spatial location, i.e., $\mathbf{U}(\mathbf{x}) = \mathbf{d}^k$ where $k = \underset{r \in \{1,2,\ldots,K\}}{\operatorname{argmax}} L^{*r}(\mathbf{x})$.

5.5 Experiments

The proposed FEM-based variational discrete registration method was evaluated on real and synthetic medical images. The proposed FEM-based discrete method was implemented in a multi-resolution framework with 4 levels. The range of deformations used in each of the 4 levels were as follows: $[0, \pm 0.125, \ldots, \pm 0.5]^\nu$, $[0, \pm 0.25, \ldots, \pm 1.0]^\nu$, $[0, \pm 0.5\, , \ldots, \pm 1.5]^\nu$, $[0, \pm 1.0]^\nu$, where $\nu = 2$ or 3. Further, $\beta = 1.0$ was fixed. In the following, two experiments were performed. The goal of the first experiment was to determine the right type of diffusivity to be used with the proposed FEM-based discrete registration method. After the diffusivity model was chosen, in the second experiment the proposed FEM-based discrete registration method was compared with the random walker (RW) based discrete registration method [28]. In the experiments below, the 2D synthetic MRI, the 3D real CT and the 3D real MRI data sets previously described in Section 4.2.3 were considered (see Figure 4.6 and Figure 4.7). Again, in order to ensure reasonable completion times of the experiments, only the synthetic 2D synthetic MRI data set was used in the RW-based registration comparison experiment . However, all the three data sets were used for the initial diffusivity model comparison experiment. The image-adaptive meshing strategy described in Section 3.4 was used to generate the non-uniform mesh on the template image. The proposed method was coded in MAT-

	Source before regis.			homogeneuous isotropic diffusivity				**Perona-Malik isotropic diffusivity**				Nagel anisotropic diffusivity			
	Synth. 2D	CT 3D	MRI 3D	Synth. 2D		CT 3D	MRI 3D	**Synth. 2D**		**CT 3D**	**MRI 3D**	Synth. 2D		CT 3D	MRI 3D
Case	SSDE	TRE	Jacc.	SSDE	AAE	TRE	Jacc.	**SSDE**	**AAE**	**TRE**	**Jacc.**	SSDE	AAE	TRE	Jacc.
1	5589.95	3.89	35.81	270.73	15.88	1.34	50.95	**223.49**	**13.67**	**1.40**	**51.12**	206.12	13.27	1.50	51.32
2	4599.06	4.34	47.18	142.89	6.55	1.41	55.02	**130.08**	**6.92**	**1.48**	**55.46**	132.38	7.10	1.72	54.21
3	5681.54	6.94	41.46	76.33	5.62	2.28	51.73	**72.04**	**6.41**	**2.31**	**51.72**	73.88	6.66	2.35	51.44
4	4582.57	9.83	38.68	98.87	8.43	2.67	53.81	**88.30**	**8.22**	**2.75**	**53.97**	94.87	8.99	3.03	53.93
5	5678.33	7.48	32.60	77.94	4.84	2.76	53.24	**73.36**	**4.80**	**2.52**	**53.63**	77.52	5.61	2.72	53.50
Mean	5226.29	6.50	39.15	133.35	8.26	2.09	52.95	**117.45**	**8.00**	**2.09**	**53.18**	116.95	8.33	2.27	52.88
Std.	581.30	4.83	13.73	81.35	4.47	2.24	9.44	**63.76**	**3.39**	**2.33**	**9.63**	54.97	3.02	2.53	9.76

Table 5.1: Comparative results obtained by the FEM-based variational discrete registration method with the different diffusivity models on the synthetic 2D MRI (with $\gamma = 5$), the real 3D MRI (with $\gamma = 20$) and the real 3D CT (with $\gamma = 10$) datasets. Here, the sum of squared differences error (SSDE), average angular error (AAE) in degrees, Jaccard overlap score (%) and the target registration error (TRE) in millimeters are reported.

LAB using the MEX facility. All the experiments below were run on an Intel i7 3.60 GHz machine with 64GB RAM.

5.5.1 Diffusivity models comparison

The first model considered was the simple homogeneous isotropic diffusivity. Next, the Perona-Malik diffusivity [82] which was inhomogeneous but still isotropic was chosen. Lastly, the Nagel diffusivity [76] which was not only inhomogeneous but also anisotropic was considered. The implementations using the different diffusivity models were tested on the three data sets mentioned earlier. On the 2D synthetic MRI data set the registration accuracy was evaluated using the sum of squared differences error (SSDE) and the average angular error (AAE) measures. In order to evaluate the registration accuracy on the 3D MRI data set, the 56 manual anatomical labels defined in the source image were mapped onto the template using the estimated deformation field. The Jaccard overlap measure was computed between the warped source labels and the template labels. For the 3D real CT data set, registration accuracy was evaluated by propagating the 300 manual landmark positions in the inhale phase image to the exhale phase image using the estimated deformation fields. The target registration error (TRE) measure was computed between the warped and the actual landmark locations. The TRE measure is the Euclidean distance in millimeters (mm). In Table 5.1 the registration results corresponding to the three different diffusivity models are shown and a sample visual result is shown in Figure 5.1 and Figure 5.2. It can be seen that the Perona-Malik inhomogeneous diffusivity performs considerably better that the basic homogeneous model on the 2D synthetic MRI and 3D real MRI data sets and obtains identical results on the 3D CT data set. Further, it can be observed that the use of the more complex Nagel anisotropic diffusivity model does not improve the results. In fact a decrease in the registration accuracy is exhibited across all the three different data sets. Therefore, the Perona-Malik diffusivity is chosen for the implementation of the proposed

	Before regis.	**FEM-based variational discrete registration**				Random walker (RW) based discrete registration [28]			
No.	SSDE	**SSDE**	**AAE**	**DOF**	**Time**	SSDE	AAE	DOF	Time
1	5589.95	**223.49**	**13.67**	**12184**	**0.11**	156.75	13.80	331588	2.52
2	4599.06	**130.08**	**6.92**	**10624**	**0.07**	101.13	7.01	331588	2.58
3	5681.54	**72.04**	**6.41**	**11140**	**0.08**	57.42	5.60	331588	2.88
4	4582.57	**88.30**	**8.22**	**11276**	**0.12**	64.47	8.12	331588	2.84
5	5678.33	**73.36**	**4.80**	**11582**	**0.10**	58.91	4.59	331588	2.73
Mean	5226.29	**117.45**	**8.00**	**11361**	**0.10**	87.74	7.82	331588	2.71
Std.	581.30	**63.76**	**3.39**	**576**	**0.02**	42.53	3.60	0	0.16

Table 5.2: Comparison between the proposed FEM-based variational discrete registration method (with $\gamma = 5$) with the Perona-Malik diffusivity and the random walker (RW) based discrete registration method on the synthetic 2D MRI dataset. Here, the sum of squared intensity errors error (SSDE), average angular error (AAE) in degrees, computational times in seconds and the number of degrees of freedom (DOF) are reported.

FEM-based discrete registration method.

5.5.2 Comparison with random walker (RW) based discrete registration

In this section, the better performance of the proposed FEM-based variational discrete registration method compared to the random walker (RW) based discrete registration method [28] was empirically demonstrated. In Table 5.2, the comparative results obtained using the proposed FEM-based discrete registration method and the RW-based discrete registration method on the synthetic 2D MRI data set are shown. The FEM-based discrete registration method was implemented using the Perona-Malik diffusivity model. The RW-based registration method uses a uniform mesh, while the proposed FEM-based discrete registration method employs a non-uniform mesh well adapted to the image features. The number of DOF associated with a mesh was given as twice the number of nodes in the mesh. Further, the computational time reported in Table 5.2 corresponds to the time taken for solving the equation system in Eq. 4.6 for the proposed FEM-based discrete registration method and it corresponds to the time required to solve the equation system in Eq. 5.8 for the RW-based discrete registration method. Based on the low mean SSDE and AAE values, it can be inferred that, both the FEM-based discrete registration method and the RW-based discrete registration method were successful in recovering the ground truth deformation fields. Further, both the methods exhibit similar spatial distribution of registration accuracy as can be seen from the plots of the recovered deformation fields in Figure 5.3. However, the proposed FEM-based discrete registration method entailed a significantly lower computational effort ($\sim$ 30 times lower DOF and $\sim$ 30 times faster) when compared to the RW-based registration method.

The reader is referred to Chapter 6 for a more extensive evaluation of the proposed FEM-based discrete registration method in comparison to other popular deformable registration methods on benchmark medical image data sets.

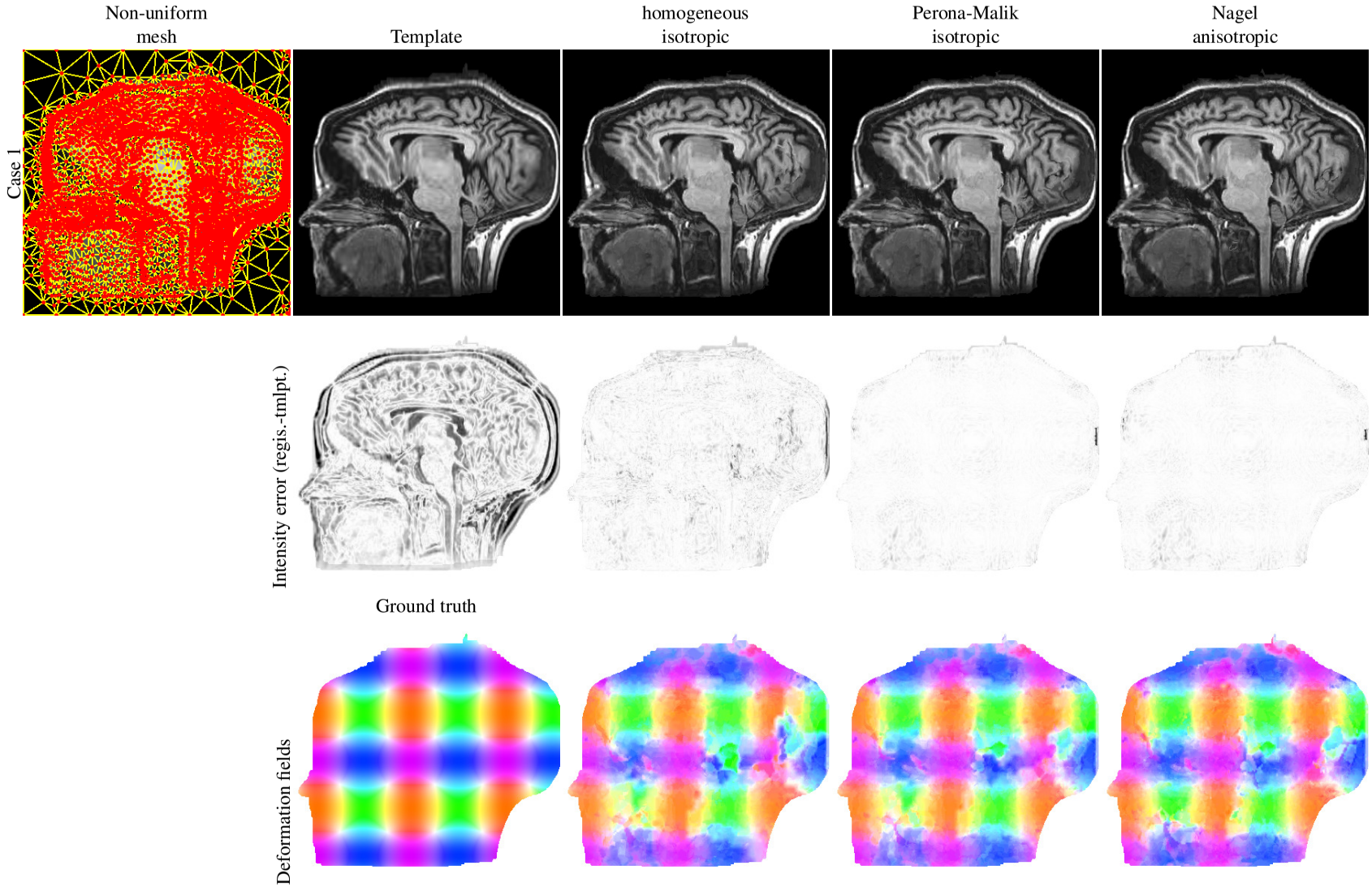

Figure 5.1: Visual comparative results obtained by the FEM-based variational discrete registration method with the different diffusivity models on the synthetic 2D MRI dataset (with $\gamma = 5$). Note that, in the intensity error (template-registered) images white means zero error and more dark the intensity implies more the error.

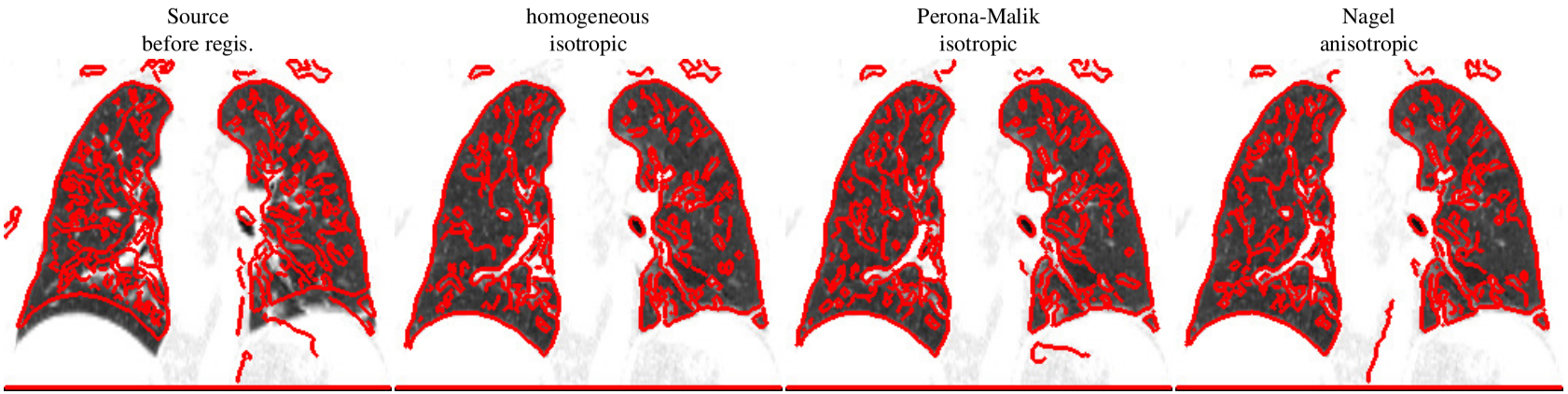

(a) 3D real CT image, Case 4 results. Here, contours of the original source image and the warped source image are overlayed on template image (a 2D slice was chosen).

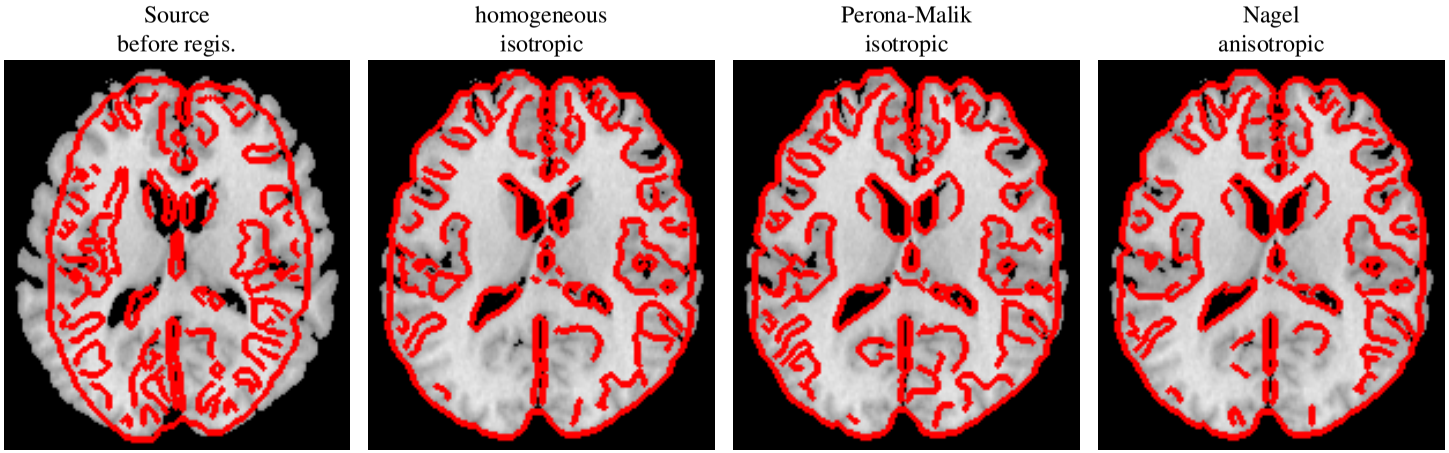

(b) 3D real MRI image, Case 5 results. Here, contours of the original source image and the warped source image contours are overlayed on template image (a 2D slice was chosen).

Figure 5.2: Visual comparative results obtained by the FEM-based variational discrete registration method with the different diffusivity models on the synthetic 2D MRI dataset the real 3D brain MRI dataset (with $\gamma = 20$) and the real 3D CT lung dataset (with $\gamma = 10$).

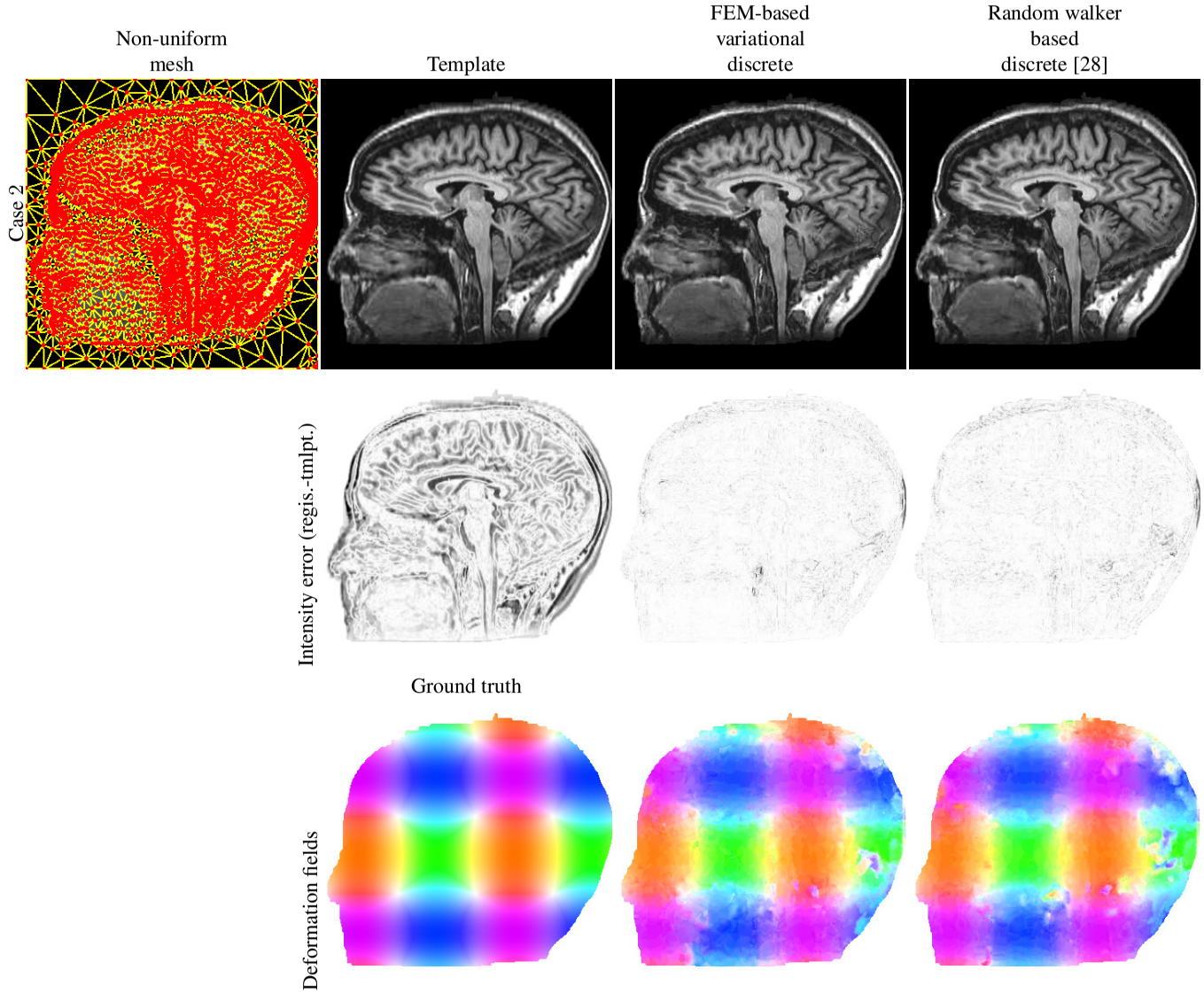

Figure 5.3: Visual comparative registration results between the FEM-based variational discrete registration method and the random walker (RW) based registration method. Note that, in the intensity error (template-registered) images white means zero error and more dark the intensity implies more the error.

5.6 Discussion

We developed a computationally efficient FEM-based discrete deformable registration method using the squared differences similarity measure and diffusion-based regularization. A salient aspect of the proposed method was the use of an image-adaptive discretization of the problem domain. This resulted in the proposed method being multiple orders of magnitude faster than the existing random walker (RW) based discrete registration method that was implemented using a uniform mesh.

There is a definite scope to improve the proposed FEM-based variational discrete registration method. In the future, the following aspects require further investigation:

- A drawback of the proposed method is that the estimated deformation field is not diffeomorphic. This is mainly due to the fact that the deformation field is not explicitly regularized and the regularization is only implicit through the smoothing of prior probability maps. An obvious solution would be to explore the use of an additional regularization step that would yield diffeomorphic deformation fields. Another promising idea is to employ an incremental approach, where small diffeomorphic steps taken at each iteration are composed together to obtain the final diffeomorphic deformation field.

- In this work, the squared differences similarity measure was considered, which is only useful for mono-modality registration tasks. A desirable extension would be the use of more complex similarity measures for multi-modality registration. As the proposed method does not involve taking gradient of the similarity measure, the incorporation of any other similarity measures into our method would be straightforward.

- Interesting insights are gained by drawing a parallel between our proposed method and the optic flow methods using the block matching algorithm (BMA) [43], [139]. Firstly, like our proposed method, the BMA-based optic flow methods also use a discrete space of possible deformation values. Furthermore, akin to our proposed method the BMA-based optic flow methods do not minimize a formal global energy for the deformation field estimation. Instead, they perform a brute-force search to find the deformation value that leads to the highest similarity map value (computed over block neighborhood) at each spatial location. However, as opposed to the BMA-based optic flow methods, our proposed method employs smoothed similarity maps obtained through diffusion-based regularization that implicitly lead to smooth deformation fields. In light of these observations the applicability of our proposed method for the computation of optic flow between images can be examined.

Chapter 6

Comparison with popular registration methods on benchmark datasets

In this chapter, the utility of the proposed FEM-based continuous and discrete deformable registration methods for practical medical image registration tasks is evaluated using benchmark datasets. The FEM-based continuous registration method (FEM-CONT) was developed in Section 4.2 and the FEM-based discrete registration method (FEM-DISC) was introduced in Section 5.4. Here, both the proposed methods were tested on two publicly available datasets; the POPI-model chest 4D CT dataset [120] that has a set of manually annotated landmarks available and the CUMC12 brain MRI database [1] that has various anatomical regions labeled by an expert.

The following settings were used in the implementation of the FEM-CONT and FEM-DISC registration methods:

- **FEM-CONT**: The Lagrange basis parametrization was employed along with the variational-like minimization strategy with an additive update. A multi-resolution strategy with 4 levels was chosen. The Perona-Malik diffusivity model [82] was chosen. The regularization parameter was fixed as $\gamma = 0.1$. The non-uniform mesh generated using the procedure described in Section 3.4.

- **FEM-DISC**: The Perona-Malik diffusivity model [82] was used and $\beta = 1.0$ was set. The regularization parameters were chosen as $\gamma = 10$ and $\gamma = 200$ for evaluation on the POPI-model and CUMC12 datasets respectively. The FEM-DISC method used a multi-resolution pyramid with 4 levels. The range of deformations used in each of the 4 levels were as follows: $[0, \pm 0.125, \ldots, \pm 0.5]^3$, $[0, \pm 0.25, \ldots, \pm 1.0]^3$, $[0, \pm 0.5\ , \ldots, \pm 1.5]^3$, $[0, \pm 1.0]^3$. Again, the non-uniform mesh generation strategy in Section 3.4 was followed.

The FEM-CONT and FEM-DISC methods were coded in MATLAB using the MEX facility. All the experiments were run on an Intel i7 3.50 GHz machine with 32GB RAM.

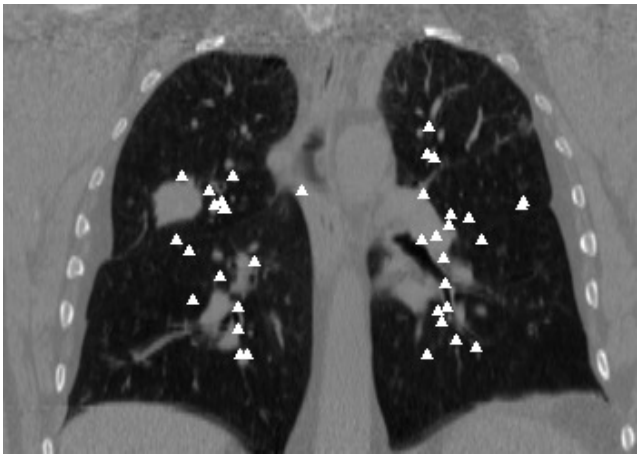

Figure 6.1: A coronal 2D slice of the end-inhalation phase image (which is used as the template) from the POPI-model 4D dataset is shown with the projected manually annotated landmarks.

6.1 Validation on the POPI-model chest 4D CT dataset

The POPI-model chest 4D CT dataset [120] consisted of ten 3D CT volumes representing ten different phases of one breathing cycle. Each of the volumes had been acquired at resolution of $360 \times 482 \times 141$ with a voxel spacing of 0.98mm $\times$ 0.98mm $\times$ 2.0mm. Further, in the lung region of these ten breathing phases, 37 manually annotated corresponding landmarks were provided (see Figure 6.1). The image corresponding to the end-inhalation phase of the breathing cycle was chosen as the template and the remaining 9 breathing phase images were registered to it using the FEM-CONT and FEM-DISC registration methods respectively. The overall computational time for each registration using the FEM-CONT method was 28 minutes from which 7 minutes were taken for solving the equation system in Eq. 4.11. For the FEM-DISC registration method, the overall run-time for each registration was about 18 minutes of which 3 minutes were taken for solving the equation system in Eq. 4.6. In order to evaluate the registration accuracy, the landmark positions in the template image was propagated to the other breathing phase images using the estimated deformation fields. The target registration error (TRE) measure was computed between the warped and the actual landmark locations. The TRE measure is the Euclidean distance in millimeters (mm). In Table 6.1, the mean and standard deviation of the TREs obtained by the FEM-CONT and FEM-DISC methods over all the phases and landmarks is shown. In addition, the mean of the upper 10% quantile (MU10) statistic, which is more robust to outliers than the maximum value is also reported. Kabus et *al.* [57] reported the mean, standard deviation and MU10 of the TREs obtained by 6 other existing deformable registration methods on the POPI-model dataset. Further, sample visual results obtained by FEM-CONT and FEM-DISC are shown in Figure 6.2. It can be seen that the FEM-CONT and FEM-DISC registration methods rank 3^{rd} and 7^{th} among the 8 methods listed in Table 6.1 based on the mean TRE values.

Method	TRE
before registration	3.68 ± 2.97 (9.6)
elsatix [63]	0.96 ± 0.56 (2.1)
DROP [45]	0.98 ± 0.56 (2.2)
FEIR [57]	1.05 ± 0.57 (2.2)
FEM-CONT	$\mathbf{1.05 \pm 0.58}$ $\mathbf{(2.3)}$
POPI-par [34]	1.07 ± 0.56 (2.2)
MBS [124]	1.11 ± 0.65 (2.5)
FEM-DISC	$\mathbf{1.13 \pm 0.74}$ $\mathbf{(2.7)}$
POPI-nonpar [103]	1.28 ± 0.42 (2.1)

Table 6.1: Results on the POPI-model lung 4D CT dataset. Target registration errors (TREs) for the various deformable registration methods. Except for the FEM-CONT and FEM-DISC registration methods, the results corresponding to all the other methods were taken from Kabus et *al.* [57]. Here, the mean $\pm$ standard deviation (MU10) of the TREs over all phases and landmarks are reported.

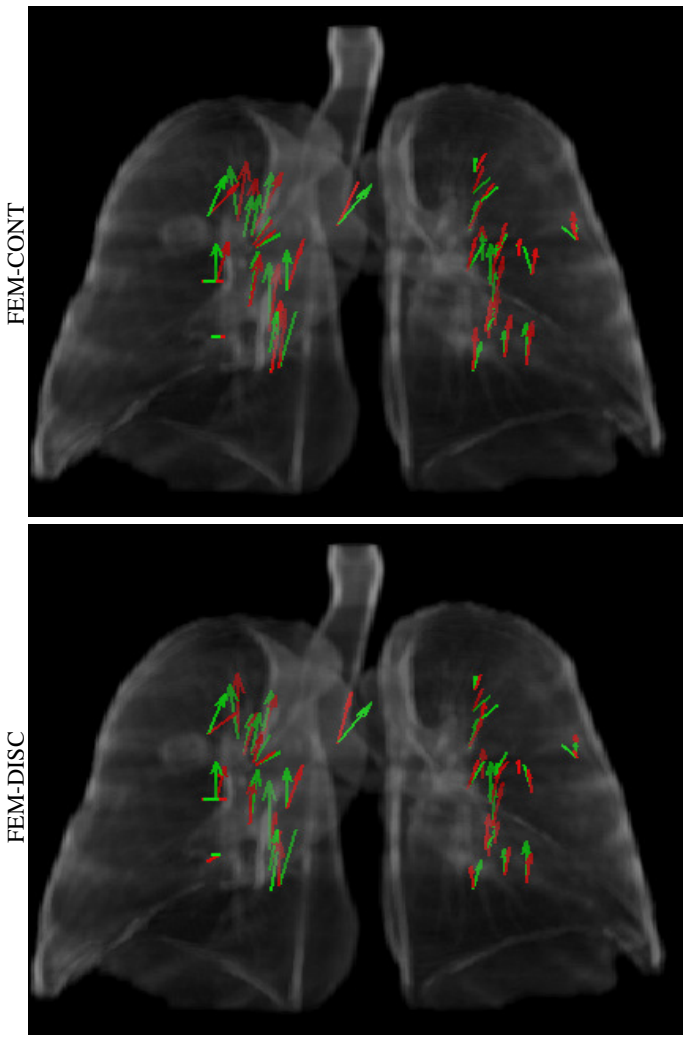

Figure 6.2: A sample visual result (for the 4^{th} breathing phase) on the POPI-model lung 4D CT dataset. Here, the estimated (red) and actual (green) deformation vectors at each of the landmark points are depicted.

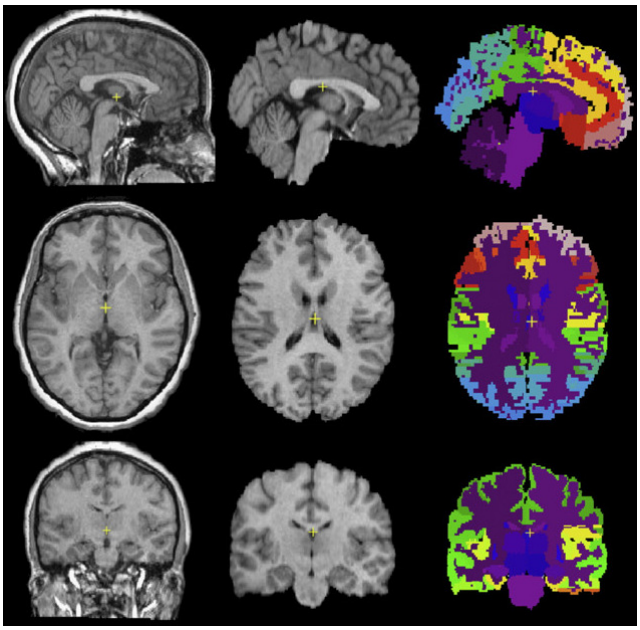

Figure 6.3: The axial, saggital and coronal 2D slices of a sample brain from the CUMC12 dataset are shown with the various manually labeled anatomical regions (image was taken from Klein et *al.* [62]).

6.2 Validation on the CUMC12 MRI database

The CUMC12 dataset [1] consisted of 3D brain MRI scans from 12 subjects (6 male and 6 female) taken at $256 \times 256 \times 124$ resolution with a $0.86\text{mm} \times 0.86\text{mm} \times 1.5\text{mm}$ voxel spacing. Manual segmentations of 128 anatomical regions were provided for each of these images (see Figure 6.3). These images were first aligned with a MNI152 atlas ($181 \times 217 \times 181$ resolution and $1.0\text{mm} \times 1.0\text{mm} \times 1.0\text{mm}$ voxel spacing) [46] using a 9-parameter linear registration. Then, $12 \times 12 - 12 = 132$ pair-wise registrations were performed between the images using the proposed FEM-CONT and FEM-DISC registration methods respectively. The overall computational time for each registration using the FEM-CONT method was 19 minutes from which 11 minutes were taken for solving the equation system in Eq. 4.11. For the FEM-DISC registration method, the overall run-time for each registration was about 10 minutes of which 4 minutes were taken for solving the equation system in Eq. 4.6. For evaluating registration accuracy, anatomical labels on the source image were mapped to the template using the estimated deformation field. The Jaccard overlap measure was computed between the warped source labels and the template labels. In Figure 6.4, the Jaccard scores obtained by averaged over 128 anatomical regions and 132 pair-wise registrations using the proposed FEM-CONT and FEM-DISC methods is reported. Klein et *al.* [62] reported average Jaccard scores obtained by 14 popular deformable registration methods on the CUMC12 dataset. It can be seen that the FEM-CONT and FEM-DISC methods rank 4^{th} and 6^{th} among the 16 methods listed in Figure 6.4. Further, sample visual results obtained by FEM-CONT and FEM-DISC are shown in

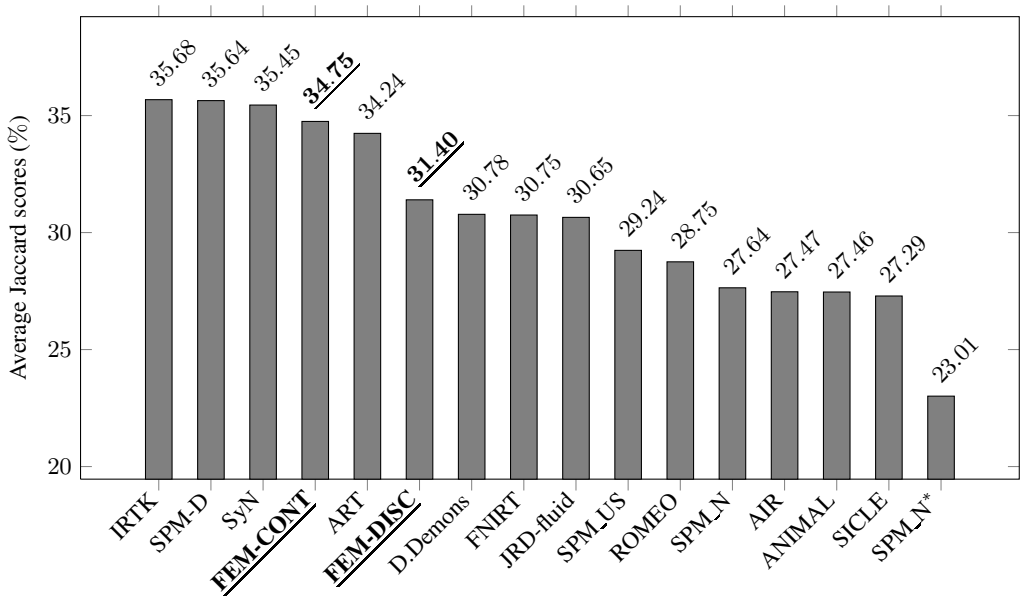

Figure 6.4: Results on the CUMC12 MRI brain database. Average Jaccard scores (over 132 pairwise registrations and 128 anatomical regions) for the various deformable registration methods are shown. Except for the proposed FEM-CONT and FEM-DISC registration methods the results corresponding to all the other methods were taken from Klein et *al.* [62].

Figure 6.5.

6.3 Discussion

The proposed FEM-CONT and FEM-DISC methods were demonstrated to be practically useful for real world medical image registration tasks based on the feasible computation times and good registration accuracies reported in Section 6.1 and Section 6.2. Even though the FEM-DISC method was faster than the FEM-CONT method, the FEM-CONT method achieved significantly greater registration accuracies. In fact, the performance of the FEM-CONT method was close to the top ranking registration methods in both the POPI-4D and CUMC12 cases. In summary, the FEM-CONT method can be readily employed for practical medical image registration tasks, whereas further research needs to done to improve the registration accuracies obtained using the FEM-DISC method.

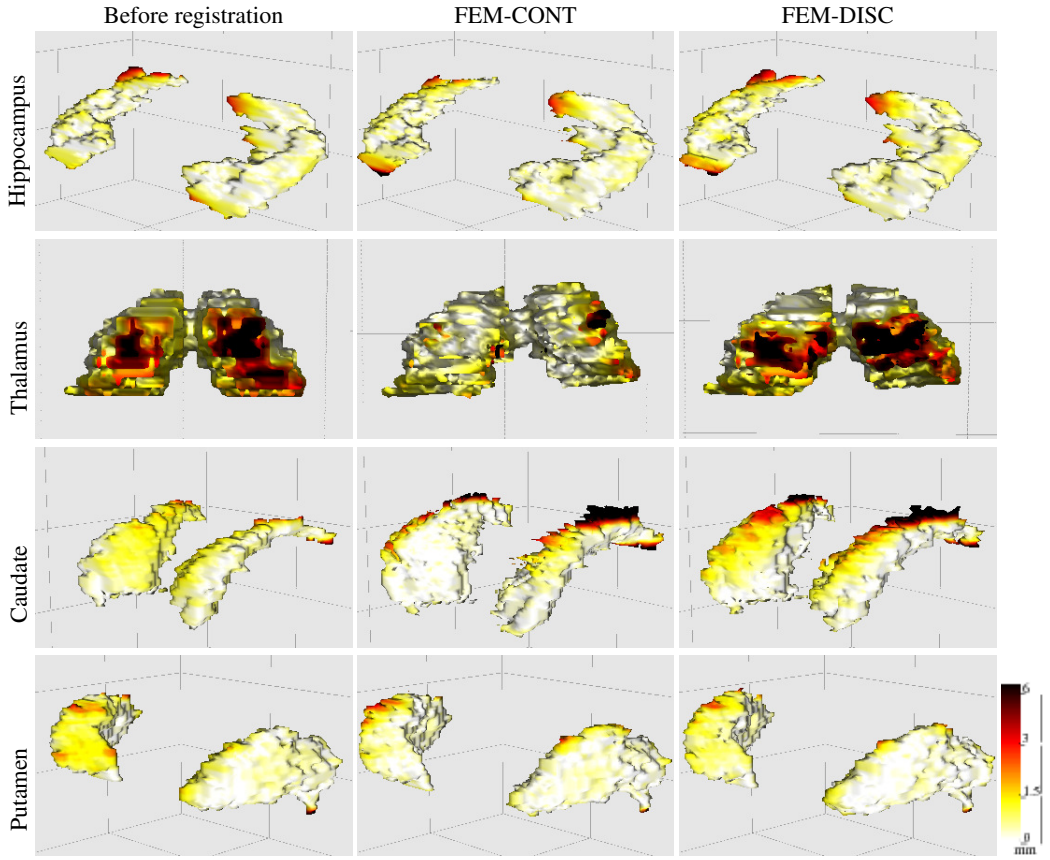

Figure 6.5: A sample visual result (registration of patient 7 to patient 9) on the CUMC12 MRI brain database using the FEM-CONT and FEM-DISC registration methods. Here, the segmentation surfaces corresponding to 4 different subcortical structures (hippocampus, thalamus, caudate and putamen) mapped from the source image onto the template image before and after registration are shown. The color denotes the deviation between the warped source segmentation surface and the template segmentation surface. The deviation is computed as the Hausdorff distance between the two surfaces.

Chapter 7

FEM-based segmentation of muscle and fat tissues from thoracic CT images

In this chapter, a particular medical imaging application of the unified FEM-based image registration and segmentation framework introduced earlier in Chapter 4 is presented. A completely automatic segmentation pipeline is developed for the estimation of muscle and fat tissue proportions from thoracic computed tomography (CT) images. The novel aspect of the proposed segmentation methodology is the use of a statistical deformation model (SDM) to incorporate a priori shape knowledge learned from training data into the unified FEM-based registration and segmentation framework. Further, a study of the relationship between the patient survival data and the cross-sectional area estimates of muscle tissue computed using the proposed automatic segmentation framework is also presented.

7.1 Introduction

Body composition, i.e., the proportion of fat and muscle tissues in the human body is related to the risk factors associated with a host of medical conditions such as growth failure in children, obesity, cachexia syndromes (in chronic disease of lung, liver, heart or kidney), malnutrition, lipodystropy, metabolic syndrome and frailty. In particular, body composition has important implications for cancer patients. It has been found that the presence of a relatively high body fat content makes the patients more vulnerable to the onset or recurrence of several types of cancers. On the other hand, sarcopenia, a wasting syndrome which involves the loss of muscle tissues has been correlated with poor response to chemotherapy treatment and reduction in overall survival of the patients. The muscle and fat tissues are target locations for the water- and fat-soluble drugs respectively used for cancer treatment. Consequently, the proportions of these tissues are believed to determine the chemotherapy toxicity and efficacy. Similarly, in patients suffering from diabetes, body composition has been linked with metabolic alteration such as insulin resistance. Therefore, it is of considerable

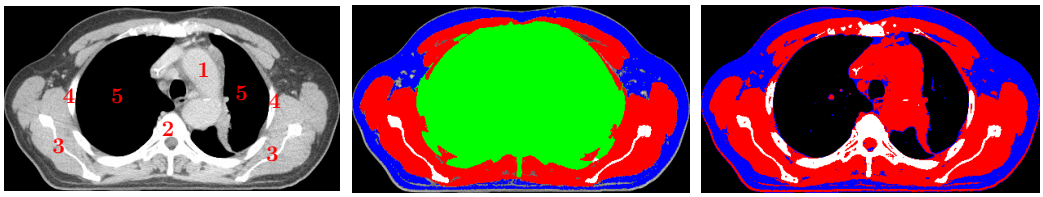

(a) Original CT (b) Manual segmentation (c) Thresholded segmentation

Figure 7.1: Illustration of the challenges in thoracic CT segmentation. (a) 1 denotes the heart, 2 denotes the T4 vertebra, 3 denotes scapula (shoulder blades), 4 denotes ribs and 5 denotes lungs. (b)-(c) Muscle tissue (red), fat tissue (blue) and thoracic cavity (green). It can be seen that segmentation solely based on thresholding the muscle and fat HU ranges results in a lot of errors due to the significant overlap of intensities between the muscle tissues and neighboring organs in the thoracic cavity.

interest to understand the complex relationships between body composition and the various health ailments.

Revolutionary advances in body composition research were brought about by the introduction of computed tomography (CT) imaging technique, which has a very high precision and specificity for different tissues in the human body [10], [95]. In body composition studies using CT images, 2D cross-sectional images acquired at specific skeletal landmarks are commonly used instead of whole body 3D scans. This is because the proportion of muscle and fat tissues at these specific skeletal landmarks correlates well with the whole body muscle volume and the whole body fat volume [108], [73]. Further, this localized image acquisition also prevents the patients from unnecessary radiation exposure. In current practice, abdominal and thoracic 2D CT images taken at the 3rd lumbar vertebra (L3) and the 4th thoracic vertebra (T4) respectively have been widely used for body composition analysis [85], [86]. These studies rely on the manual segmentation of muscle and fat tissue regions from CT images using pre-defined windows of Hounsfeld units (HU, units of radiation attenuation) for each tissue. However, the manual segmentation of large databases of CT images used in these studies is not practical and hence automatic segmentation methods are needed.

The segmentation of the fat region from CT images using automatic methods [137], [138] is relatively straightforward due to the unique HU range of the fat tissue $[-190 \ -30]$. But, the automatic segmentation of the muscle region is quite challenging as there exists a significant overlap between the HU ranges of the muscle tissue $[-29 \ 150]$ and surrounding organs (see Figure 7.1). Very few works exist on muscle segmentation from CT images [58], [59]. Moreover, these works only consider the segmentation of a specific muscle group as opposed to the segmentation of the total muscle region captured in the image. Recently, Chung et *al.* [27] addressed the segmentation of whole muscle and fat regions from abdominal CT images with great success. In their work, the difficult step of segmenting the muscle region was achieved by taking advantage of the well defined muscle shape present in abdominal CT images using a shape prior based segmentation method. But, this approach cannot be used for the segmentation of muscle regions in thoracic CT images as in the

thoracic CT images the shape of the muscle does not conform to a specific class of shapes. However, in thoracic CT images, the thoracic cavity containing the lungs, ribs and other organs (see Figure 7.1) exhibits a consistent shape across the patient population, modulo the inter-patient variation and the variability in the manual identification of the T4 vertebrae. Hence, a priori shape knowledge about the thoracic cavity's shape can be used to disambiguate the muscle tissue from the other organs in the thoracic cavity that have overlapping intensities. Based on this idea, an automatic segmentation framework is proposed for thoracic CT images, where the thoracic cavity is first segmented using a shape prior model learned from training data and then the muscle and fat regions are obtained by thresholding the rest of the image using their respective HU ranges.

The proposed segmentation framework takes a template-based approach, where a binary template defining an initial shape is deformed via deformable registration to match the region of interest (ROI) in the input image. This corresponds to a template-based representation of the segmentation boundary as shown in Figure 2.4, where the desired segmentation boundary is implicitly defined by the contour of the initial shape and the deformation field estimated between the template and the input image. Existing works on template-based segmentation either use a non-parametric representation of the deformation field [102], [65] or parametrize the deformation field using B-spline basis functions [55], [67] on a uniform discretization of the image domain. As highlighted before in Section 4.3, the use of a uniform discretization is inefficient in the case of template-based segmentation. This is because, it leads to the computation of the deformation field with the same accuracy everywhere even though detailed deformations are only needed along the contours of the ROI. Therefore, in the proposed framework, following the FEM-based deformable registration methodology discussed in Section 4.2, the deformation field is efficiently parametrized using the Lagrange basis functions (see Eq. 3.3) on a non-uniform mesh well adapted to the contours of the initial shape in the template. Further, in order to better capture the shape variations of the thoracic cavity, a shape prior based on a statistical deformation model (SDM) is constructed from a set of training shapes which are encoded as deformations of a non-uniform mesh. The FEM-based deformable registration methodology is then extended using the SDM to perform a shape prior constrained segmentation of the thoracic cavity.

7.2 Related work

In this section, the relevant literature on the segmentation of muscle and/or fat tissues from medical images is briefly reviewed. Further, as the template-based shape modeling approach is used for image segmentation in this work, a short survey of the current works on statistical deformation model (SDM) based shape prior segmentation is also presented.

As mentioned before, owing to the distinct HU range of the fat tissues, CT images are a natural choice for the estimation of fat content in the human body [137], [138]. However, there have been efforts to delineate fat tissue regions from magnetic resonance images (MRI) as well, using user-

defined thresholds [48], [71] or automatic image-adaptive thresholding techniques [64], [74]. We note that these works additionally sub-segment the fat region into subcutaneous fat tissue (SFT) and visceral fat tissue (VFT) respectively.

The general focus of the existing works on muscle segmentation has been to extract a specific group of muscles from whole body CT or MRI scans using statistical shape models. Kamiya et *al.* devised a rule-based expert system for the segmentation of the psoas major [58] and rectus abdominis [59] muscles from CT images, where the muscle shape was approximated by a simple quadratic function. A more elaborate representation of the muscle shape can be considered through the use of a point distribution model (PDM) constructed from a set of training shapes with manually annotated landmark correspondences. Such PDMs have been employed for providing shape information during the Markov random field (MRF) based segmentation of the calf muscle [125] and the snake based segmentation of the quadratus lumborum muscle [37] from MRI images. Alternatively, in [5] an isometric log-ratio (ILR) space embedding of the muscle shape was employed for the segmentation of extensor and flexor muscles from MRI images via a convex energy minimization framework.

The popular approach for the construction of shape prior models has been to use the level set embedding functions (see Figure 2.4) for representing the shape of the region of interest (ROI) [66], [96], [118], [97], [32], [97]. Alternatively, Rueckert *et al.* [100] introduced the idea of using shape priors based on a statistical deformation model (SDM), where the general shape of the ROI is represented using a binary template image and then the shape variations are defined using a set of deformation fields which are obtained by the deformable registration of each of the binary training shapes to the template image. The two important choices in the construction of a SDM are the parametrization of the deformation field and the statistical model to compactly encode shape variations (given by the deformation fields) in the training data. Originally, Rueckert *et al.* [100] used the B-spline basis parametrization on a uniform mesh and employed the multivariate Gaussian probability density to model the mesh deformations in the training data. Such a B-spline based Gaussian SDM has been used for general shape prior constrained segmentation in [54]. In fact, the above mentioned work by Chung et *al.* [27] on muscle segmentation from abdominal images also uses the B-spline based Gaussian SDM approach. However, these works used the principal component analysis (PCA) to encode only the major modes of shape variations in the training data. Albrecht et *al.* [2] extended the Gaussian-PCA SDM to span a wider range of shape variations through the use of an augmented covariance matrix while employing a non-parametric representation of the deformation field. As an alternative to the simple Gaussian density, the more general Parzen or kernel density has been explored for the construction of a SDM using the B-spline parametrization [116]. More recently, Glocker et *al.* [44] proposed a MRF-based statistical modeling framework that takes advantage of the dependencies between the B-spline mesh deformations to obtain a more compact SDM without compromising its ability to capture the wide range of shape variations present in the training data.

In the proposed segmentation framework, as opposed to above discussed B-spline based SDMs [100], [54], [27], [116], [44], a SDM is constructed using the Lagrange basis parametrization of the deformation field on a non-uniform mesh . The nodal deformations of the non-uniform mesh obtained from the training data are compactly encoded following the augmented Gaussian-PCA approach proposed in [2].

7.3 Segmentation via FEM-based deformable registration with a Gaussian SDM

This section presents the theory behind the central aspect of the proposed CT image segmentation framework, which is the segmentation of the thoracic cavity using a SDM based shape prior.

7.3.1 FEM-based deformable registration

For the reader's convenience, we briefly review the description of the particular FEM-based deformable registration methodology proposed earlier in Section 4.2. Given input $I : \Omega \rightarrow \mathbb{R}$ and template $I_T : \Omega_T \rightarrow \mathbb{R}$ images, where $\Omega, \Omega_T \subset \mathbb{R}^\nu$, $\nu = 2$ or 3, the task of deformable registration is to find a dense deformation field $\mathbf{U} : \Omega_T \rightarrow \mathbb{R}^\nu$ such that the input image warped using the deformation field, $I(\mathbf{x} + \mathbf{U}(\mathbf{x}))$ is similar to the template image I_T. In a FEM-based framework, the deformation field $\mathbf{U}$ is approximated as a linear combination of a set of nodal basis functions $\{\phi_n\}_{n=1}^N$ on the uniform or non-uniform mesh $\mathcal{M}$:

$$\mathbf{U}(\mathbf{x}) = \sum_{n=1}^{N} \mathbf{U}_n \phi_n(\mathbf{x}; \mathcal{M}), \qquad \forall \mathbf{x} \in \Omega_T. \tag{7.1}$$

Following the variational-like approach discussed in Section 4.1.1, the deformable registration task is transformed into finding the unknown nodal deformation field parameters $\mathbf{\Theta} = [\mathbf{U}_n]_{n=1}^N \in \mathbb{R}^{N\nu}$ through the finite-dimensional multivariate minimization of an energy:

$$\mathbf{\Theta}^* = \underset{\mathbf{\Theta} \in \mathbb{R}^{N\nu}}{\operatorname{argmin}} \, E_D(\mathbf{\Theta}; I_T, I) + \gamma_R E_R^{\text{diff}}(\mathbf{\Theta}), \tag{7.2}$$

where γ_R is the regularization constant and the sum of squared differences (SSD) data term E_D in Eq. 4.20 and the diffusion-based regularization term in Eq. 4.3 are given as:

$$\begin{aligned} E_D(\mathbf{\Theta}; I_T, I) &= \frac{1}{2} \int_{\Omega_T} \left(I(\mathbf{x} + \sum_{n=1}^{N} \mathbf{U}_n \phi_n) - I_T(\mathbf{x}) \right)^2 d\mathbf{x}, \\ E_R^{\text{diff}}(\mathbf{\Theta}) &= \frac{1}{2} \sum_{k=1}^{\nu} \sum_{n=1}^{N} U_{kn} \sum_{m=1}^{N} U_{km} \int_{\Omega_T} \nabla \phi_n^{\mathrm{T}} \nabla \phi_m \, d\mathbf{x}, \end{aligned} \tag{7.3}$$

where $\mathbf{U}_n = [U_{kn}]_{k=1}^{\nu}$. Note that, in the above a homogeneous isotropic diffusivity model $W(\mathbf{x}) = 1.0$ has been assumed.

7.3.2 Segmentation via FEM-based registration

The above described FEM-based deformable registration methodology can be readily used for the template-based segmentation of binary input images $I : \Omega_T \rightarrow \{0, 1\}$ which are considered in the context of thoracic cavity segmentation from CT images (see Figure 7.3). For this purpose, a binary image $I_T : \Omega_T \rightarrow \{0, 1\}$ defining an initial shape of the region of interest (ROI) is chosen as the template. This template is then deformed through the energy minimization in Eq. 7.2 and the final segmentation label $I^* : \Omega \rightarrow \{0, 1\}$ is given by inverse warping the template using the optimal nodal deformation parameters $\mathbf{\Theta}^* = [\mathbf{U}_n^*]_{n=1}^N$ as:

$$I^*(\mathbf{x}) = I_T(\mathbf{x} - \sum_{n=1}^{N} \mathbf{U}_n^* \phi_n) \qquad \forall \mathbf{x} \in \Omega. \tag{7.4}$$

Different types of nodal basis functions, namely, the Lagrange, the cubic B-spline and the multi-linear basis functions described in Section 3.3 can be used for the parameterization of the deformation field in Eq. 7.1. However, in the proposed segmentation approach, the Lagrange basis functions which are defined on a non-uniform mesh well adapted to the contours of the ROI in the template are used. The computational advantage in using the Lagrange basis parametrization as opposed to the uniform mesh based B-spline and multi-linear basis parametrizations has been empirically demonstrated before in Section 4.2.3 and Section 4.3.3. Note that, the above described segmentation approach is only valid for binary input images. This is in contrast to the more general FEM-based template-based segmentation methodology discussed in Section 4.3 where a region-based data term was used instead of the SSD data term in Eq. 7.3.

7.3.3 Gaussian statistical deformation model

Assume that a set of M nodal deformation field parameters $\{\mathbf{\Theta}^{(m)} = [\mathbf{U}_n^{(m)}]_{n=1}^N\}_{m=1}^M$ are obtained by registering M training images $\{I^{(m)} : \Omega \rightarrow \mathbb{R}\}_{m=1}^M$ to a template image I_T, using the FEM-based deformable registration method. For introducing a priori shape knowledge into coming registration tasks, a statistical deformation model (SDM) is now constructed from these nodal deformation field parameters $\{\mathbf{\Theta}^{(m)}\}_{m=1}^M$. Following [2], the space of deformation parameters is modeled using a multivariate Gaussian density $\mathcal{N}(\overline{\mathbf{\Theta}}, \Sigma_{\mathbf{\Theta}})$, with a sample mean $\overline{\mathbf{\Theta}}$ and a $N\nu \times N\nu$ sample covariance matrix $\Sigma_{\mathbf{\Theta}}$. Further, the dominant modes of shape variation are computed using principal component analysis (PCA) and they are used to devise an additional shape-based regularization term as follows:

$$\begin{aligned}
&E_S^{\mathrm{PCA}}(\mathbf{\Theta}) = ||B\,(\mathbf{\Theta} - \overline{\mathbf{\Theta}})||^2 + \frac{1}{2(\varrho\sigma_0^2)}||\mathbf{\Theta} - \overline{\mathbf{\Theta}}||^2, \\
&B = \mathrm{diag}(\eta_1 \ldots \eta_K)[B_1 \ldots B_K]^{\mathrm{T}}, \\
&\underline{\Sigma}_{\mathbf{\Theta}} = (1 - \varrho)\Sigma_{\mathbf{\Theta}} + \varrho\sigma_0^2 \mathrm{Id}_{N\nu}, \\
&\eta_k^2 = ((1 - \varrho)\sigma_k^2 + \varrho\sigma_0^2)^{-1} - (\varrho\sigma_0^2)^{-1},
\end{aligned} \tag{7.5}$$

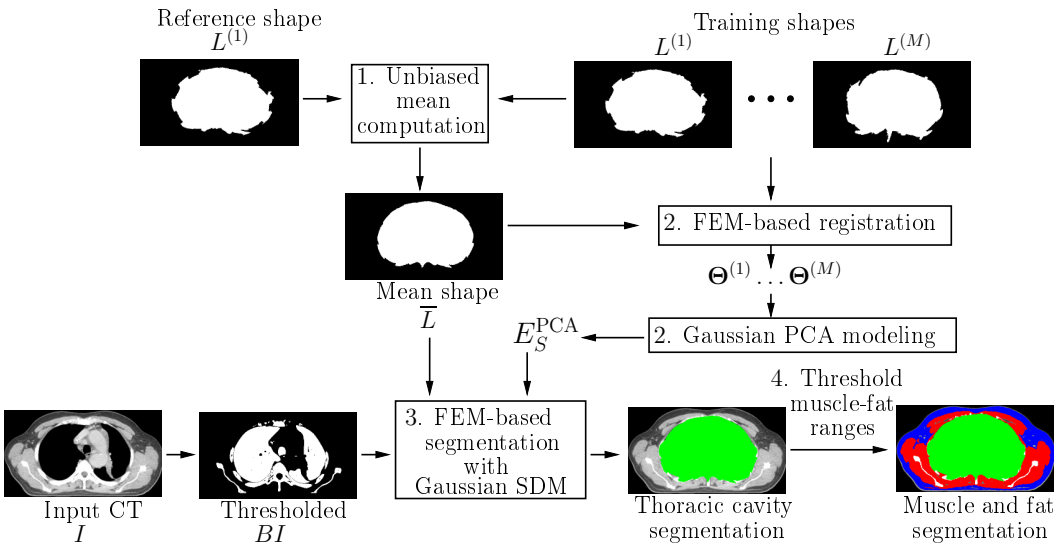

Figure 7.2: Overview of the proposed muscle and fat segmentation framework

where $\{B_k\}_{k=1}^{K}$ is the PCA basis corresponding to the augmented covariance matrix $\underline{\Sigma}_{\mathbf{\Theta}}$. Here, σ_k^2 are the eigen values of the matrix $\Sigma_{\mathbf{\Theta}}$ and ϱ, σ_0 are constants. The above regularizer can be seen as imposing a shape prior on the deformation fields by penalizing deviations from the Gaussian SDM as opposed to strictly restricting the deformation fields to the span of the PCA basis. Incorporating the shape-based regularizer into Eq. 7.2, the following statistically constrained FEM-based deformable registration formulation is obtained:

$$\mathbf{\Theta}^* = \underset{\mathbf{\Theta} \in \mathbb{R}^{N\nu}}{\operatorname{argmin}} E_D(\mathbf{\Theta}; I_T, I) + \gamma_R E_R^{\text{diff}}(\mathbf{\Theta}) + \gamma_S E_S^{\text{PCA}}(\mathbf{\Theta}), \tag{7.6}$$

where γ_R, γ_S are regularization constants. Here, it is more efficient to perform the energy minimization using an explicit line search based gradient-descent strategy as opposed to the semi-implicit scheme described in Algorithm 2, Section 4.1.1. This is because the gradient of the shape-based term $\nabla E_S^{\text{PCA}}(\mathbf{\Theta})$ yields a very large non-sparse system of equations at every iteration corresponding to step 6 in Algorithm 2, that would require a large computational time to solve. The line search based gradient descent strategy is given as:

$$\mathbf{\Theta}^{(k+1)} = \mathbf{\Theta}^{(k)} - \tau(\nabla E_D(\mathbf{\Theta}^{(k)}; I_T, I) + \gamma_R \nabla E_R^{\text{diff}}(\mathbf{\Theta}^{(k)}) + \gamma_S \nabla E_S^{\text{PCA}}(\mathbf{\Theta}^{(k)})), \tag{7.7}$$

where $\nabla \equiv \nabla_{\mathbf{\Theta}}$ and τ is the time step determined using line search.

7.4 Framework for automatic segmentation of muscle and fat tissues

The main idea of our segmentation framework is to first determine the thoracic cavity (see Figure 7.1b) in an input CT image through shape prior based segmentation using the FEM-based deformable registration with a Gaussian SDM presented in the section 7.3. Then, the muscle and fat

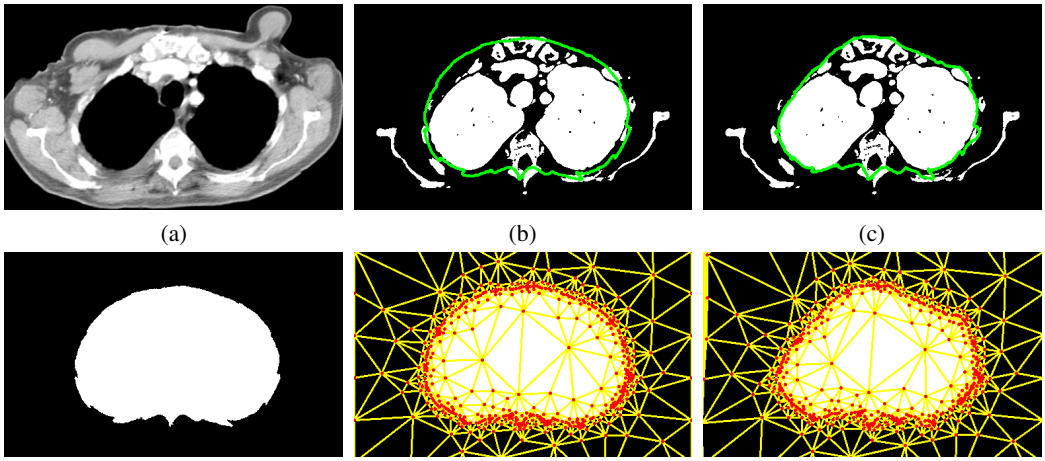

Figure 7.3: (a) Input image I (b) Thresholded input image BI initialized with mean shape $\overline{L}$ (green contour) (c) BI with final estimated thoracic cavity shape L^* (green contour) (d) Mean shape $\overline{L}$ (e) Initial FEM mesh on $\overline{L}$ (f) Deformed FEM mesh on estimated thoracic cavity shape L^*

regions are segmented by thresholding the points in the input CT image that do not belong to the thoracic cavity using the pre-defined HU ranges of muscle and fat tissues respectively. But, before these segmentation steps are performed, a shape prior of the thoracic cavity shape is constructed from training data which involves the computation of a mean shape and encoding the deviations from the mean shape using a Gaussian SDM. The proposed segmentation framework is depicted in Figure 7.2 and we describe its various components in detail below:

1. **Computation of thoracic cavity mean shape**: Given a training set of binary thoracic cavity shapes $\{L^{(m)} : \Omega \rightarrow \{0,1\}\}_{m=1}^{M}$, the backward approach [49] for mean shape computation is followed. In this approach, $L^{(1)}$ is arbitrarily (without loss of generality) chosen as the reference shape and all the other training shapes $\{L^{(m)}\}_{m=2}^{M}$ are non-rigidly registered (after an initial affine alignment) to $L^{(1)}$ using the FEM-based deformable registration method (see section 7.3.1). The unbiased mean thoracic cavity shape $\overline{L}$ (see Figure 7.3d) is obtained by warping back the average of the registered training shapes using the inverse of the average deformation field.

2. **Building a SDM of thoracic cavity shape**: The possible variations of the thoracic cavity shape are represented by the set of nodal deformation field parameters $\{\mathbf{\Theta}^{(m)}\}_{m=1}^{M}$ that are estimated through the FEM-based deformable registration (after an initial affine alignment) of the training shapes $\{L^{(m)}\}_{m=1}^{M}$ with the mean shape $\overline{L}$. A Gaussian SDM is built to compactly encode these shape variations and the corresponding PCA-based regularizer E_S^{PCA} (see Eq. 7.5) is formulated for enforcing shape prior constraints in the next step.

3. **Segmentation via SDM constrained FEM-based registration**: The segmentation of the thoracic cavity in the input image I is performed on a binary thresholded version of the input image $BI : \Omega \rightarrow \{0,1\}$, which is obtained by setting the points in the input image that lie *outside* the HU ranges of muscle and fat tissues to 1. In order to initialize the segmentation, the mean shape

Tissue	Jaccard (%)	
	Thresholding	**Proposed framework**
Muscle	86.82 ± 5.31	$\mathbf{94.95 \pm 2.10}$
Fat	87.51 ± 8.74	$\mathbf{94.82 \pm 5.05}$

Table 7.1: Comparison of Jaccard scores obtained by thresholding-based segmentation and the proposed FEM-based segmentation framework with a SDM on 116 CT images. All values are reported as mean $\pm$ SD

Tissue	Area (cm^2)		Raw diff. (cm^2)	Diff. (%)	COV. (%)	**Jaccard** (%)
	Manual	**Automatic**				
Muscle	197.8 ± 44.7	$\mathbf{199 \pm 45.2}$	1.3 ± 6.0	0.6 ± 2.9	1.39 ± 1.58	$\mathbf{94.95 \pm 2.10}$
Fat	168.1 ± 84.4	$\mathbf{172.5 \pm 90}$	4.4 ± 8.4	0.7 ± 5.6	2.57 ± 3.03	$\mathbf{94.82 \pm 5.05}$

Table 7.2: Comparison of manual and automatic segmentation of thoracic CT images ($n = 116$). All values are reported as mean $\pm$ SD. Raw difference = (automated $-$ manual).

$\overline{L}$ is affinely-aligned with the thresholded image BI (see Figures 7.3b, 7.3e). The mean shape $\overline{L}$ is then deformed towards the thresholded image BI according to the minimization of the energy in Eq. 7.6 incorporating the shape-based regularizer E_S^{PCA}. This corresponds to the FEM-based deformable registration of BI to $\overline{L}$ where the deformations that deviate from the learned Gaussian SDM are penalized. The desired final thoracic cavity shape L^* (see Figure 7.3c, 7.3f) is determined by warping back the mean thoracic cavity shape $\overline{L}$ using the inverse of the optimal nodal deformation field parameters ${\boldsymbol{\Theta}^*}^{-1} = -\boldsymbol{\Theta}^*$, i.e., $L^*(\mathbf{x}) = \overline{L}(\mathbf{x} - \sum_{n=1}^{N} \mathbf{U}_n^* \phi_n)$, where $\boldsymbol{\Theta}^* = \{\mathbf{U}_n^*\}_{n=1}^N$.

4. **Muscle and fat region segmentation**: The muscle and fat region segmentation is simply performed by thresholding points in the input image that do not belong to the estimated thoracic cavity using the respective muscle and fat HU ranges (see Figure 7.4).

7.5 Experiments

Our experimental data set consisted of 146 axial 2D thoracic CT images of size 512×512 taken at the level of T4 from patients with head and neck cancers. Out of these 30 images were used for training the SDM and 116 images were used for testing.

7.5.1 Comparison with manual segmentation

The performance of the proposed automatic segmentation framework was evaluated by comparison with manual segmentations on all the 116 images in the test data set. The manual segmentations were performed by a single expert operator using Slice-O-Matic V4.3 software (Tomovision, Montreal, Canada), while the proposed automatic framework was implemented in MATLAB. The regularization parameters were chosen as $\gamma_R = 1.5$ and $\gamma_S = 1.0$ (see Equation 7.6). The non-uniform mesh on the mean shape of the thoracic cavity consisted of 503 nodes. It was generated by manually selecting a few seed points along the contour of the mean shape followed by Delaunay triangulation and refinement using the TRIANGLE [109] package. The experiments were run on a

Pct. of T4 SMI ($\mathrm{cm}^2/\mathrm{m}^2$)	Men	Women
95 th	92.7	68.4
75 th	77.0	59.0
Median 50 th	69.3	53.7
25 th	62.4	48.6
5 th	52.2	36.6

Sex specific distribution of SMI

Pct. of SMI ($\mathrm{cm}^2/\mathrm{m}^2$)	HR	Days of survival
$<$ 5 th	4.5^*	611^*
5th$-$25th	2.5^*	965^*
25th$-$50th	1.6	1382
$>$ 50 th	1	1540

Univariate relationship between SMI and survival. * denotes $p < 0.05$ Log rank test.

Table 7.3: Distribution of muscularity and relationship with survival. Here, the harzard ratio (HR) and the T4 skeletal muscle index (SMI) are reported. The sample size was $n = 116$ out of which 88 images were from males and 28 were from females.

3.2GHz Quadcore machine with 4GB of RAM. The automatic segmentation took about 1 min for each image. The Jaccard score was used to measure the overlap between the manual and automatic segmentations. In Table 7.1, it can be seen that a significant improvement in the Jaccard scores is achieved using the proposed framework compared to the simple thresholding-based segmentation. Further, the tissue cross-sectional areas (cm^2) were estimated from segmentations by summing up tissue pixels and multiplying by the pixel surface area. In Table 7.2, it can be seen that the coefficient of variation (COV) between the automatic and manual methods is within $(1-3)\%$ which is similar or less than inter- or intra- operator COVs reported for manual segmentation [35]. In Figure 7.4, visual segmentation results obtained using the proposed framework are also shown on 3 images.

7.5.2 Study of relationship between patient survival and muscularity

As previously mentioned, sarcopenia a muscle loss syndrome that commonly occurs in cancer patients is known to be associated with reduced patient survival. Conventional measures like body mass index (BMI) and body surface area (BSA) have been shown to be poor indicators of sarcopenia, because patients with similar BMI/BSA could still have widely different muscle masses [86]. A more direct estimate of the muscularity is the muscle tissue area (cm^2) which can be easily obtained from the segmentation of thoracic CT images using the proposed automatic segmentation method. Here, the use of the T4 skeletal muscle index (SMI) which is defined as the ratio of the height-adjusted cross-sectional muscle tissue area at the 4th thoracic vertebra and the square of the body height ($\mathrm{cm}^2/\mathrm{m}^2$) are investigated for detection of sarcopenia and thus as a predictor of patient survival. For this purpose, SMI was normalized over the male and female patient populations in our dataset using a percentile (pct.) distribution as shown in Table 7.3a. The result of a univariate log rank test performed between the pct. of SMI and the days of survival are shown in Table 7.3b. Here, for patients below the 25th SMI percentile (which indicates low muscularity hence sarcopenia), a statistically significant decrease in the survival times and a high harzard ratio (HR) is observed. This suggests that SMI is a good correlate of patient survival.

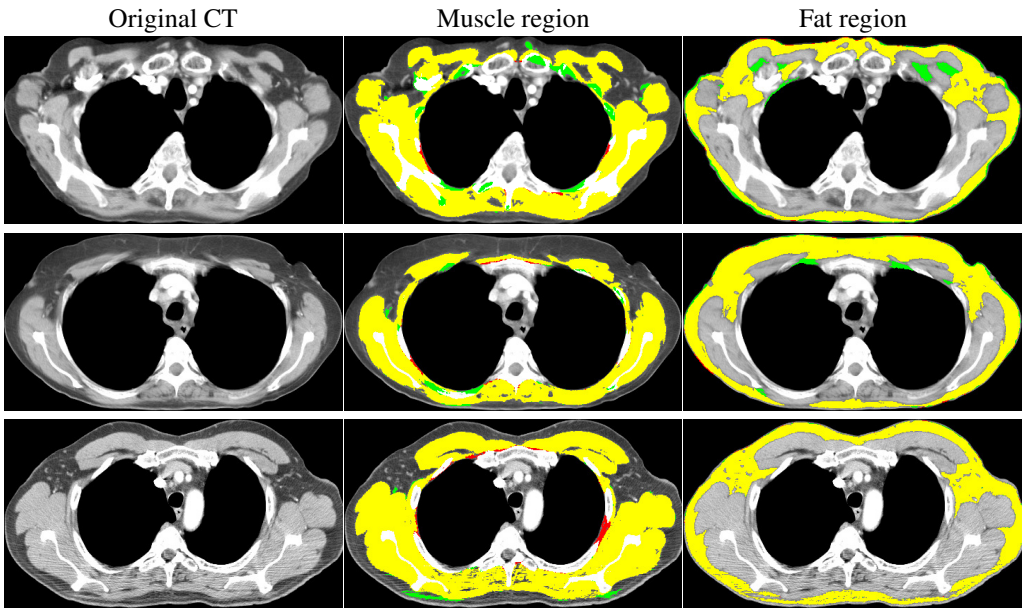

Figure 7.4: Muscle and fat region segmentation results. Manual label (red), automatic label (green) and overlap (yellow).

7.6 Discussion

The proposed automatic framework for thoracic CT images provides fast and accurate segmentations of both the muscle and fat tissues, which permits the undertaking of large scale cancer research studies involving measures based on muscle and fat proportions in the human body. The proposed thoracic CT segmentation approach can be directly extended to the segmentation of abdominal CT images. Therefore, in the future it is desirable to unify thoracic and abdominal CT segmentation using the FEM-based deformable registration with Gaussian SDM methodology. Further, currently the 2D CT slices are selected manually from the 3D volumetric CT scans of the patient body, corresponding to the 3rd lumbar vertebra (L3) and the 4th thoracic vertebra (T4) skeletal landmarks in the abdominal and thoracic cases respectively. Due to this manual selection, there is an element of human operator variability in the identification of these landmarks. To remedy this issue, a promising idea is to devise a method for the automatic localization of these vertebral landmarks by performing segmentation of the spinal cord in the 3D volumetric patient scans using the unified FEM-based registration and segmentation framework in Chapter 4 by taking advantage of the a priori known shape of the spinal cord through SDMs.

Chapter 8

Conclusion and future work

In this thesis, the powerful yet less explored finite element method (FEM) has been extensively employed for devising computationally efficient image registration and segmentation methods. In this chapter, the proposed FEM-based registration and segmentation methods are reviewed taking into account their experimental performance and areas for their future improvement are identified.

8.1 Conclusion

One of the main contributions in this thesis was to address both the registration and segmentation tasks using a unified FEM-based energy minimization framework. The applicability of the unified FEM-based minimization framework was not just limited to continuous registration and it was also extended for discrete deformable registration. This owed to the proposed novel variational minimization formulation of discrete registration. In the following, a brief review of the three main FEM-based registration and segmentation models proposed in this thesis is presented. A summary of the experimental results obtained by these FEM-based registration and segmentation methods is given in Table 8.1.

8.1.1 FEM-based continuous deformable registration

The traditional approach to deformable registration was to parametrize the unknown deformation field on a uniform mesh and solve the ensuing minimization problem corresponding to the deformable registration using the finite difference method (FDM). The main disadvantage of this approach was the computationally inefficiency that stemmed from the use of a high degrees of freedom (DOF) parametrization of the deformation field using a uniform discretization of the problem domain. The proposed FEM-based registration approach addressed this issue through the use of an image-adaptive non-uniform mesh which allows for a low DOF parametrization of the deformation field using Lagrange basis functions. The unified FEM-based energy minimization framework was then used to obtain a highly computationally efficient solution to the deformable registration problem. Another important aspect of the FEM-based deformable registration model was the use

Method	Task	Computational efficiency	Accuracy		
				Benchmark data	
			Test data	CUMC12	POPI-model
FEM-based continuous registration	registration	30x faster 30x lower DOF	2D synthetic 5 images AAE $\sim 1.4^{\circ}$	rank 4/16	rank 3/8
FEM-based continuous registration with a statistical deformation model	segmentation	-	116 images Muscle J. $\sim 95\%$ Fat J. $\sim 95\%$	-	-
FEM-based template-based multi-region segmentation	segmentation	$>$ 100x faster 10x-100x lower DOF	3 2D 1 3D images Binary J. $\sim 89\%$ 2 2D images Mlt.-rgn. J. $\sim 78\%$	-	-
FEM-based variational discrete deformable registration	registration	30x faster 30x lower DOF than RW [28]	2D synthetic 5 images AAE $\sim 8^{\circ}$	rank 6/16	rank 7/8

Table 8.1: Summary of the experimental results obtained using the various proposed FEM-based registration and segmentation methods. Here, the computational efficiency refers to the relative computational efficiency achieved by using the Lagrange basis parametrization compared to the B-spline and multi-linear parametrizations unless specified otherwise. On the test data, accuracy for the segmentation task corresponds to the mean Jaccard scores ($\%$) and for the registration task it corresponds to the mean average angular error (AAE) in degrees.

of a general diffusion-based regularization term as opposed to the task specific bio-mechanical regularizers that were generally used in previous works on deformable registration using the FEM method. Further, the FEM-based registration model was generalized to include the deformation models defined on uniform meshes using the B-spline and multi-linear basis functions. The experimental results on synthetic and real medical images unambiguously established the superior performance of the Lagrange basis parametrization over the conventional B-spline and multi-linear basis parametrizations in terms of computational efficiency that was achieved without compromising registration accuracy. Additional validation on benchmark datasets demonstrated that the proposed FEM-based registration method was very suitable for practical medical image registration tasks as it achieved registration accuracies similar to the current best available deformable registration methods.

Extension for shape prior constrained segmentation

The FEM-based continuous deformable registration model was extended to perform a shape prior constrained segmentation of binary images. The main idea here was to perform segmentation by deforming a binary template image towards the desired region of interest (ROI) in the input binary image through the minimization of the same energy functional that was used in FEM-based continuous deformable registration. However, to obtain a more accurate and robust segmentation, a priori shape information was introduced into the segmentation process using a Gaussian statistical deformation model (SDM) learned from a training set of deformations defined on a non-uniform mesh. The SDM was incorporated into the FEM-based continuous registration model as an additional reg-

ularization term apart from the diffusion-based regularizer. The motivation behind developing the SDM constrained FEM-based continuous registration method was the particular medical imaging application of muscle and fat tissue segmentation from 2D thoracic computed tomography (CT) images. The proposed method yielded excellent results for the muscle and fat tissue segmentation task when evaluated on a large database of CT images.

8.1.2 FEM-based template-based multi-region segmentation

In contrast to the popular level set optimization framework, a template-based approach was adopted along with the unified FEM-based minimization framework to develop a region-based segmentation methodology. The proposed FEM-based template-based segmentation method was inherently free from the drawbacks of the standard level set approach such as undesirable topological changes and difficulty in deal with multi-region segmentation. Further, it exploits the computational advantage offered by unified FEM-based minimization framework through the use of a non-uniform mesh well adapted to the contours of the ROIs in the template for a low DOF parametrization of the deformation field using Lagrange basis functions. Two different formulations of the FEM-based template-based segmentation method were proposed, both of which avoid the "more" non-convex data terms containing the warped input image and formulate the data terms using the original input image. The testing of the proposed template-based segmentation method on a set of real medical images validated the computational gains in using a Lagrange basis parametrization instead of the B-spline and multi-linear basis parametrization even in the case of a region-based energy minimization. Further, the proposed method obtained encouraging segmentation accuracies on the set of real medical images.

8.1.3 FEM-based variational discrete deformable registration

As an alternative to the standard Markov random field (MRF) based discrete deformable registration approaches, a novel variational formulation for discrete registration was developed. Borrowing the idea of assigning prior probabilities to each of the quantized deformation field values from the random walker (RW) based discrete registration method [28], a convex variational energy functional that corresponds to the diffusion-based smoothing of prior probability maps was formulated for discrete deformable registration. Interestingly, the FDM method based solution to this variational problem was shown to be exactly equivalent to the RW-based discrete registration method. But, a more computationally efficient solution was obtained by solving the convex variational formulation as a special case of the unified FEM-based energy minimization framework. The greater computational efficiency again arose from the use of a image-adaptive non-uniform discretization and the use of a low DOF Lagrange basis parametrization of the probability maps. The evaluation on synthetic medical images showed an improvement of multiple orders of magnitude in terms computational efficiency compared to the RW-based discrete registration method. The good registration accuracies

obtained on the benchmark datasets made evident the practical usefulness of the proposed FEM-based variational discrete registration method.

8.2 Future work

The registration and segmentation methods presented in this thesis were primarily unsupervised, except for the FEM-based continuous registration method extended using the basic Gaussian statistical deformation model (SDM) discussed in Section 7.3.3. In the future, the plan is to investigate more elaborate approaches for the incorporation of statistical models learned from training data into the proposed unified FEM-based registration and segmentation framework. Specially, the future work would focus on two main areas, shape priors using the SDMs for registration and segmentation, and multi-modal region intensity priors for image segmentation.

8.2.1 SDM-based shape priors for FEM-based registration and segmentation

The statistical deformable models (SDMs) were previously discussed in Section 7.1 and Section 7.3.3. The main challenge in the construction of SDMs is to efficiently model the space of nodal deformation parameters $\{\boldsymbol{\Theta}^{(m)} = \{\mathbf{U}_n^{(m)}\}_{n=1}^{N}\}_{m=1}^{M}$ given in the training data using a statistical model that not only accurately captures the shape variations in the training data but also allows for the SDM to be easily incorporated into the FEM-based deformable registration or template-based segmentation method. Below, few ideas related to the statistical modeling of the space of training nodal deformation field parameters are explored.

Multivariate probability models

As an alternative to the standard multivariate probability models like the Gaussian and Parzen density, a promising idea is to extend the graph-based SDM [44] which was originally proposed using uniform meshes and a B-spline parametrization to the FEM parametrization on non-uniform meshes. In the graph-based SDM, the high dimensional multivariate probability model is factored into a set of local low dimensional multivariate probability models by grouping the nodal points into a set of clusters. This clustering is usually performed based on the co-dependencies in the deformation field values between the nodes. The proposed approach would augment this clustering procedure with the adjacency information of the non-uniform mesh.

Manifold learning based models

A major difficulty encountered while estimating the above discussed multivariate probabilities is the very high dimensionality $N\nu$ of the data compared to the number of training data samples M, i.e., $N\nu >> M$. The manifold learning techniques such as ISOMAP, Diffusion-maps, LLE [3] overcome this issue by observing that even though the training data is represented as points in high dimensional space, i.e., $\boldsymbol{\Theta}^{(m)} \in \mathbb{R}^{N\nu}$, this data only occupies a small part of this high dimensional

space . In other words, the set of training nodal deformation field parameters $\{\boldsymbol{\Theta}^{(m)}\}_{m=1}^{M}$ are assumed to lie on a low dimensional manifold $\mathbb{R}^p$ embedded into the high dimensional space $\mathbb{R}^{N\nu}$ where $p << Nd$. Therefore, the goal in manifold learning is to estimate the low dimensional representation $\{\hat{\boldsymbol{\Theta}}^{(m)}\}_{m=1}^{M}$, with $\hat{\boldsymbol{\Theta}}^{(m)} \in \mathbb{R}^p$ of the original training data, which better captures the shapes variations than the multivariate probability models learned using the high dimensional representation. However, a key limitation in the use of manifold learning based SDMs, is the lack of explicit projection functions from the low dimensional space $\mathbb{R}^p$ back to original space $\mathbb{R}^{N\nu}$. Specifically, this causes difficulties in the formulation of shape based regularization terms that can be directly incorporated into the FEM-based deformable registration and template-based segmentation methods. There is a recent work [38] in the area of level set based segmentation using shape priors, that deals with this issue of unavailability of the projection functions, by endowing the level set based shape prior manifold with an approximate projection operator. The plan is to extend the ideas in this work to devise regularization terms using manifold learning based SDMs that can be integrated into the FEM-based deformable registration and template-based segmentation methods.

8.2.2 Multi-modal region intensity priors in FEM-based segmentation

This section advocates the incorporation of region intensity priors into the proposed FEM-based template-based multi-region segmentation method discussed in Section 4.3 for medical image segmentation tasks. Although, in general many anatomical structures of interest do not show sharp boundaries in single modality medical images, they might exhibit better contrast in the high-dimensional feature space of multi-modality medical images. In order to take advantage of multi-modality medical images, the region-based energy in Eq. 4.28 used for the FEM-based template-based multi-region segmentation method can be simply extended using multivariate densities to model the region statistics in the high-dimensional feature space. Further, the idea is to explore the learning of region intensity priors in this high-dimensional feature space. Another extension worth pursuing is the introduction of region-overlap priors [13] into the proposed FEM-based multi-region segmentation method.

Bibliography

[1] Columbia univ. medical centre mri dataset. www.mindboggle.info/papers/evaluation_NeuroImage2009/data/CUMC12.tar.gz. Accessed: 1/3/2013.

[2] T. Albrecht, M. Luthi, and T. Vetter. A statistical deformation prior for non-rigid image and shape registration. In Computer Vision and Pattern Recognition, 2008. CVPR 2008. IEEE Conference on, pages 1–8, 2008.

[3] P. Aljabar, R. Wolz, and D. Rueckert. Machine Learning in Computer-Aided Diagnosis: Medical Imaging Intelligence and Analysis, chapter Manifold Learning for Medical Image Registration, Segmentation, and Classification. 2012.

[4] Y. Amit. A nonlinear variational problem for image matching. SIAM Journal on Scientific Computing, 15(1):207–224, 1994.

[5] S. Andrews, G. Hamarneh, A. Yazdanpanah, B. HajGhanbari, and W. D. Reid. Probabilistic multi-shape segmentation of knee extensor and flexor muscles. In Medical Image Computing and Computer-Assisted Intervention–MICCAI 2011, pages 651–658. Springer, 2011.

[6] V. Arsigny, O. Commowick, N. Ayache, and X. Pennec. A fast and log-euclidean polyaffine framework for locally linear registration. Journal of Mathematical Imaging and Vision, 33(2):222–238, 2009.

[7] V. Arsigny, X. Pennec, and N. Ayache. Polyrigid and polyaffine transformations: A new class of diffeomorphisms for locally rigid or affine registration. Medical Image Computing and Computer-Assisted Intervention-MICCAI 2003, pages 829–837, 2003.

[8] J. Ashburner. A fast diffeomorphic image registration algorithm. Neuroimage, 38(1):95–113, 2007.

[9] J. Ashburner and K.J. Friston. Nonlinear spatial normalization using basis functions. Human brain mapping, 7(4):254–266, 1999.

[10] R.N. Baumgartner, K.M. Koehler, D. Gallagher, L. Romero, S.B. Heymsfield, R.R. Ross, P.J. Garry, and R.D. Lindeman. Epidemiology of sarcopenia among the elderly in new mexico. American journal of epidemiology, 147(8):755–763, 1998.

[11] M. Baust and N. Navab. A spherical harmonics shape model for level set segmentation. Computer Vision–ECCV 2010, pages 580–593, 2010.

[12] M.F. Beg, M.I. Miller, A. Trouvé, and L. Younes. Computing large deformation metric mappings via geodesic flows of diffeomorphisms. International Journal of Computer Vision, 61(2):139–157, 2005.

[13] I. Ben Ayed, S. Li, and I. Ross. A statistical overlap prior for variational image segmentation. International journal of computer vision, 85(1):115–132, 2009.

[14] L. Bertelli, M. Zuliani, and BS Manjunath. Pairwise similarities across images for multiple view rigid/non-rigid segmentation and registration. In Computer Vision, 2007. ICCV 2007. IEEE 11th International Conference on, pages 1–8. IEEE, 2007.

[15] C. Broit. Optimal registration of deformed images. PhD thesis, University of Pennsylvania, 1981.

[16] T. Brox. From pixels to regions: partial differential equations in image analysis. PhD thesis, Faculty of Mathematics and Computer Science, Saarland University, Germany, April 2005.

[17] T. Brox and J. Weickert. Level set segmentation with multiple regions. Image Processing, IEEE Transactions on, 15(10):3213–3218, 2006.

[18] P. Cachier, E. Bardinet, D. Dormont, X. Pennec, and N. Ayache. Iconic feature based nonrigid registration: the pasha algorithm. Computer Vision and Image Understanding, 89(2):272–298, 2003.

[19] N.D. Cahill, J.A. Noble, and D.J. Hawkes. Demons algorithms for fluid and curvature registration. In Biomedical Imaging: From Nano to Macro, 2009. ISBI'09. IEEE International Symposium on, pages 730–733, 2009.

[20] V. Caselles, F. Catté, T. Coll, and F. Dibos. A geometric model for active contours in image processing. Numerische Mathematik, 66(1):1–31, 1993.

[21] V. Caselles, R. Kimmel, and G. Sapiro. Geodesic active contours. International journal of computer vision, 22(1):61–79, 1997.

[22] R. Castillo, E. Castillo, R. Guerra, V.E. Johnson, T. McPhail, A.K. Garg, and T. Guerrero. A framework for evaluation of deformable image registration spatial accuracy using large landmark point sets. Physics in Medicine and Biology, 54(7):1849, 2009.

[23] T.F. Chan and L.A. Vese. Active contours without edges. Image Processing, IEEE Transactions on, 10(2):266–277, 2001.

[24] C. Chefd'hotel, G. Hermosillo, and O. Faugeras. Flows of diffeomorphisms for multimodal image registration. In Biomedical Imaging, 2002. Proceedings. 2002 IEEE International Symposium on, pages 753–756, 2002.

[25] G.E. Christensen. Deformable shape models for anatomy. PhD thesis, Washington University, St. Louis, Missouri, 1994.

[26] G.E. Christensen and H.J. Johnson. Consistent image registration. Medical Imaging, IEEE Transactions on, 20(7):568–582, 2001.

[27] H. Chung, D. Cobzas, J. Lieffers, L. Birdsell, and V. Baracos. Automated segmentation of muscle and adipose tissue on ct images for human body composition analysis. In SPIE Medical Imaging, 2009.

[28] D. Cobzas and A. Sen. Random walks for deformable image registration. Medical Image Computing and Computer-Assisted Intervention–MICCAI 2011, pages 557–565, 2011.

[29] L.D. Cohen. On active contour models and balloons. CVGIP: Image understanding, 53(2):211–218, 1991.

[30] L.D. Cohen and I. Cohen. Finite-element methods for active contour models and balloons for 2-d and 3-d images. Pattern Analysis and Machine Intelligence, IEEE Transactions on, 15(11):1131–1147, 1993.

[31] O. Commowick, R. Stefanescu, P. Fillard, V. Arsigny, N. Ayache, X. Pennec, and G. Malandain. Incorporating statistical measures of anatomical variability in atlas-to-subject registration for conformal brain radiotherapy. Medical Image Computing and Computer-Assisted Intervention–MICCAI 2005, pages 927–934, 2005.

[32] D. Cremers, S.J. Osher, and S. Soatto. Kernel density estimation and intrinsic alignment for knowledge-driven segmentation: Teaching level sets to walk. Pattern Recognition, pages 36–44, 2004.

[33] D. Cremers, M. Rousson, and R. Deriche. A review of statistical approaches to level set segmentation: integrating color, texture, motion and shape. International Journal of Computer Vision, 72(2):195–215, 2007.

[34] B. Delhay, P. Clarysse, C. Pera, and I.E. Magnin. A spatio-temporal deformation model for dense motion estimation in periodic cardiac image sequences. In Workshop from statistical atlases to personalized models: Understanding complex diseases in populations and individuals, MICCAI, 2006.

[35] E.W. Demerath, K.J. Ritter, W.A. Couch, N.L. Rogers, G.M. Moreno, et al. Validity of a new automated software program for visceral adipose tissue estimation. Int. jour. of obesity, 31(2):285–291, 2006.

[36] P. Dupuis, U. Grenander, and M.I. Miller. Variational problems on flows of diffeomorphisms for image matching. Quarterly of applied mathematics, 56(3):587, 1998.

[37] C.M. Engstrom, J. Fripp, V. Jurcak, D.G. Walker, O. Salvado, and S. Crozier. Segmentation of the quadratus lumborum muscle using statistical shape modeling. Journal of Magnetic Resonance Imaging, 33(6):1422–1429, 2011.

[38] P. Etyngier, F. Ségonne, and R. Keriven. Shape priors using manifold learning techniques. In Computer Vision, 2007. ICCV 2007. IEEE 11th International Conference on, pages 1–8. IEEE, 2007.

[39] M. Ferrant, O. Cuisenaire, and B. Macq. Multi-object segmentation of brain structures in 3d mri using a computerized atlas. SPIE Medical Imaging99, 3661:2, 1999.

[40] M. Ferrant, S. Warfield, C. Guttmann, R. Mulkern, F. Jolesz, and R. Kikinis. 3d image matching using a finite element based elastic deformation model. In Medical Image Computing and Computer-Assisted Intervention–MICCAI99, pages 202–209, 1999.

[41] B. Fischer and J. Modersitzki. Curvature based image registration. Journal of Mathematical Imaging and Vision, 18(1):81–85, 2003.

[42] M. Fornefett, K. Rohr, and H.S. Stiehl. Elastic registration of medical images using radial basis functions with compact support. In Computer Vision and Pattern Recognition, 1999. IEEE Computer Society Conference on., volume 1, 1999.

[43] M. Ghanbari. The cross-search algorithm for motion estimation. Communications, IEEE Transactions on, 38(7):950–953, 1990.

[44] B. Glocker, N. Komodakis, N. Navab, G. Tziritas, and N. Paragios. Dense registration with deformation priors. In Information Processing in Medical Imaging, pages 540–551, 2009.

[45] B. Glocker, N. Komodakis, G. Tziritas, N. Navab, and N. Paragios. Dense image registration through mrfs and efficient linear programming. Medical Image Analysis, 12(6):731–741, 2008.

[46] Günther Grabner, Andrew L Janke, Marc M Budge, David Smith, Jens Pruessner, and D Louis Collins. Symmetric atlasing and model based segmentation: an application to the hippocampus in older adults. In Medical Image Computing and Computer-Assisted Intervention–MICCAI 2006, pages 58–66. Springer, 2006.

[47] L. Grady. Multilabel random walker image segmentation using prior models. In Computer Vision and Pattern Recognition, 2005. CVPR 2005. IEEE Computer Society Conference on, volume 1, pages 763–770, 2005.

[48] S.A. Gronemeyer, R.G. Steen, W.M. Kauffman, W.E. Reddick, and J.O. Glass. Fast adipose tissue (fat) assessment by mri. Magnetic resonance imaging, 18(7):815–818, 2000.

[49] A. Guimond, J. Meunier, and J.P. Thirion. Average brain models: A convergence study. Computer vision and image understanding, 77(2):192–210, 2000.

[50] MS Hansen, R. Larsen, B. Glocker, and N. Navab. Adaptive parametrization of multivariate b-splines for image registration. In Computer Vision and Pattern Recognition, 2008. CVPR 2008. IEEE Conference on, pages 1–8, 2008.

[51] M. Hernandez, M.N. Bossa, and S. Olmos. Registration of anatomical images using geodesic paths of diffeomorphisms parameterized with stationary vector fields. 2007.

[52] K. Höllig. Finite element methods with B-splines, volume 26. Society for Industrial Mathematics, 1987.

[53] B.K.P. Horn and B.G. Schunck. Determining optical flow. Artificial intelligence, 17(1-3):185–203, 1981.

[54] X. Huang, Z. Li, and D. Metaxas. Learning coupled prior shape and appearance models for segmentation. MICCAI, pages 60–69, 2004.

[55] X. Huang, D. Metaxas, and T. Chen. Metamorphs: Deformable shape and texture models. In Computer Vision and Pattern Recognition, 2004., volume 1, pages I–496, 2004.

[56] P. Jordan, S. Socrate, TE Zickler, and RD Howe. Constitutive modeling of porcine liver in indentation using 3d ultrasound imaging. Journal of the mechanical behavior of biomedical materials, 2(2):192–201, 2009.

[57] S. Kabus, J. von Berg, T. Yamamoto, R. Opfer, and P.J. Keall. Lung ventilation estimation based on 4d-ct imaging. In MICCAI Workshop: Pulmonary Image Analysis, pages 73–81, 2008.

[58] N Kamiya, X Zhou, H Chen, T Hara, H Hoshi, R Yokoyama, M Kanematsu, and H Fujita. Automated recognition of the psoas major muscles on x-ray ct images. In Engineering in Medicine and Biology Society, 2009. EMBC 2009. Annual International Conference of the IEEE, pages 3557–3560. IEEE, 2009.

[59] N. Kamiya, X. Zhou, H. Chen, C. Muramatsu, T. Hara, R. Yokoyama, M. Kanematsu, H. Hoshi, and H. Fujita. Automated segmentation of recuts abdominis muscle using shape model in x-ray ct images. In Engineering in Medicine and Biology Society, EMBC, 2011 Annual International Conference of the IEEE, pages 7993–7996. IEEE, 2011.

[60] M. Kass, A. Witkin, and D. Terzopoulos. Snakes: Active contour models. International journal of computer vision, 1(4):321–331, 1988.

[61] A. Kelemen, G. Székely, and G. Gerig. Elastic model-based segmentation of 3-D neuroradiological data sets. Medical Imaging, IEEE Transactions on, 18(10):828–839, 1999.

[62] A. Klein, J. Andersson, B.A. Ardekani, J. Ashburner, B. Avants, M.C. Chiang, G.E. Christensen, D.L. Collins, J. Gee, P. Hellier, et al. Evaluation of 14 nonlinear deformation algorithms applied to human brain mri registration. Neuroimage, 46(3):786–802, 2009.

[63] S. Klein, M. Staring, and J.P.W. Pluim. Evaluation of optimization methods for nonrigid medical image registration using mutual information and b-splines. Image Processing, IEEE Transactions on, 16(12):2879–2890, 2007.

[64] J. Kullberg, H. Ahlström, L. Johansson, and H. Frimmel. Automated and reproducible segmentation of visceral and subcutaneous adipose tissue from abdominal mri. International Journal of Obesity, 31(12):1806–1817, 2007.

[65] C. Le Guyader and L.A. Vese. A combined segmentation and registration framework with a nonlinear elasticity smoother. Computer Vision and Image Understanding, 115(12):1689–1709, 2011.

[66] M.E. Leventon, W.E.L. Grimson, and O. Faugeras. Statistical shape influence in geodesic active contours. In CVPR, volume 1, pages 316–323, 2000.

[67] C. Li and Y. Sun. Active image: A shape and topology preserving segmentation method using b-spline free form deformations. In Image Processing (ICIP), 2010 17th IEEE International Conference on, pages 2221–2224. IEEE, 2010.

[68] J. Liang, T. McInerne, and D. Terzopoulos. United snakes. In ICCV, page 933, 1999.

[69] NA Lord, J. Ho, and BC Vemuri. USSR: A Unified Framework for Simultaneous Smoothing, Segmentation, and Registration of Multiple Images. In Computer Vision, 2007. ICCV 2007. IEEE 11th International Conference on, pages 1–6, 2007.

[70] P.V. Negrón. Marrero. A numerical method for detecting singular minimizers of multidimensional problems in nonlinear elasticity. Numerische Mathematik, 58(1):135–144, 1990.

[71] J.P. Mattei, Y.L. Fur, N. Cuge, S. Guis, P.J. Cozzone, and D. Bendahan. Segmentation of fascias, fat and muscle from magnetic resonance images in humans: the dispimag software. Magnetic Resonance Materials in Physics, Biology and Medicine, 19(5):275–279, 2006.

[72] J. Modersitzki. Numerical methods for image registration. Oxford University Press, USA, 2004.

[73] M. Mourtzakis, C.M.M. Prado, J.R. Lieffers, T. Reiman, L.J. McCargar, and V.E. Baracos. A practical and precise approach to quantification of body composition in cancer patients using computed tomography images acquired during routine care. Applied Physiology, Nutrition, and Metabolism, 33(5):997–1006, 2008.

[74] H-P Müller, F. Raudies, A. Unrath, H. Neumann, A.C. Ludolph, and J. Kassubek. Quantification of human body fat tissue percentage by mri. NMR in Biomedicine, 24(1):17–24, 2011.

[75] D. Mumford and J. Shah. Optimal approximations by piecewise smooth functions and associated variational problems. Comm. Pure Appl. Math, 42(5):577–685, 1989.

[76] H-H. Nagel. On the estimation of optical flow: Relations between different approaches and some new results. Artificial intelligence, 33(3):299–324, 1987.

[77] D. Nain, S. Haker, A. Bobick, and A. Tannenbaum. Multiscale 3-d shape representation and segmentation using spherical wavelets. Medical Imaging, IEEE Transactions on, 26(4):598–618, 2007.

[78] S. Osher and J.A. Sethian. Fronts propagating with curvature-dependent speed: algorithms based on hamilton-jacobi formulations. Journal of computational physics, 79(1):12–49, 1988.

[79] N. Paragios and R. Deriche. Unifying boundary and region-based information for geodesic active tracking. In Computer Vision and Pattern Recognition, 1999. IEEE Computer Society Conference on., 1999.

[80] N. Paragios and R. Deriche. Geodesic active regions: A new framework to deal with frame partition problems in computer vision. Journal of Visual Communication and Image Representation, 13(1-2):249–268, 2002.

[81] X. Pennec, P. Cachier, and N. Ayache. Understanding the demons algorithm: 3d non-rigid registration by gradient descent. In Medical Image Computing and Computer-Assisted Intervention–MICCAI99, pages 597–605, 1999.

[82] P. Perona and J. Malik. Scale-space and edge detection using anisotropic diffusion. Pattern Analysis and Machine Intelligence, IEEE Transactions on, 12(7):629–639, 1990.

[83] K.M. Pohl, J. Fisher, W.E.L. Grimson, R. Kikinis, and W.M. Wells. A bayesian model for joint segmentation and registration. NeuroImage, 31(1):228–239, 2006.

[84] K. Popuri, D. Cobzas, and M. Jagersand. Fast fem-based non-rigid registration. In Computer and Robot Vision (CRV), 2010 Canadian Conference on, pages 378–385, 2010.

[85] C.M.M. Prado, V.E. Baracos, L.J. McCargar, M. Mourtzakis, K.E. Mulder, T. Reiman, and et al. Body composition as an independent determinant of 5-fluorouracil–based chemotherapy toxicity. Clin. Canc. Res., 13(11):3264–3268, 2007.

[86] C.M.M. Prado, J.R. Lieffers, L.J. McCargar, T. Reiman, M.B. Sawyer, and et al. Prevalence and clinical implications of sarcopenic obesity in patients with solid tumours of the respiratory and gastrointestinal tracts: a population-based study. Lancet Oncol., 9(7):629–635, 2008.

[87] L. Ramus, O. Commowick, and G. Malandain. Construction of patient specific atlases from locally most similar anatomical pieces. In MICCAI, pages 155–162, 2010.

[88] J. N. Reddy. An introduction to the finite element method, volume 2. McGraw-Hill New York, 1993.

[89] P. Risholm, E. Samset, and W. Wells. Bayesian estimation of deformation and elastic parameters in non-rigid registration. Biomedical Image Registration, pages 104–115, 2010.

[90] G.K. Rohde, A. Aldroubi, and B.M. Dawant. The adaptive bases algorithm for intensity-based nonrigid image registration. Medical Imaging, IEEE Transactions on, 22(11):1470–1479, 2003.

[91] T. Rohlfing, C.R. Maurer Jr, D.A. Bluemke, and M.A. Jacobs. Volume-preserving nonrigid registration of mr breast images using free-form deformation with an incompressibility constraint. Medical Imaging, IEEE Transactions on, 22(6):730–741, 2003.

[92] K. Rohr, H. Stiehl, R. Sprengel, W. Beil, T. Buzug, J. Weese, and M. Kuhn. Point-based elastic registration of medical image data using approximating thin-plate splines. In Visualization in Biomedical Computing, pages 297–306. Springer, 1996.

[93] K. Rohr, H.S. Stiehl, R. Sprengel, T.M. Buzug, J. Weese, and MH Kuhn. Landmark-based elastic registration using approximating thin-plate splines. Medical Imaging, IEEE Transactions on, 20(6):526–534, 2001.

[94] K. Rohr and S. Worz. An extension of thin-plate splines for image registration with radial basis functions. In Biomedical Imaging (ISBI), 2012 9th IEEE International Symposium on, pages 442–445. IEEE, 2012.

[95] R. Ross, D. Dagnone, P.J.H. Jones, H. Smith, A. Paddags, R. Hudson, and I. Janssen. Reduction in obesity and related comorbid conditions after diet-induced weight loss or exercise-induced weight loss in mena randomized, controlled trial. Annals of Internal Medicine, 133(2):92–103, 2000.

[96] M. Rousson and N. Paragios. Shape priors for level set representations. ECCV 2002, pages 416–418, 2002.

[97] M. Rousson, N. Paragios, and R. Deriche. Implicit active shape models for 3D segmentation in MR imaging. Medical Image Computing and Computer-Assisted Intervention–MICCAI 2004, pages 209–216, 2004.

[98] M. Rousson and C. Xu. A general framework for image segmentation using ordered spatial dependency. Medical Image Computing and Computer-Assisted Intervention–MICCAI 2006, pages 848–855, 2006.

[99] D. Rueckert, P. Aljabar, R. Heckemann, J. Hajnal, and A. Hammers. Diffeomorphic registration using b-splines. Medical Image Computing and Computer-Assisted Intervention–MICCAI 2006, pages 702–709, 2006.

[100] D. Rueckert, A.F. Frangi, and J.A. Schnabel. Automatic construction of 3D statistical deformation models using non-rigid registration. In Proceedings of the 4th International Conference on Medical Image Computing and Computer-Assisted Intervention, pages 77–84, 2001.

[101] D. Rueckert, L.I. Sonoda, C. Hayes, D.L.G. Hill, M.O. Leach, and D.J. Hawkes. Nonrigid registration using free-form deformations: application to breast mr images. Medical Imaging, IEEE Transactions on, 18(8):712–721, 1999.

[102] KA Saddi, C. Chefd'hotel, M. Rousson, and F. Cheriet. Region-based segmentation via non-rigid template matching. In Computer Vision, 2007. ICCV 2007. IEEE 11th International Conference on, pages 1–7, 2007.

[103] D. Sarrut, V. Boldea, S. Miguet, and C. Ginestet. Simulation of four-dimensional ct images from deformable registration between inhale and exhale breath-hold ct scans. Medical physics, 33:605, 2006.

[104] L. A. Schwarz. Non-rigid registration using free-form deformations. PhD thesis, Ph. D. dissertation, Dept. CS, Technische Univ., Munchen, German, 2007.

[105] D.W. Shattuck, M. Mirza, V. Adisetiyo, C. Hojatkashani, G. Salamon, K.L. Narr, R.A. Poldrack, R. M. Bilder, and A.W. Toga. Construction of a 3d probabilistic atlas of human cortical structures. Neuroimage, 39(3):1064–1080, 2008.

[106] T. Shen, H. Li, Z. Qian, and X. Huang. Active volume models for 3d medical image segmentation. In Computer Vision and Pattern Recognition, 2009. CVPR 2009. IEEE Conference on, pages 707–714, 2009.

[107] T. Shen, Y. Zhu, X. Huang, J. Huang, D. Metaxas, and L. Axel. Active volume models with probabilistic object boundary prediction module. Medical Image Computing and Computer-Assisted Intervention–MICCAI 2008, pages 331–341, 2008.

[108] W. Shen, M. Punyanitya, Z. Wang, D. Gallagher, J. Onge, M-P. St.and Albu, S.B. Heymsfield, and S. Heshka. Total body skeletal muscle and adipose tissue volumes: estimation from a single abdominal cross-sectional image. Journal of Applied Physiology, 97(6):2333–2338, 2004.

[109] J.R. Shewchuk. Triangle: Engineering a 2D quality mesh generator and Delaunay triangulator. Lecture Notes in Computer Science, 1148:203–222, 1996.

[110] W. Shi, X. Zhuang, L. Pizarro, W. Bai, H. Wang, K-P. Tung, P. Edwards, and D. Rueckert. Registration using sparse free-form deformations. In MICCAI, pages 659–666. Springer, 2012.

[111] Hang Si and A TetGen. A quality tetrahedral mesh generator and three-dimensional delaunay triangulator. Weierstrass Institute for Applied Analysis and Stochastic, Berlin, Germany, 2006.

[112] R. Stefanescu, X. Pennec, and N. Ayache. Grid powered nonlinear image registration with locally adaptive regularization. Medical Image Analysis, 8(3):325–342, 2004.

[113] R.C. Stefanescu. Parallel nonlinear registration of medical images with a priori information on anatomy and pathology. PhD thesis, University of Nice Sophia Antipolis, 2005.

[114] G. Székely, A. Kelemen, C. Brechbühler, and G. Gerig. Segmentation of 2-d and 3-d objects from mri volume data using constrained elastic deformations of flexible fourier contour and surface models. Medical Image Analysis, 1(1):19–34, 1996.

[115] T.W.H. Tang and A. Chung. Non-rigid image registration using graph-cuts. In MICCAI, pages 916–924, 2007.

[116] M. Taron, N. Paragios, and M.P. Jolly. Registration with uncertainties and statistical modeling of shapes with variable metric kernels. TPAMI, 31(1):99–113, 2009.

[117] J.P. Thirion. Image matching as a diffusion process: an analogy with maxwell's demons. Medical image analysis, 2(3):243–260, 1998.

[118] A. Tsai, A. Yezzi Jr, W. Wells, C. Tempany, D. Tucker, A. Fan, W.E. Grimson, and A. Willsky. A shape-based approach to the segmentation of medical imagery using level sets. Medical Imaging, IEEE Transactions on, 22(2):137–154, 2003.

[119] G. Unal and G. Slabaugh. Coupled pdes for non-rigid registration and segmentation. In Computer Vision and Pattern Recognition, 2005. CVPR 2005. IEEE Computer Society Conference on, volume 1, pages 168–175, 2005.

[120] J. Vandemeulebroucke, D. Sarrut, P. Clarysse, et al. The popi-model, a point-validated pixel-based breathing thorax model. In Conference on the Use of Computers in Radiation Therapy, 2007.

[121] T. Vercauteren, X. Pennec, A. Perchant, and N. Ayache. Non-parametric diffeomorphic image registration with the demons algorithm. In Proceedings of the 10th international conference on Medical image computing and computer-assisted intervention, pages 319–326, 2007.

[122] T. Vercauteren, X. Pennec, A. Perchant, and N. Ayache. Symmetric log-domain diffeomorphic registration: A demons-based approach. Medical Image Computing and Computer-Assisted Intervention–MICCAI 2008, pages 754–761, 2008.

[123] L.A. Vese and T.F. Chan. A multiphase level set framework for image segmentation using the mumford and shah model. International Journal of Computer Vision, 50(3):271–293, 2002.

[124] J. von Berg, H. Barschdorf, T. Blaffert, S. Kabus, and C. Lorenz. Surface based cardiac and respiratory motion extraction for pulmonary structures from multi-phase ct. In Medical Imaging, pages 65110Y–65110Y. International Society for Optics and Photonics, 2007.

[125] Chaohui Wang, Olivier Teboul, Fabrice Michel, Salma Essafi, and Nikos Paragios. 3d knowledge-based segmentation using pose-invariant higher-order graphs. In Medical Image Computing and Computer-Assisted Intervention–MICCAI 2010, pages 189–196. Springer, 2010.

[126] F. Wang and B.C. Vemuri. Simultaneous registration and segmentation of anatomical structures from brain MRI. MICCAI 2005, pages 17–25, 2005.

[127] H. Wang, J.W. Suh, R. Das, Sandhitsu, et al. Multi-atlas segmentation with joint label fusion. TPAMI, 2012.

[128] Y. Wang and L. H. Staib. Integrated approaches to non-rigid registration in medical images. In Applications of Computer Vision, 1998. WACV'98. Proceedings., Fourth IEEE Workshop on, pages 102–108. IEEE, 1998.

[129] J. Weickert. Anisotropic diffusion in image processing. Teubner Stuttgart, 1998.

[130] H. Wendland. Piecewise polynomial, positive definite and compactly supported radial functions of minimal degree. Advances in computational Mathematics, 4(1):389–396, 1995.

[131] Z. Wu. Compactly supported positive definite radial functions. Advances in Computational Mathematics, 4(1):283–292, 1995.

[132] F. Xian, B. Pierre-Louis, B. John, et al. A multiple geometric deformable model framework for homeomorphic 3d medical image segmentation. In MMBIA, 2008.

[133] C. Xu and J.L. Prince. Snakes, shapes, and gradient vector flow. Image Processing, IEEE Transactions on, 7(3):359–369, 1998.

[134] Y. Yang, N.M. Wernick, and G. Brankov. A fast approach for accurate context-adaptive mesh generation. IEEE transactions on image processing, 12(8):866–881, 2003.

[135] I. Yanovsky, C. Le Guyader, A. Leow, A. W. Toga, P.M. Thompson, L. Vese, et al. Unbiased volumetric registration via nonlinear elastic regularization. In 2nd MICCAI Workshop on Mathematical Foundations of Computational Anatomy, 2008.

[136] A. Yezzi, L. Zollei, and T. Kapur. A variational framework for joint segmentation and registration. In Mathematical Methods in Biomedical Image Analysis, 2001. MMBIA 2001. IEEE Workshop on, pages 44–51, 2001.

[137] T. Yoshizumi, T. Nakamura, M. Yamane, A.H.M.W. Islam, M. Menju, K. Yamasaki, T. Arai, K. Kotani, T. Funahashi, S. Yamashita, et al. Abdominal fat: standardized technique for measurement at ct1. Radiology, 211(1):283–286, 1999.

[138] B. Zhao, J. Colville, J. Kalaigian, et al. Automated quantification of body fat distribution on volumetric computed tomography. Jour. of comp. assis. tomography, 30(5):777, 2006.

[139] S. Zhu and K-K. Ma. A new diamond search algorithm for fast block-matching motion estimation. Image Processing, IEEE Transactions on, 9(2):287–290, 2000.

[140] D. Zikic, M. Baust, A. Kamen, and N. Navab. Generalization of deformable registration in riemannian sobolev spaces. Medical Image Computing and Computer-Assisted Intervention–MICCAI 2010, pages 586–593, 2010.

[141] D. Zikic, A. Kamen, and N. Navab. Unifying characterization of deformable registration methods based on the inherent parametrization. Biomedical Image Registration, pages 161–172, 2010.